Wide-Area Forecasting of Total Electron Content over Europe

Dear, Richard Mark

Award date:
2007

Awarding institution:
University of Bath

Wide-Area Forecasting of Total Electron Content over Europe

Submitted by Richard Mark Dear

for the degree of Doctor of Philosophy

of the University of Bath

2007

ProQuest LLC
789 East Eisenhower Parkway
P.O. Box 1346
Ann Arbor, MI 48106-1346

Abstract

The aim of this research is to develop algorithms that can be applied to ionospheric forecasting. The basis of the work is a tomographic imaging technique that uses Global Positioning System (GPS) data to produce 3D, time-dependent images of electron density over large, continental-scale regions. The focus of this thesis is the mid-latitude ionosphere of Europe.

In the first instance, the imaging technique is evaluated using both simulated and experimental results. The vertical total electron content (TEC) is found to be determined with high accuracy but the distribution of the electron density vertically results in an underestimate of the peak density. These simulation results were confirmed by experiment and an improvement to the imaging was developed and demonstrated using independent data from other instruments.

The GPS observables differential phase and differential delay are both important in ionospheric measurement. The differential delay suffers from errors known as interfrequency bias (IFB). These need to be estimated to determine the ionospheric component of the delay. This estimation of the IFB values is tested under both simulation and experiment. The experimental results indicate errors about double those found from simulation. This is mainly due to a limitation in the simulation, as it does not include a representation of multipath.

Several approaches to forecasting wide-area images of vertical TEC are examined. Methods that worked successfully on single-location TEC time-series values were not successful because they were found to introduce artefacts into the forecasted images. The most successful approach involved the combination of a climatological model with an algorithm to search for previous similar changes in TEC. Forecasting accuracies of 2.97 and 4.63 and 4.95 TEC units were achieved for day-time TEC maps of 1, 3 and 6 hours ahead.

The major feature of the mid-latitude ionosphere at night is the trough. Algorithms are developed for estimating the position and movement of this feature. While the trough TEC is low and therefore does not impact the overall TEC accuracy in absolute terms, its position is of great importance for HF propagation predictions. The trough position was estimated to within 1.6° and 2.1°, and overall accuracies of 2.3 and 2.8 TEC units for the night time TEC maps.

The algorithms developed and tested in this research will enable the application of a real-time nowcasting and short-term forecasting ionospheric mapping system for Europe.

Table of Contents

List of Abbreviations

AFRL	Air Force Research Laboratory
C/A code	GPS Civil Coarse/Acquisition code
CCIR	Consultative Committee on International Radiocommunications
CIC	Combined Ionospheric Campaign
CME	Coronal Mass Ejection
CODE	Center of Orbit Determination in Europe
COSPAR	Committee of Space Research
DGPS	Differential GPS
DoD	Department of Defence
DST	Disturbance Storm Time
EC	Electron Concentration
EGNOS	European Geostationary Navigation Overlay Service
EISCAT	European Incoherent Scatter radar
EOF	Empirical Ortho-normal Function
EPSRC	Engineering and Physical Sciences Research Council
EUV	Extreme Ultraviolet radiation
FOC	Full Operational Capacity
foF2	Reflection frequency of F2 layer
GAIM	Global Assimilative Ionospheric Model
GIM	Global Ionospheric Maps
GPS	Global Positioning System
HF	High Frequency
IGS	International GNSS Service
IMF	Interplanetary Magnetic Field
INV	Data Structure of MIDAS inversion using IRI-95 model as input
IRI	International Reference Ionosphere
LEO	Low Earth Orbit
LT	Local Time
MCS	Master Control Station
MIDAS	Multi-Instrument Data Analysis System
MLT	Magnetic Local Time
MOD	Data structure for IRI-95 model data
MUF	Maximum Usable Frequency of ionosphere
NmF2	Electron concentration at the F2 layer

NN	Neural Network
NNSS	Navy Navigational Satellite System
NOAA	National Oceanic and Atmospheric Administration
P-code	GPS Precision code
PGM	Percentage Gradient Matching
PIM	Parameterised Ionospheric Model
PRN	Pseudo Random Noise
RAL	Rutherford Appleton Laboratory
RBF	Radial Basis Function
REAL	Data structure of MIDAS inversion using GPS data as input
SCTIP	Sheffield Coupled Thermosphere-Ionosphere-Plasmasphere model
SH	Spherical Harmonic
SIRM	Simplified Ionospheric Regional Model
SIRMUP	SIRM UPdating model
SOPAC	Scripps Orbit and Permanent Array Centre
SPIDR	Space Physics Interactive Data Resource
STIF	Short-Term Ionospheric Forecasting
TEC	Total Electron Content
UCL	University College London
UHF	Ultra High Frequency
URSI	International Union of Radio Science (or Union Radio-Scientifique Internationale)
UT	Universal Time
UV	Ultraviolet
WAAS	Wide-Area Augmentation System
WDC	World Data Centre

List of Symbols

A	Matrix of ray path lengths across voxels
C_B	Receiver clock bias
E	Receiver elevation angle
I	Total Electron Content
IFB_R	Receiver Interfrequency Bias
IFB_S	Satellite Interfrequency Bias
K_p	Magnetic Activity
L_i	Carrier Phase measurement for GPS frequency i
N	Peak Electron Density
P_i	Pseudorange measurement for GPS frequency i
R_E	Radius of Earth
R_n	GPS signal path length
T	Voxel to ortho-normal conversion matrix
U	Receiver co-ordinates
X	Matrix of contributions for the basis functions
b	Matrix of observed line integrals
c	Speed of light
f	Frequency
h	Height of ionospheric shell
n	Integer number of wavelength (Carrier phase measurement)
t	Time
x	Electron densities matrix
x_j	Unknown pixel density
y_i	Receiver-satellite ray
Λ	Trough Latitude
Λ_0	Trough at midnight local time constant
α	Trough magnetic activity variability constant
β	Trough local time variability constant
ε	Phase carrier dispersive components of receiver and satellite
ϕ	Longitude (geographic or geomagnetic)

λ	Carrier wavelength
θ	Latitude (geographic or geomagnetic)
ρ	Electron Density of a pixel
σ	Non-dispersive delays of a GPS signal
τ	Pseudorange dispersive components of receiver and satellite
Δ_{ij}	Ray length through an unknown pixel

Acknowledgments

Firstly, I would like to thank BAE Systems and the UK Engineering and Physical Sciences Research Council (EPSRC) for their support throughout this work. This work would also not have been possible without access to large data sets, made available by several organisations. They are the International GPS Service for the use of the GPS data, Space Physics Interactive Data Resource (SPIDR) and World Data Centre (WDC) for access to ionosonde data, WDC and National Oceanic and Atmospheric Administration (NOAA) for geophysical parameters used throughout this thesis, and the Center of Orbit Determination in Europe (CODE) for the use of their IFBs. I also acknowledge the use of the International Reference Ionosphere (IRI) and the Multi-Instrument Data Analysis System (MIDAS), without which, this thesis would not be as colourful.

I would also like to thank the many people at Bath who I have known. Many have supported me, either in an academic or social environment, without them, I would not have reached this stage of my career. I would also like to give a special thank-you to my supervisor, Cathryn, for her time and experience over the past few years, passing on her knowledge and enthusiasm for the subject.

A big thank-you to my parents for their help and guidance, throughout the past twenty-six years. Finally all my love to Jenny, for always being there, when most would not have had the patience.

Chapter 1 Introduction

1.1 The Ionosphere

The ionosphere is an ionised region of the Earth's atmosphere, starting at around 50 km altitude. Radio signals are refracted and delayed by the ionosphere. This was first demonstrated in 1901 by Marconi who showed transatlantic radio transmission by using the ionosphere to bounce signals to areas not in direct line of sight. Marconi was not concerned with the physical theory, and it was left to Lodge, and Kennelly and Heaviside to suggest that an electrically conducting layer in the upper atmosphere reflected the radio waves over this distance. Details of the early history of theories of this layer are described in more detail in Rishbeth (2001).

In the following section, mechanisms that produce the ionosphere are described. Details about the main regions and the variations that occur over various timescales are also given. The final part of this chapter covers the two main techniques for imaging the ionosphere.

1.1.1 Formation

Over the hundred years since Marconi's demonstration, the theory of the ionosphere has been studied and developed extensively, and now the physical processes are largely well understood. The main source of energy is produced by the Sun in the form of extreme ultra-violet (EUV) radiation. This causes ionisation of the neutral atoms and molecules in the outermost regions of the Earth's atmosphere. Ionisation is the process where a neutral atom or molecule is converted into a free electron and a positively charged ion. The free electron produced is about 20,000 times lighter than the ion, and is able to be made to oscillate by radio waves travelling through the region.

There are two further mechanisms, called recombination and attachment, which remove the free electrons from the atmosphere. At high altitudes, the main process is recombination, where a positively charged ion, recombines with a free electron to produce a neutral atom. There are two types of recombination, with the most efficient being a two-stage process called dissociative recombination. The first stage involves attachment of a positive ion to O_2 or N_2, then the second stage is the combination with an electron, leaving the molecule and the ion. The other process is attachment, which occurs when free electrons attach themselves to neutral atoms, producing negatively charged ions.

In simple terms, the electron concentration in the atmosphere is the offset between these mechanisms. The rate of change of free electrons in the atmosphere varies throughout the day as all of the processes are more efficient dependant upon conditions. Recombination and attachment always take place but vary due to the population of the particular species in the neutral atmosphere. This effect is exaggerated at high altitudes, near, and above, the F2 peak, as concentrations of neutral species at these altitudes are much lower and electrons have a smaller probability of recombining by charge transfer. The photoionisation process does not always occur as it requires the Sun, and thus does not occur at night. A maximum in electron density is reached just after local midday where this process is greatest due to the intensity of the rays from the Sun. After sunset, recombination and attachment are the only processes and therefore electron density decreases. Recombination is not completely efficient, as all electrons are not removed by sunrise.

Apart from these chemical mechanisms, there are other systems that affect the atmosphere. The major effect is from the Earth's magnetic field. When a current passes through a magnetic field a force is produced. This mechanism can be seen most at night time, when free electrons rise in altitude in the absence of the effects from the Sun's radiation.

1.1.2 Structure

The ionosphere can be classified into various distinct regions. They all vary in their characteristics and properties due to the diverse chemical processes that produce them. Figure 1.1 (Hargreaves and Burns, 1996), shows the distribution of electron concentration with height in the daytime. At night the lower layers have negligible concentration as the source of the photoionisation, the Sun's energy, is not provided. Brief descriptions of the various regions of the ionosphere are given in the following subsections.

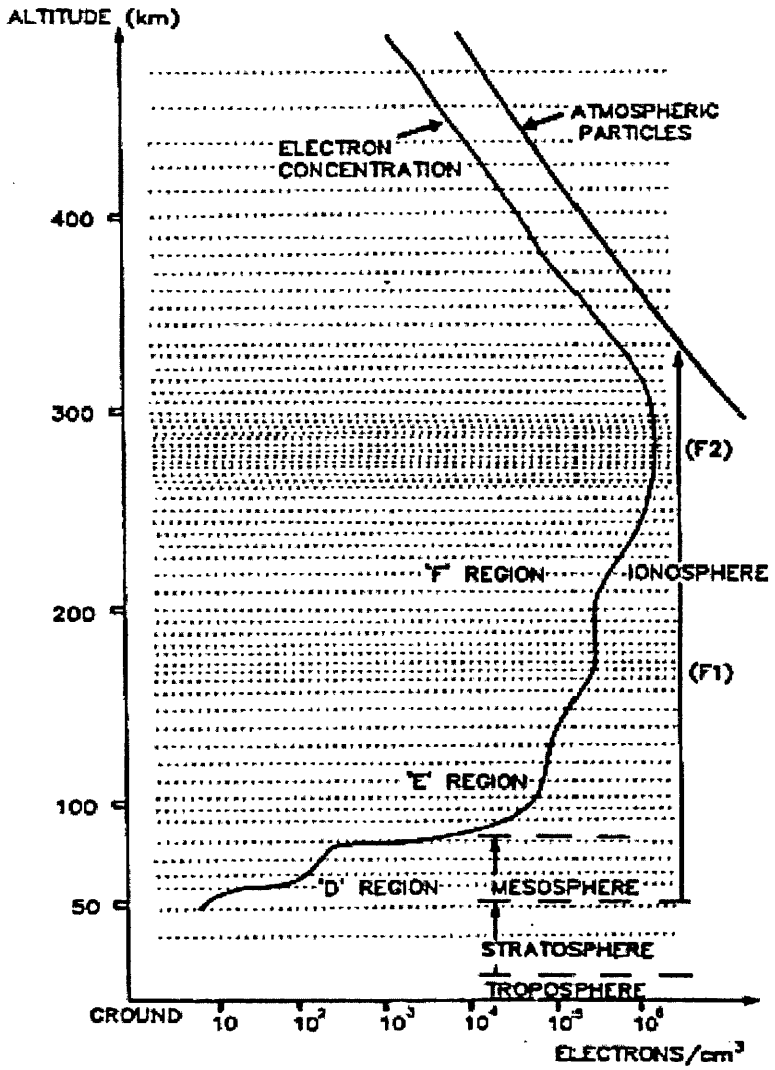

Figure 1.1. **Distribution of electron concentration with height (Hargreaves and Burns, 1996).**

D-region

The D-region is the lowest region with significant ionisation and has an upper altitude around 90 km. The D region ionisation is greatest during daylight hours due to its dependence on energy from the sun. The layer therefore has a daily maximum shortly after midday local time with the maximum being greatest in the summer months. The electron density is dependent on height with the largest electron concentrations occurring at the boundary to the E-region. Electron concentrations are lower than at higher altitudes in the F region because recombination and attachment are more efficient due to greater populations of the molecules required for these to take place. Free electrons also rise to higher altitudes due to diffusion, caused by the Earth's magnetic field.

E-region

The E-region is between altitudes 90 km and 140 km and is seen to have largest electron concentrations just after midday local time and, like the D-layer, reduces to low levels at night. The E-region is only dense enough to refract HF signals during the daytime hours and is used for HF propagation for hop distances up to 2000 km. Small areas of large densities, called sporadic E, can be observed that last for only a few hours at heights of approximately 105 km. Their appearance is hard to predict but seasonal trends have been found in the auroral zone, and daily trends have been identified in the equatorial zone. The result is to produce shorter HF propagation paths than usual as the signals will not travel to the heights expected without the sporadic E being present.

F-region

The F-region extends in altitude stretches from 140 km to about 400 km and can be split into two separate sections as two peaks can be produced, depending upon times of day and prevailing geophysical conditions. The F1-region is from 140 km to 200 km, and the F2-region from 200 km to 500 km. The F1 and F2 layers are defined as the height where there is a peak of the electron concentration in a particular altitude range. The F1 layer is found at altitudes from 130 km to 300 km during daylight hours. At night this layer combines with the F2-layer, which is normally about 300 km but can be as high as 500 km, as it is strongly influenced by short-term events such as geomagnetic storms. The most used parameter for HF users is foF2, which is the frequency that signals reflect off the peak electron concentration in the F2 layer.

Topside Ionosphere

The topside ionosphere is the region above the peak electron concentrations of the F-layer where the electron density decreases with altitude. Little change is seen between day and night concentrations as processes that produce and remove free electrons are rare due to the much reduced likelihood of the conditions required for them to occur.

1.1.3 Short and long-term variations

Diurnal

The diurnal variation is caused by the relationships between the chemical mechanisms that affect the concentration of free electrons. This produces a peak in the early afternoon, after maximum EUV radiation occurs, and a minimum just before sunrise, the greatest time since EUV radiation occurred. The daily variation of integrated electron density in the northern

hemisphere is shown in Figure 1.2, for a day in December 2002 from the International Reference Ionosphere (IRI), Bilitza 1990.

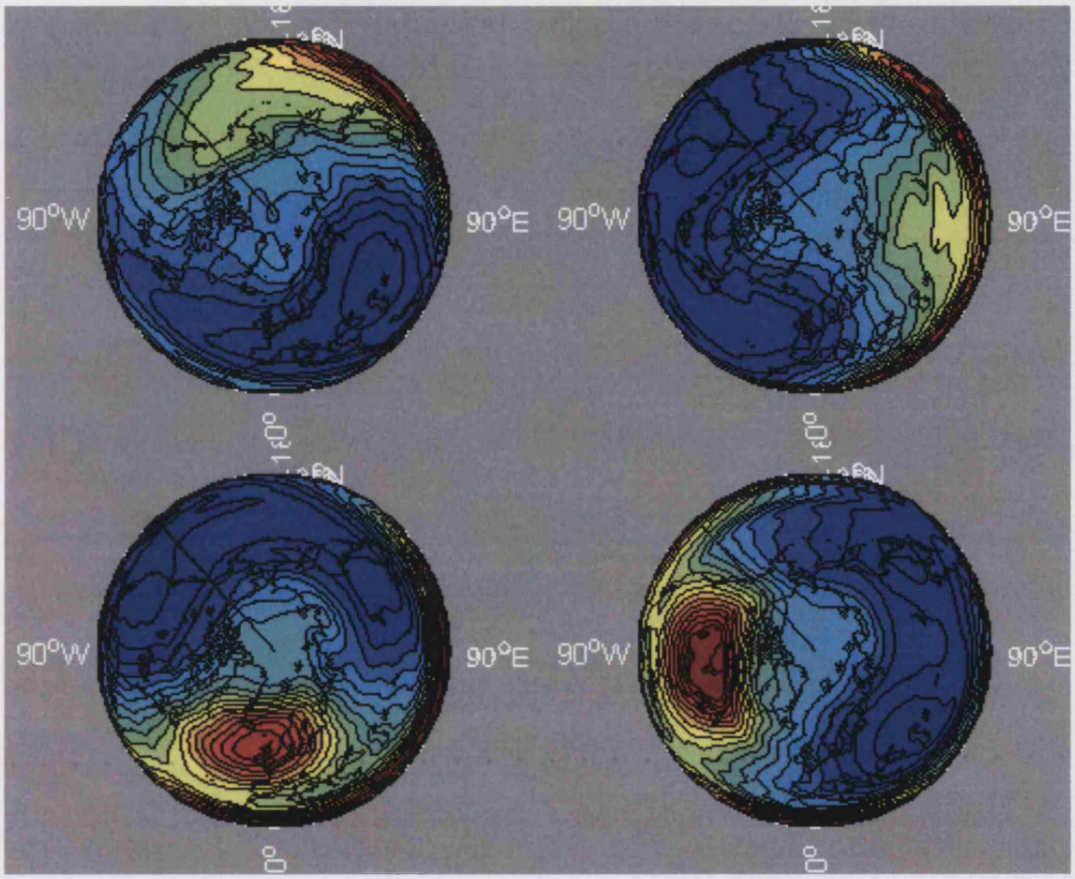

Figure 1.2. Daily ionospheric TEC variation on December 22, 2002 at 00 UT, 06 UT, 12 UT and 18 UT from IRI simulations (Peak mid-latitude TEC is 80 TEC units).

Seasonal

The tilt of the Earth with respect to the Sun's rays mean that the Sun is overhead at the Tropic of Cancer (23.5°N) at the summer solstice, June 21st, and overhead at the Tropic of Capricorn (23.5°S) at the winter solstice, December 21st. The solar zenith angle in the mid-latitudes of the northern hemisphere is therefore less at noon in the summer than the winter. If the diurnal variation was applied to this annual change in the mid-latitudes in the northern hemisphere, this would result in a larger peak in electron density in the summer. This is not the case as a minimum is seen instead. This is due to the complex effect the Sun has on the neutral atmosphere. In summer there is an increase in the production of free electrons, and also the rate of electron loss. The increase in the summertime loss overwhelms the increase in production and so produces the decrease of the peak concentrations. The effect is known as the winter

anomaly and can be seen in both hemispheres, although less common in the southern hemisphere.

Location

The ionosphere can be divided into three separate latitudinal areas depending upon the dominant processes in that region.

Firstly the equatorial region is described, which is controlled mainly by the fountain effect. The Earth's magnetic field produces a peak in concentration of electrons between 10° and 20° away from the magnetic equator. Electrons that are produced by photoionisation in the equatorial region rise, by the combination of electric and magnetic fields, then travel away from the equator along magnetic field lines to produce the peak of electron concentration.

Secondly, the auroral (and polar cap) region has more complex physical processes, as this area can either have prolonged periods of darkness or light, instead of the diurnal variation seen in mid-latitudes. Auroral blobs are structures produced by particle precipitation from the magnetosphere. The coupling effect with the magnetosphere, due to the open field lines in this area, mean that the solar wind and the Interplanetary Magnetic Field (IMF) are important factors in this region.

Finally, the mid-latitudes do not have the large movement of particles associated with the other regions. Instead, the solar effects are dominant during the day and the magnetic effects during the night. Some structures present in these latitudes produce unexpected variations from that expected by simple theory. Examples of such structures are the winter anomaly, the mid-latitude trough and travelling ionospheric disturbances.

Solar Activity

The amount of EUV radiation received at the Earth is related to the number and size of sunspots on the Sun's surface. The production of sunspots is affected by numerous mechanisms under the Sun's surface. Some of these are understood, but there are still many that are not, and this means that the amount of EUV radiation produced by the Sun is very hard to predict. There are trends in this production and these are used to produce an estimate of what the Sun will produce at a given time.

The shortest cycle is a 27-day cycle and is due to the rotation of the Sun. Sunspots are mainly found near its equator, but they are randomly distributed around this axis with large sunspots producing peaks of EUV radiation for three or four solar rotations. A longer trend is produced by the 11-year solar cycle and causes peaks in the 12-month average of sunspot number, called solar maxima, with the most recent peak occurring between the years 2000 and 2002. Figure 1.3 shows the variations of sunspot number since the peak of solar cycle 22, January 1980, using data from the National Oceanic and Atmospheric Administration (NOAA) website, http://www.sec.noaa.gov, and showing the monthly and 12-month mean of the sunspot number.

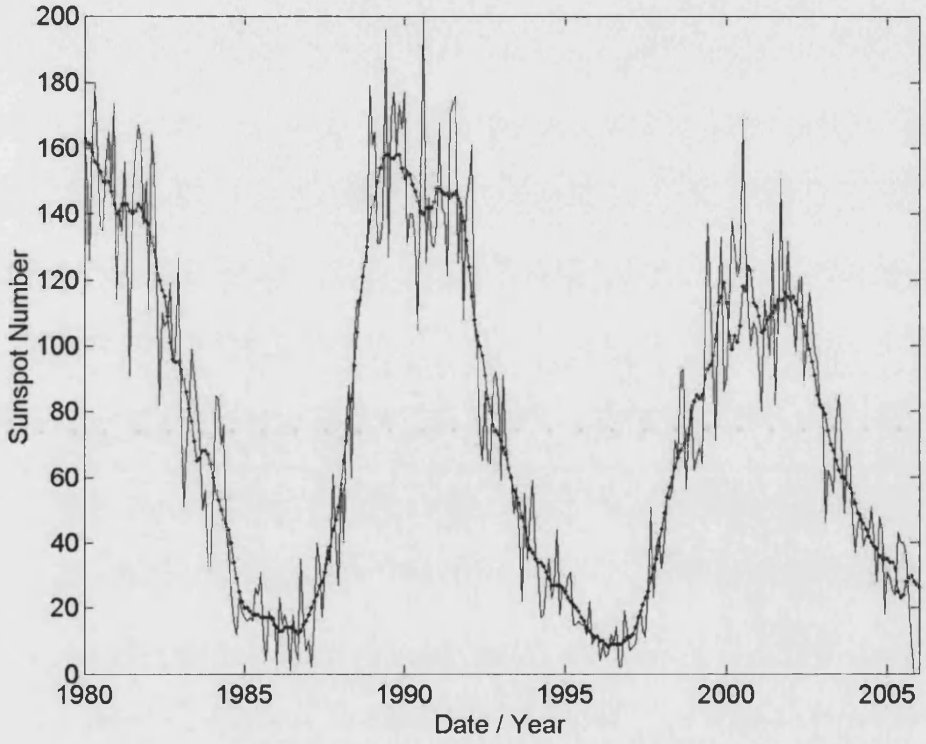

Figure 1.3. Variation of sunspot number, monthly and 12-month (Dots), from the peak of solar cycle 21.

Short term variations can be caused by large solar flares, or coronal mass ejections (CMEs), from the Sun (Rees, 1995). The solar wind carries with it the weak interplanetary magnetic field, IMF, and if this meets the Earth's path, intense electric fields can be produced along geomagnetic field lines to the high latitude ionosphere, which in turn affect the lower latitudes. (Buonsanto, 1999). Changes in the rates of production and loss of ionisation are produced, which produces an increase of electron concentration for the day of the storm commencement, but may also produce a large reduction of electron concentration for several days after the initial storm event. This is called the negative phase of the storm.

1.1.4 Main Ionospheric Trough

The main ionospheric trough is a longitudinally extended depletion in the electron density of the night time ionosphere. The northern wall is associated with the southern boundary of the auroral zone and is usually within 5° of the auroral oval. An example plot of the trough is shown in Figure 1.4, with units $1x10^{16}$ e m^{-2} (TECU). The trough shown is at latitudes between 50°N and 60°N at these European longitudes in this ionospheric image. The production of such images is discussed in Section 2.4.

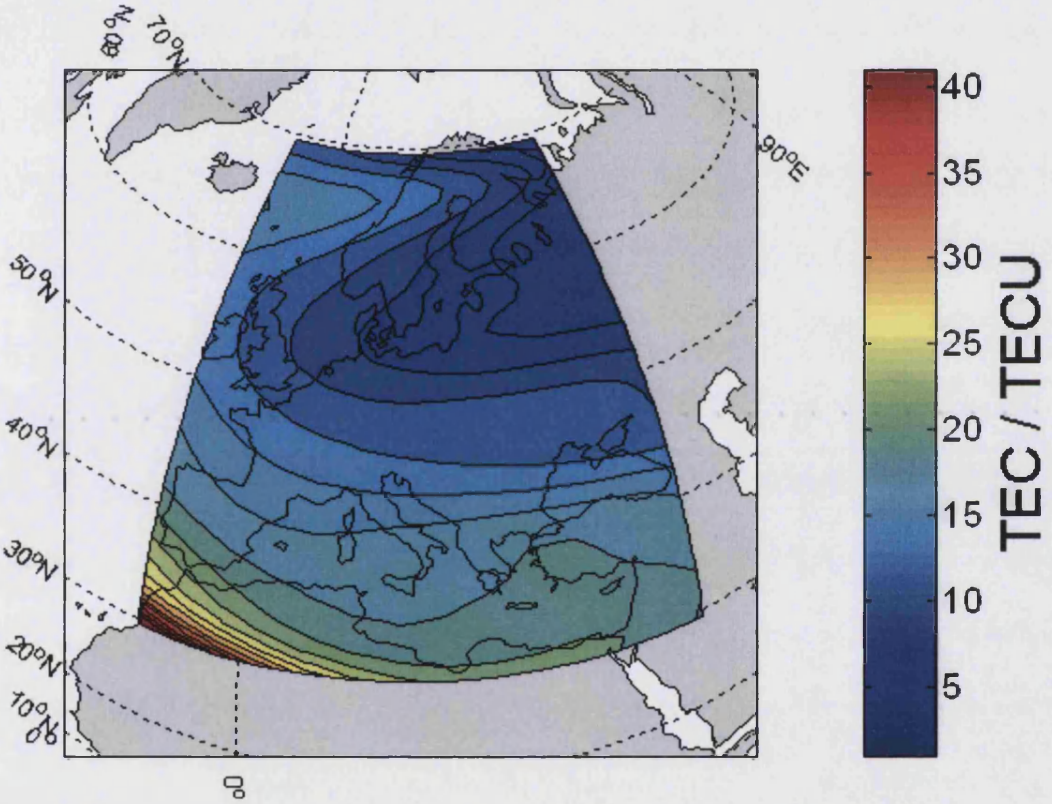

Figure 1.4. Example trough for February 15th 00:00 UT 2002.

Reviews of the modelling and observation of the main ionospheric trough are given by Moffett and Quegan (1983) and Rodger et al. (1992). Their findings can be summarised as follows. The mid-latitude trough is primarily a night-side phenomenon, although has been observed at all local times, and is most regularly seen in winter and during equinox. The pole ward edge of the trough is usually field aligned and lies close to the boundary of the diffuse aurora. The latitude of the trough decreases throughout the night and at quiet times may move back to higher latitudes in the early morning hours. Also during increased geomagnetic activity, the trough is

observed at lower latitudes for a given magnetic local time and the occurrence of the trough is largely independent upon the level of solar activity. The variations in the electron concentration of the ionosphere produced by the trough can have significant implications for radio systems. The propagation delay is affected due to the changes of electron concentration, and other small scale phenomena, such as scintillation, are more likely to occur.

The trough is much more common during the winter months as can be seen in Figure 1.5 which shows the probability of the trough forming near midnight, (Karpachev and Afonin, 1998). The trough, once formed, moves southward as the night continues. In addition, its position will be further south for greater magnetic activity, with the K_p index, the planetary magnetic index, being the most used parameter to describe the current magnetic conditions.

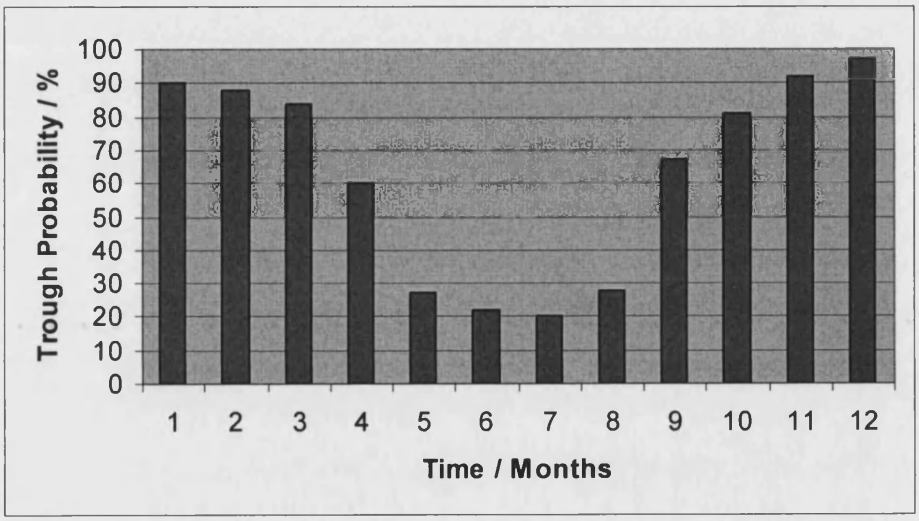

Figure 1.5. Probability of trough occurring near midnight (20-04 UT) from Karpachev and Afonin (1998).

The trough location was found to be mainly dependant upon local time and geomagnetic activity. Consequently, models of its position take the form:

$$\Lambda = \Lambda_0 - \alpha K_p - \beta t \qquad [1.1]$$

where Λ is the latitudinal position of the trough, α and β and χ are constants, K_p is the three-hour planetary magnetic index, t is the time difference in hours from midnight (negative before midnight, positive thereafter), and Λ_0 is an estimate of the position of the trough when K_p and t are equal to zero. The structure may be similar, but the equations suggested by each of the

groups have different coefficient. This is due to the different methods used to obtain the ionospheric measurements and the location at which the data was recorded.

The earliest studies of trough occurrence and empirical modelling of the trough position were by Rycroft and Burnell (1970) and Kohnlein and Raitt (1977). The formula produced by Rycroft and Burnell used measurements from a topside sounder on the Alouette I satellite is the first to show a magnetic and local time dependence.

$$\Lambda = 62.7 - 1.4K_p - 0.7t \qquad [1.2]$$

Kohnlein and Raitt (1977) used plasma density measurements from the ESRO4 satellite. Observations were carried out from November 1972 until April 1974, which was a period of low solar activity. Three hundred observations were used over this time period and it was found that in April and May; the trough was observed between 19 LT until 05 LT and the following relationship was found.

$$\Lambda = 65.2 - 2.1K_p - 0.5t \qquad [1.3]$$

The accuracy of this model is given as ±2° and the occurrence of the event is heavily biased to the post-midnight sector.

Collis and Haggstrom (1988) used incoherent scatter data from Northern Scandinavia. Trough measurements were taken on 28 days between April 1986 and April 1987, and found that the following relationship can be produced.

$$\Lambda = 62.2 - 1.6K_p - 1.35t \qquad [1.4]$$

These trough formulae have been used extensively to predict the position of the trough, but in recent years researchers have tried to use data covering a wider area and thus produce a prediction algorithm that will specify the trough position over a greater variety of locations. An objective of this project will be to determine which of these approaches produces the most accurate position for use in prediction algorithms. The magnetic co-ordinate system produces the most accurate results for all locations around the globe but this may not be necessary for the area that will be studied, as there is only a small difference between geographic and magnetic

co-ordinate systems over Europe. The formula of Karpachev et al. (1996) used a statistical model, not restricted to linear relationships.

The trough position was predicted between 18-06 UT is in the midnight segment of a circle (polar coordinate system) centred at 86.5° latitude and 3.5 MLT (magnetic local time) meridian with radius given by,

$$r = 24.0 + 2.3K_p \qquad [1.5]$$

or the linear approximation

$$\Lambda = 66.3 - 2.35K_p - 0.55t \qquad [1.6]$$

The standard deviation of this method is 1.9° for the full time period. This reduces to 1.7° when either the pre or post-midnight data is used.

The three-dimensional structure of the trough is now being investigated and results are being verified using these models to ensure that a trough can be expected at the latitudes seen in the images (Hedin et al., 2001). Also Meggs et al. (2005) has compared the output produced by MIDAS with an incoherent scatter radar, and found that both found depletions in the same region.

1.2 Developments in ionospheric forecasting in this thesis

In this thesis the specification and forecasting of ionospheric electron density over Europe is developed and the accuracy is established.

The research is based upon an algorithm to image the electron density from GPS (Global Positioning System) data. GPS is described in Section 2.5, the imaging approach is described in Section 2.4. GPS provides two different quantities that relate to the ionospheric total electron content (TEC) – the differential phase advance and the differential group delay. The phase of the signal is a highly-accurate measurement that gives a relative change in the TEC, whereas the group delay is subject to stable biases. These biases are a large component of the overall value and are specific to a given receiver or satellite (Chapter 5). This dual measurement system allows the assessment of imaging accuracy, by using only the phase data to make the images the code delay data can be reserved for image accuracy assessment. Through both simulation and experiment the accuracy of the imaging technique in terms of TEC mapping has been assessed.

The vertical profile of electron density obtained from ionospheric imaging using only ground-based data was also assessed (Chapter 4). It was found that a systematic underestimate of the peak density was encountered because of the inability to define the basis functions used in the imaging. A new approach was developed whereby the peak density and scale heights from ionosonde data were used to assist the reconstruction. This is particularly applicable to HF applications where the vertical profile is critical to the outcome.

Various methods for forecasting the daytime TEC over large-regions were explored (Chapter 6 and Chapter 7). It was found that methods that worked well for isolated locations did not translate to wide-area mapping and could produce spurious artefacts. The preferred approach shown to work here involved the use of a climatological model coupled to the imaging. This was shown to be applicable even during disturbed conditions. For the night-time, the main trough was the dominant feature and its movement and density changes necessitated the use of feature recognition coupled into the forecasting.

This work has demonstrated that mean absolute daytime TEC accuracies of 3.0, 4.6 and 5.0 TECU can be achieved for real-time, 1, 3 and 6 hour forecasts of the ionosphere over Europe. By using IRI along with a trough movement model the TEC can be forecast for periods of 1 and 3 hours to an accuracy of 2.3 and 2.8 TECU, and the trough position to 1.6° and 2.1°.

Chapter 2 Imaging Techniques

2.1 Introduction

In the Chapter, an introduction to the two main approaches that are used to determine vertical TEC will be given. The first is the thin-shell model, which approximates the ionosphere as a shell at constant altitude. The second, tomography, is a more recent technique, and uses a two or three-dimensional grid to represent the ionosphere. The inversion approach used to produce the ionospheric images in this thesis will then be introduced. The final part of the Chapter is how the data used for these approaches is produced. The main source is the Global Positioning System (GPS). An overview of GPS is given first, followed by how TEC measurements are derived from it. The final section of the Chapter gives an overview of another source of ionospheric data used in this thesis, the ionosonde.

2.2 Thin-shell model

The thin shell model produces a two-dimensional map in the latitudinal and longitudinal directions by mapping the slant TEC of satellite to receiver rays onto a shell at a height (normally 350-400 km) near the F2 peak. With knowledge of the receiver and satellite position, the intersection of the ray with the shell can be found using basic trigonometry. Slant TEC (sTEC) can be approximated to vertical TEC (vTEC) using mapping functions, before the shell surface is used to interpolate between intersecting points (Wilson and Mannucci, 1993). The geometry of the problem can be seen in Figure 2.1, which shows a satellite and a ground based receiver. The positions of the satellite and receiver are x_s and x_r, R_E is the radius of the Earth, h is the shell height, E is the elevation angle of the ray, and (θ, ϕ) is the latitude and longitude of the intersection point of the ray and shell.

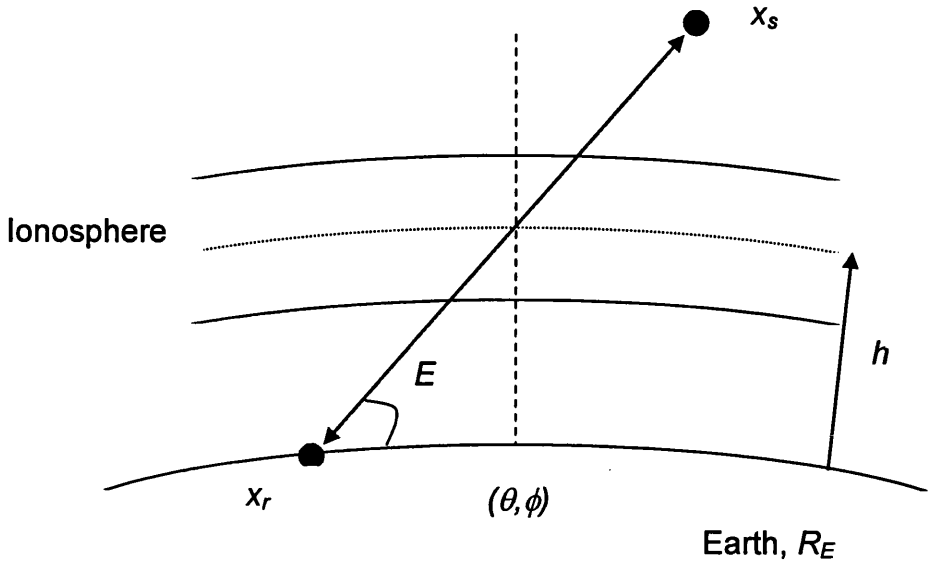

Figure 2.1. Diagram showing the geometry of thin-shell approach to TEC mapping.

Examples of the thin shell model in use include the original model developed by NASA Jet Propulsion Laboratory (JPL) and the WAAS (Wide-Area Augmentation System) network, (Mannucci et al., 1999).

Mathematically the problem can be described as follows (Mannucci et al., 1999). The integrated electron density, or total electron content (TEC), along a ray path between a satellite and a receiver is expressed as:

$$I = \int_{x_r}^{x_s} \rho(\theta,\phi,h)ds \qquad [2.1]$$

where I is the TEC, ρ is the electron concentration at a given latitude (θ), longitude (ϕ) and height (h). The shell model uses the approximation that there is negligible horizontal variation of electron density along the ray path. This therefore means that each ray can be approximated at a single latitude and longitude coordinate (θ_m, ϕ_m).

$$I \approx \int_{x_r}^{x_s} \rho(\theta_m,\phi_m,h)ds \qquad [2.2]$$

As the horizontal variation is considered insignificant, we can define that

$$\rho_m(h) = \rho(\theta_m, \phi_m, h) \qquad [2.3]$$

Transforming the variable of integration to height, and using the geometrical transformation that relates path to height changes,

$$ds = \frac{\rho_m(h)dh}{\sqrt{1 - \frac{\cos^2 E}{(1 + h/R_E)^2}}} \qquad [2.4]$$

and therefore Equation 2.1 becomes

$$I \approx \int_{h_r}^{h_E} \frac{\rho_m(h)dh}{\sqrt{1 - \frac{\cos^2 E}{(1 + h/R_E)^2}}} \qquad [2.5]$$

To derive the simplified shell model form, it should be noted that the TEC, $I_V(\theta_m, \phi_m)$, for vertical ray paths, E = 90°, can be written without approximation as Equation 2.6, because vertical ray paths have no horizontal variation of density

$$I_V(\theta_m, \phi_m) = \int_{h_r}^{h_E} \rho_m(h)dh \qquad [2.6]$$

Combining the exact (Equation 2.6) and the approximated (Equation 2.5) for TEC we obtain

$$I \approx I_V(\theta_m, \phi_m)M(E) \qquad [2.7]$$

where *M(E)* , the elevation scaling or obliquity function, is defined as

$$M_{TS}(E) = \frac{\int_{h_r}^{h_E} \frac{\rho_m(h)dh}{\sqrt{1-\frac{\cos^2 E}{(1+h/R_E)^2}}}}{\int_{h_r}^{h_E} \rho_m(h)dh} \qquad [2.8]$$

A commonly used obliquity factor is produced by assuming that $\rho_m(h)$ is non-zero only in the thin-shell region. Therefore the thin-shell factor is implicit and is given below:

$$M_{TS}(E) = \frac{1}{\sqrt{1-\frac{\cos^2 E}{(1+h/R_E)^2}}} \qquad [2.9]$$

Using these functions, the thin-shell model reduces the problem from three-dimensions (latitude, longitude and height) to two (latitude and longitude). For each ray path a unique shell-intersection point can be defined and so large-scale ionospheric maps can be produced. Gaps in data are dealt with by minimising the residual between vertical TEC estimates and those produced by the coefficients from the mapping functions.

2.3 Tomography

The second method is tomography, which, when first used, produced only two-dimensional images, but has now been shown to produce images in three and four dimensions. Here the basic theory used in tomography will be introduced and then review of the main developments in the past twenty years is given.

The approach uses TEC measurements between satellites and receivers to produce a system of linear equations, which must be solved to produce an image. Pixels of constant electron density are used to model the form of the ionosphere.

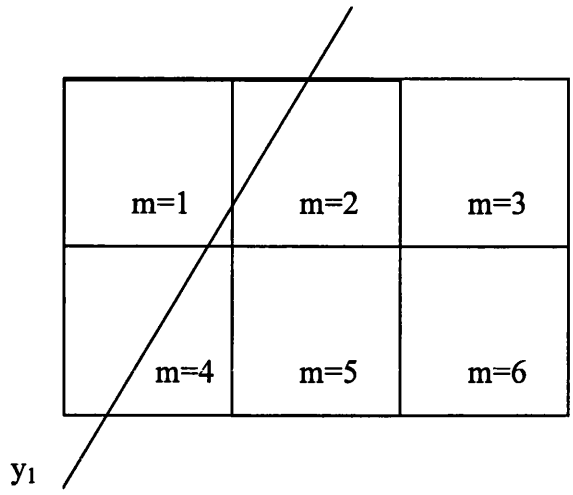

Figure 2.2. Basic tomography situation.

In general, the TEC, y, for a ray path, *i*, of element Δ through a grid is given by

$$y_i = \sum_{m=1}^{N} \Delta_m x_m \qquad [2.10]$$

Where m is the pixel index and N is the number of pixels in the grid

These equations generally cannot be solved using simple matrix inversion methods, as there are more unknowns than equations. Normally some prior knowledge must also be employed, (e.g. vertical distribution), along with the measurements of TEC, to produce an image.

To use tomographic imaging for dimensions greater than two–dimensions, a more complex configuration of receivers and satellites must be used to produce increased volume of data required. Measurements from the GPS are being used to an increasing extent for ionospheric research, due to the large number of receivers supplying data over the internet. GPS, discussed in Section 2.5 and the tomographic method that produces four-dimensional images is MIDAS Mitchell and Spencer (2003), used in this thesis, covered in Section 2.4.

Tomographic imaging principles were first developed in the early 20th century by Radon in 1917, but have only recently been used for ionospheric tomography due to the procedure's requirement for fast computers with large memories (Leitinger, 1999). As a concept it was first presented as a new technique at the International Beacon Satellite Symposium 1986 by Austen

et al. (1986), and published fully by Austen et al. (1988). This early technique was based in two dimensions and used a triangular vertical density profile, centred close to the simulated peak density, to compensate for the lack of vertical gradient information.

Experimental results showing a tomographic image of the ionosphere were first published by Andreeva et al. (1990). These used TEC data from three receivers based in Russia. Alternative sources, detailing the local ionospheric electron density were not available for comparison. It was not until 1992 that independent verification of a tomographic image was published by Pryse and Kersley (1992). Images were produced using two receivers in Sweden and Finland, using data from the USA Navy Navigational Satellite System (NNSS) and compared with images from the European Incoherent Scatter (EISCAT) radar. This experiment was improved a year later, Raymund et al. (1993), by using a chain of four receivers covering 10° of latitude. The comparisons showed good agreement, with similar troughs and enhancements observed by the two techniques.

Theoretical limitations of ionospheric tomography were published by Yeh and Raymund 1991, who highlighted the limitation in the geometry of the LEO satellite-to Earth configuration, due to the small number of viewing angles. The viewing angles are biased in a vertical sense, with no horizontal ray paths due to the curvature of the Earth. The constraint means that the vertical electron-content gradient is poorly defined by the TEC measurement alone and so prior knowledge must be used. Fremouw et al. (1992) use vertical orthonormal vectors from ionospheric models, and Hajj et al. (1994), use ray-paths between GPS and LEO satellites. Both of these approaches improve the vertical structure of the result.

Tomographic images of various ionospheric phenomena have now been produced. These include travelling ionospheric disturbances (Pryse et al., 1995), ionospheric troughs (Kersley et al., 1997), magnetic-field-aligned irregularities E-region enhancements (Mitchell et al., 1995) and also the northern crest of the equatorial anomaly in Italy (Materassi et al., 2001).

Recently 3D images and 4D movies have been developed to improve upon the 2D geometry produced from receiver chains. Bust et al. (2001) used the Ionospheric Data Assimilation 3D (IDA3D) algorithm, developed at CIC (Combined Ionospheric Campaign), to study the Caribbean region. MIDAS (Multi Instrument Data Analysis System) is another inversion technique, which uses various TEC measurements to map spatial and temporal distributions of electron density over wide areas. This technique has been used to produce global images at times of large geomagnetic disturbance.

Figure 2.3 shows the complex geometry for tomographic imaging, which uses a single low-earth-orbit (LEO) satellite and three ground-based receivers. The ionosphere is represented by a four by six array and only a few example ray paths are included.

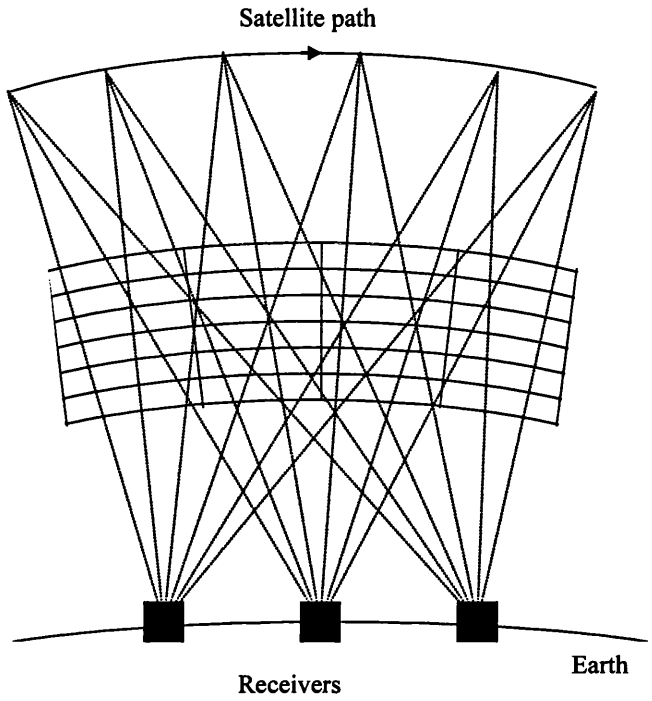

Figure 2.3. Idealised Geometry for tomographic imaging using polar orbiting LEO satellites.

2.4 Multi-Instrument Data Analysis System

The Multi-Instrument Data Analysis System (MIDAS) software was developed to generate images of the ionospheric electron concentration using line integral measurements of the relative TEC (Mitchell and Spencer, 2003). The first stage of the inversion is to set up a three-dimensional grid of voxels, each bounded in latitude, longitude and altitude, and to compute the length of each element of a satellite-to-receiver signal propagation path though each intersected voxel. For i TEC measurements and j voxels the unknown electron concentration is defined to be constant within each voxel and contained in the column vector **x**. The problem may now be expressed as,

$$\mathbf{Ax} = \mathbf{b} \qquad [2.11]$$

where **A** is an i by j matrix of the path lengths within each voxel and **b** are the i observed or simulated TECs. This cannot be solved directly as the matrix **A** is rectangular, highly singular

and sparse. It also incorporates no prior information as to the likely solution. To overcome this difficulty a mapping matrix, **X**, is used to transform the problem to one for which the unknowns are *n* coefficients of orthonormal basis functions, the combination of which will give the final image of electron concentration.

The choice of orthonormal basis functions is critical in the determination of the final solution to this underdetermined inversion problem. Here, the basis functions (**X**) were generated using a spherical harmonic expansion to represent the horizontal variation, and empirical orthonormal functions (EOFs) for the radial variation in electron concentration. The EOFs form a constraint to the vertical profile, only allowing a certain range of possible solutions.

This is now expressed mathematically as

$$\mathbf{AXW} = \mathbf{b} \qquad [2.12]$$

where the matrix **X** contains the basis functions, such that **AX** defines a basis set of line integrations of electron concentration. Since the ray-path integrals derived from differential phase measurements along the same satellite-to-receiver paths are subject to an unknown cycle offset, adjacent rows of the matrices **AX** and **b** can be differenced to negate the effect of this on the solution. The *n* unknowns, **W**, now represent the relative contribution of the basis functions where

$$\mathbf{W} = (\mathbf{AX})^{-1}\mathbf{b} \qquad [2.13]$$

Applying singular value decomposition to the matrix **AX** returns two orthogonal matrices **U** and **V** and a diagonal matrix of singular values, **w**. Here $(\mathbf{AX})^{-1}$ is a generalized inverse matrix such that **W** is the maximum likelihood solution. In this case singular value decomposition (SVD) has been chosen to solve the inversion, thus

$$(\mathbf{AX})^{-1} = \mathbf{V}(\mathrm{diag}(1/\mathbf{w})\mathbf{U}^{\mathrm{T}} \qquad [2.14]$$

The solution to the inverse problem is then given by

$$\mathbf{W} = (\mathbf{V}(\mathrm{diag}(1/\mathbf{w})\mathbf{U}^{\mathrm{T}})\mathbf{b} \qquad [2.15]$$

where the reciprocal of the terms in w that are sufficiently small, typically 10^{-7} of the dominant singular weight, are zeroed to account for degeneracy in the **AX** matrix. A description of the use of SVD can be found in Golub and Van Loan (1989). Finally, the electron densities within each voxel are recovered using

$$\mathbf{x} = \mathbf{XW} \qquad [2.16]$$

The inversion results in a four-dimensional image (3D space and time) showing the distribution of electron concentration, but for presentation purposes it is only possible to show static images of TEC, taken from frames of the movie.

MIDAS includes options for generating a variety of basis functions by combining empirical ortho-normal functions (EOFs) with spherical harmonics. The EOFs may be generated in one or three dimensions. In the one-dimensional case, EOFs are generated to represent the radial distribution of ionisation with the horizontal variations defined by spherical harmonics. An alternative option is to generate EOFs in three dimensions. These functions may then be used with or without spherical harmonic modulation. For each term in the basis set, it is possible to allow linear freedom in time such that the solution may evolve during the period of the observations.

For the inversions used in this thesis, MIDAS is configured to use three, one-dimensional EOFs, linear time evolution, and mapping functions that are centred on the geographic pole. The size of each voxel is 4° longitude, by 1° latitude, by 50 km in altitude. Input data are taken from ground-based GPS observations of differential phase divided into 1-hour windows. These are either obtained from a simulated ionosphere (using IRI-95) or from data downloaded from a geodetic network of GPS receivers (SOPAC)

The variables in the production of EOFs used in the TEC images in this thesis are given in Table 2.1.

Table 2.1. Parameters used for Chapman vertical profiles.

Layer	Chapman variables	Typical values
General F-region	Peak height / km (h_P)	{250, 300, 350, 400}
	Peak density (N_P)	1
	Scale height / km (H_P)	{30 50, 40 60, 50 80, 60 120}
	Profile power (B)	1
F1	Peak height / km (h_{F1})	{175, 200}
	Scale height / km (H_{F1})	30
	Fractional density (F_{F1})	{0, 0.2}
E	Peak height / km (h_E)	110
	Scale height / km (H_E)	20
	Fractional density (F_E)	{0, 0.1}
Topside	Fractional correction (F_T)	{0, 0.2}
	Asymmetry component (A)	{1, 2}

Using the parameters in the table the three layer heights (h_P, h_{F1} *and* h_E) can be defined where x corresponds to P, $F1$ and E dependant upon the layer.

$$z_x = \frac{h - h_x}{H_x} \qquad [2.17]$$

Thus the general vertical profile is created using exponential functions that define the distribution of the main peak, F1 peak, E layer and the topside variation, such that the main peak will have magnitude of 1.

$$\begin{aligned} N &= \exp(1 - z_P - \exp(-z_P)) \\ &+ F_{F1} \exp(1 - z_{F1} - \exp(-z_{F1})) \\ &+ F_E \exp(1 - z_E - \exp(-z_E)) \\ &+ T.F_T * [(1 - \exp(-z_P))^4] \end{aligned} \qquad [2.18]$$

T is a step function which masks heights below the F-peak such that

$$T(z_P) = \begin{cases} 1 \text{ for } h \geq h_P \\ 0 \text{ for } h < h_P \end{cases} \qquad [2.19]$$

$$N_{out} = N^B.N_P \qquad [2.20]$$

The combination of profiles for Table 2.1 results in set of 256 vertical profiles, which are orthogonalised using singular value decomposition to three EOF bases. This is the most efficient way of creating the vertical profiles. An example result is shown in Figure 2.4.

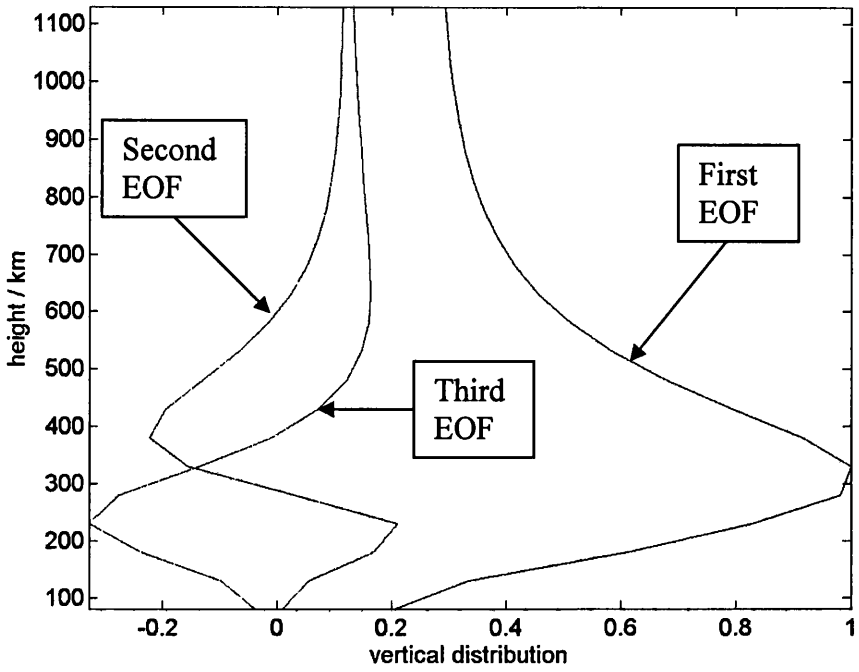

Figure 2.4. The normalised vertical distribution for the three EOF bases used to produce the vertical profile.

2.5 Global Positioning System

The Global Positioning System (GPS) is a satellite-based radio navigation system, developed and maintained by the US Department of Defence (DoD) and forms the basis of where the ionospheric data, input into the MIDAS algorithm. Its original aim was to provide position, velocity, acceleration and time information worldwide, although it has found many other uses since it reached full operational capacity in April 1995. One of these is the area of ionospheric research and a description of the system will be given. The following section is a description of the system's architecture, the technology it is based on, how positional information is gained, and known errors that contribute to positional inaccuracies.

2.5.1 System structure

The system can be divided into three major segments:

1. Space Segment, which produces the data required to calculate position, velocity, acceleration and time information. This consists of at least 24 operational satellites, currently 30, in six orbital inclined at 55° to the equatorial plane. All satellites broadcast a navigational signal over two L-band frequencies: L1 at 1575.42 MHz and L2 at 1227.60 MHz. The navigational signal contains information about the position and time when the signal was sent, along with known errors, such as the satellites clock differences from Universal Time (UT), the systems basis for synchronisation.
2. Control Segment, which continuously analyses the state of the system to correct errors that produce inaccuracies. This consists of five monitoring stations to measure the current status, a Master Control Station to process the information, and three antennas to transmit data back to the satellites.
3. User Segment, which contains receivers that decode the information contained within the transmitted signal for various applications. The accuracy of the data outputted depends upon the sophistication of the receiver. A basic receiver will only be able to use the civilian, L1 frequency, and therefore have a relatively low accuracy compared to a military receiver which has access to the second frequency and therefore improved error removal techniques at its disposal

Further information, about these three segments is available in Kaplan (1996) and Logsdon (1992).

2.5.2 Signal structure

The basis for the signals is the fundamental satellite clock frequency 10.23 MHz. The two carrier frequencies, L1 and L2, are obtained using frequency multipliers that increase the clock frequency by 154 and 120 times to produce each of the respective carriers. These carrier signals are sinusoids and therefore cannot be used for instantaneous positioning, as these will repeat every wavelength. The wavelength is much shorter than the distance between the satellite and the receiver, and as a result, this distance cannot be calculated without the addition of more information on the transmitted signal. Three binary codes, the C/A code (Civil coarse/acquisition code), P-code (Precision-code) and Navigation message, are added to the carrier frequencies to enable them to be used for accurate positioning by receivers. The

receivers recreate the transmitted signals and correlate these with the received signals until matches are produced.

2.5.3 Navigation solution

In this section, navigation principles using GPS are described. Figure 2.5 illustrates this problem. At least four satellites are required because the three coordinates (U_x, U_y, U_z) of the receiver must be calculated along with a fourth unknown, which is the clock bias (C_B), the difference between the receiver time and UT. The clock bias is required, as most receiver clocks only use quartz crystals. This means they are not as accurate as the atomic clock or synchronised to the satellite clocks and hence they are a source of positioning error.

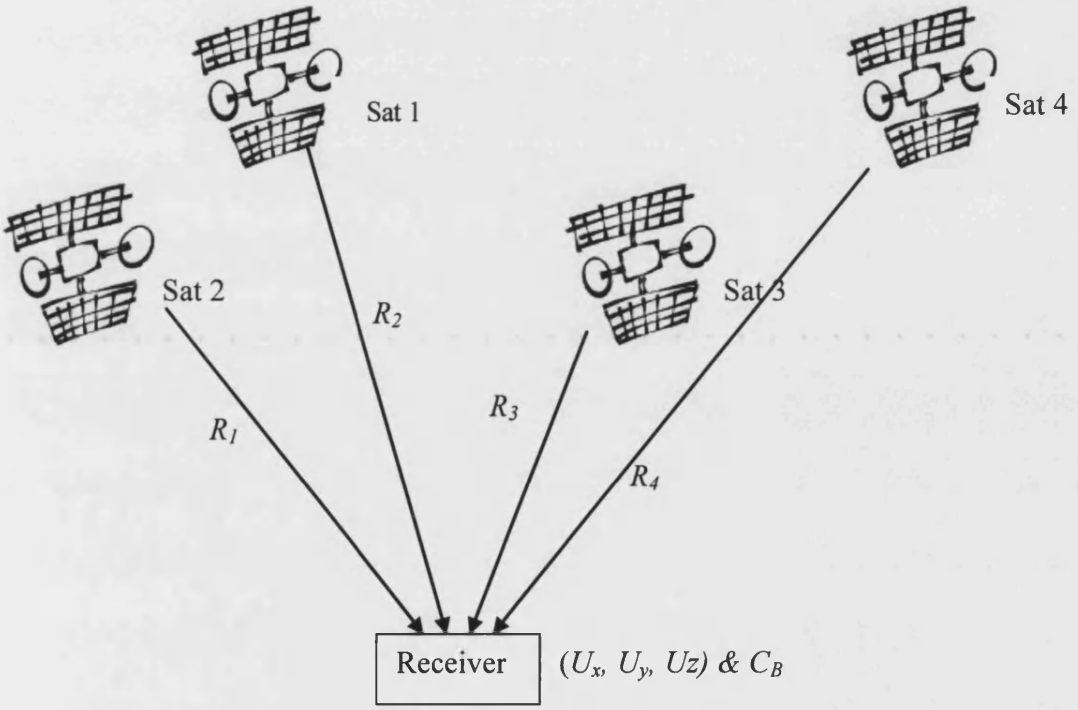

Figure 2.5. Diagram showing the GPS satellites and a receiver illustrating the navigation technique.

The receiver measures the signal path length (R_n) by comparing the signal received from the satellite to a predicted signal that the receiver constructs from its clock. The time delay between the two signals (t_n) can therefore be used to calculate the signal path length, assuming that the signal travelled at the speed of light, c, in a vacuum.

$$R_n = ct_n \qquad [2.21]$$

Four equations can be produced relating the positions of the satellites and the receiver, with the distance between them and the receiver clock bias using simple trigonometry.

$$(x_1 - U_X)^2 + (y_1 - U_Y)^2 + (z_1 - U_Z)^2 = (R_1 - C_B)^2 \quad [2.22a]$$

$$(x_2 - U_X)^2 + (y_2 - U_Y)^2 + (z_2 - U_Z)^2 = (R_2 - C_B)^2 \quad [2.22b]$$

$$(x_3 - U_X)^2 + (y_3 - U_Y)^2 + (z_3 - U_Z)^2 = (R_3 - C_B)^2 \quad [2.22c]$$

$$(x_4 - U_X)^2 + (y_4 - U_Y)^2 + (z_4 - U_Z)^2 = (R_4 - C_B)^2 \quad [2.22d]$$

These equations cannot be solved analytically as one result is not normally produced, but a small region where the receiver can be found and so a best result is produced instead using an iterative process that uses Taylor series expansions. This approach can range from a basic algorithm based only on the first order expansion, to the more complex versions using more derivatives of the variables to improve the speed and accuracy of the receiver position measurements.

2.5.4 Error sources

There are three major sources of error with GPS. The first is ephemeris error and occurs when a satellite deviates from its correct orbit. There are also errors with the satellite clocks, which drift over time as the hardware characteristics change as the satellite ages. These errors are included in the navigational message, they can be decoded and hence corrected for by a good receiver. The third major error is from the ionosphere, which produces an error related to frequency, f (Hz), and I, the TEC (electrons/m^2), described by Boithias (1983), where the positive result is the group delay and the negative is the phase delay. i corresponds to the two GPS frequencies, where 1 and 2 corresponds to L1 and L2 respectively.

$$\boldsymbol{Error} = \pm\frac{40.3\boldsymbol{I}}{\boldsymbol{f_i^2}} \quad [2.23]$$

Other error sources include tropospheric delay, multipath and receiver noise but these are negligible when compared to the other, larger errors.

Dual frequency receivers can eliminate the ionospheric error, but single frequency users use a model to help estimate what the error would be along a particular ray path. This normally reduces the positional error from the ionospheric delay by 50% and can be read in more detail in Klobuchar (1987). Other methods used by single frequency users to reduce the error are to use a number of GPS receivers, with known position, to calculate the error that is produced by ionospheric conditions by differencing the calculated and actual geographic position. Differential GPS (DGPS) uses one receiver and transmits the information to the local area. This method will become less accurate as the user' receiver and the correction receiver become further apart. Examples of large-scale systems are the Wide-Area Augmentation System (WAAS) network in Northern America or the soon to be operational European Geostationary Navigation Overlay Service (EGNOS). These use a network of ground based receivers, to calculate a map of positions errors for the area in question. These corrections use Satellite Based Augmentation Systems (SBAS), which use geostationary satellites to broadcast the corrections and improve positional accuracy of the user' receiver to below three metres.

2.5.5 How TEC is derived from GPS observables

A GPS receiver in the global network records two delay observables for each satellite being tracked. These are the pseudorange delay (P), and the carrier phase delay (L). These are acquired on both GPS transmission frequencies, f_1 and f_2, and produce four observables, which are governed by the following equations, (Mannucci et al., 1999).

$$P_1 = \sigma + \frac{40.3 * I}{f_1^2} + \tau_1^r + \tau_1^s \qquad [2.24]$$

$$P_2 = \sigma + \frac{40.3 * I}{f_2^2} + \tau_2^r + \tau_2^s \qquad [2.25]$$

$$L_1 = \sigma - \frac{40.3 * I}{f_1^2} + \lambda_1 n_1 + \varepsilon_1^r + \varepsilon_1^s \qquad [2.26]$$

$$L_2 = \sigma - \frac{40.3 * I}{f_2^2} + \lambda_2 n_2 + \varepsilon_2^r + \varepsilon_2^s \qquad [2.27]$$

Each observable depends upon a non-dispersive delay term, σ, which combines the geometric distance, troposphere delays, clock errors, and non-dispersive delays in the hardware signal paths. The carrier phase terms have an integer cycle ambiguity ($\lambda_1 n_1, \lambda_2 n_2$), where n_1 and n_2 are generally unknown, and λ_1 and λ_2 are the carrier wavelengths. The possibility of integer phase jumps can be removed using a detection algorithm, (Blewitt, 1990).

The ionospheric delay terms from Equation 2.26, are dependent on the signal frequency, f_i, and the TEC, I, and effects the phase and range observables with opposite sign. The remaining terms, ε and τ, are the dispersive components of the satellite and receiver hardware delays. The ionospheric combination for both range observables is formed by frequency differencing the equations for each observable.

$$P_I \equiv P_2 - P_1 = 40.3(1/f_2^2 - 1/f_1^2)I + IFB_R + IFB_S \qquad [2.28]$$

$$L_I \equiv L_2 - L_1 = -40.3(1/f_2^2 - 1/f_1^2)I + (\lambda_1 n_1 - \lambda_2 n_2) + IFB'_R + IFB'_S \qquad [2.29]$$

where the interfrequency biases have been expressed as single receiver, IFB_R, or satellite terms, IFB_S. These biases exhibit a gradual drift over several months (Wilson and Mannucci, 1993, Sardon and Zarraoa, 1997) and can be solved for, during the ionospheric imaging process (Mannucci et al., 1998). Using differential carrier phase measurements, TEC can be found using a period of satellite observations. Phase jumps, caused by cycle slips, can be removed and biases are assumed constant during this period. The signal frequencies are also known so all that is left are the TEC measurements for the period of data.

2.6 Alternative ionospheric data sources

A final section will deal with other sources of ionospheric measurements used in this thesis.

2.6.1 Ionosondes

An ionosonde consists of a transmitter and receiver in close proximity. Frequencies between 1 and 20 MHz are produced and sent in the form of pulse vertically. The ionosphere refracts these

signals dependant upon the frequency of the signal and the receiver measures the time delay between the transmission of the pulse and the frequencies return. By plotting the detected frequencies in the range sent in the original pulse, against the time difference between the signals transmissions and the arrival at the receiver, an ionogram is produced. Automatic measurements can be produced for the height and critical frequency of the major layers of the ionosphere. Two heights are normally outputted. The first is an apparent height and the second is an actual height using a parabola to represent the actual path of the signal. Figure 2.6 shows the difference between the apparent height and the actual height. The apparent height is produced by assuming that the signal reflects off a shell by multiplying the speed of travel of the signal, c, by half of the time between the produced pulse and the time of arrival at the receiver. Other measurements include the maximum usable frequency (MUF), the highest frequency that will return to Earth.

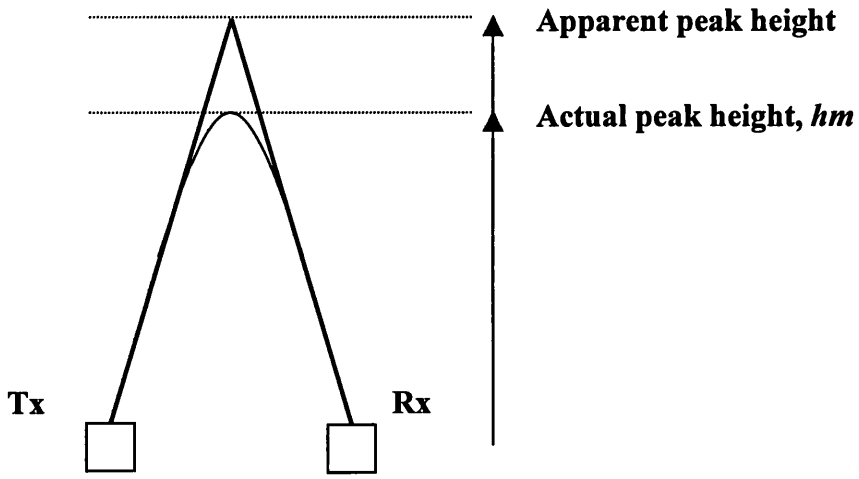

Figure 2.6. Difference between apparent and actual peak height.

Ionosondes normally produce a result every 15-minutes or every hour and a number of ionosonde results can be used to reconstruct wide-area images of the derived parameters. Ground-based ionosondes will only produce information for the ionosphere for the F2-peak height and below and so will not include the topside information. Orbiting ionosondes or other sources of data, such as GPS or ionospheric models, can be used to provide the additional information required to produce maps of parameters such as the vertical TEC.

Chapter 3 Prediction Techniques

3.1 Introduction

In this chapter, a review of various ionospheric modelling and forecasting techniques is given. Several modelling approaches that use many years of ionospheric measurements to predict trends in the ionosphere are introduced. These can be trends in the actual state of the ionosphere, by modelling long term variations such as the solar cycle, or trends in the variation of the ionosphere by modelling the physical interactions and concentrations of the various particles which make up the ionosphere. These models produce good approximations of the average state of the ionosphere given a set of particular parameters. However, more accurate representations of the ionosphere are produced by forecasting short periods ahead from accurate ionospheric measurements. Techniques that achieve this, including methods such as neural networks and mathematical algorithms, are introduced. These techniques are for wide-area maps, as well as single site data sets.

3.2 Empirical models

Empirical models are formed from a variety of data sources collected over a long period of time. They use instruments such as ionosondes, incoherent scatter radars or satellites and sort the results into various bins according to appropriate indices so that a best-fit approximation can be found using analytical expressions or orthogonal functions. Although, this approach will only produce an average result when used to predict the ionosphere, it can be used with certain assimilation methods described later in this chapter, by including recent measurements to increase their accuracy. One example of an empirical model is the International Reference Ionosphere (IRI) (Bilitza, 1990).

3.2.1 International Reference Ionosphere

The IRI is an international standard for the specification of ionospheric electron densities and temperatures, developed by a joint working group of the International Union of Radio Science (URSI), and the Committee on Space Research (COSPAR) (Bilitza et al., 1993). The group started in the late 1960s, and released the first program in 1978 (IRI-78). The group has updated this software many times, with the latest program released, at time of writing, in 2000. The results from the program give 3D, monthly median representations of the ionosphere. It has

been used as an input test structure for various systems to help model the effect of the ionosphere on signals that propagate through the medium.

Originally the major source of data for the IRI model was a report produced by the Consultative Committee of International Radiocommunications (CCIR). This report used data obtained from 13 ionosondes collected over a period of five years in the late 1950s. Ionospheric maps for various important ionospheric peak parameters were produced, along with models to describe the ionosphere's critical frequencies and propagation factors. These can be used to produce peak densities and heights for the major ionospheric layers and so produce a basic prediction of the ionosphere. These maps have been updated in recent versions of the IRI software as they originally covered only the low to medium part of the solar cycle. Fourier coefficients for 12-month mean sunspot number, R12, equal to 0 and 100 have been published. CCIR recommend using a linear relationship for these coefficients to the mean sunspot number when reconstructing the electron density field (12-month mean of monthly sunspot number).

The IRI model is continually being improved through yearly workshops. The main aim now is to produce a better vertical representation of the ionosphere. Other features are also being added to the program to help improve the accuracy. In the most recent version of the program, an algorithm to describe storm-time variation has been included and a further addition in the future will be a trough model once a single, global algorithm describing the movement has been verified.

The data produced by the IRI software can be used for various applications in the ionospheric community. Some examples of the uses of the IRI model include:

1. Ionospheric corrections for satellite altimeter measurements.
2. A background ionosphere for testing GPS data analysis and data reduction algorithms.
3. As an initial guess for a tomographic technique to reconstruct ionospheric images.
4. High Frequency (HF) propagation estimates.

3.3 Physics based models

Physics based models use momentum and energy equations for the ions and electrons present in the ionosphere along with other formulae evaluating other influences, such as chemical processes. Information describing the current state of the magnetosphere and atmosphere must also be obtained to produce an accurate result. The data for these inputs are obtained in two separate ways.

The first is called a Data-Driven Physics-Based model and uses measurements from various sources to obtain the required information. Some of these data sources are very rare and so empirical models are more commonly used to predict these (Schunk et al., 2002).

The second type is called a Coupled Physics-based model. These link physics based models for different regions of the atmosphere such as the plasmasphere, mesosphere and the magnetosphere. An example of such a model is the Sheffield Coupled Thermosphere-Ionosphere-Plasmasphere (SCTIP) model, which combines the University College London (UCL) thermosphere model with models produced by Sheffield University (Millward 1996). Physics-based models are not used in this thesis because they do not accurately specify current conditions; they are more useful for scenario testing in physical investigations.

3.4 Parameterised models

Parameterised models use orthogonal function to fit to data. The difference from empirical models is that results are produced from physics-based ionospheric models, rather than from measured data. This means that outputs can be computed quickly, but some use is still made of the physics of the theoretical models. The Parameterized Ionospheric Model (PIM) is a good example of such a model. It was develop under the direction of the US Air Force Research Laboratory (AFRL). More information can be found in Daniell et al. (1995). Also the Simplified Ionospheric Regional Model (SIRM) (Zolesi et al., 1996) has been used as the basis of work which adapt this model with real-time data, (Zolesi et al. (2004) and Tsagouri et al. (2005)) to produce real-time values of foF2 data using SIRMUP, the SIRM Updating model.

3.5 Data assimilation models

Data Assimilation is increasing in use because of the improving availability of ionospheric measurements. Data from various sources are input into first principles models to produce an output estimate of the ionospheric conditions. Ionospheric models can help to compensate for regions of missing data. A Kalman filter can perform this task as it can combine information from models, statistical description of uncertainties, and the ionospheric data, to produce the ionospheric estimate. Models, such as IRI, can be used to produce an initial state for the ionosphere, then for later time steps, the previous output can be used as the initial guess. An example of a data-assimilation technique is GAIM (Global Assimilative Ionospheric Model), which is being developed by the University of California and JPL (Hajj et al., 2002). GAIM

uses GPS data, LEO occultation data and UV irradiance measurements to produce an ionospheric specification.

3.6 Ionospheric forecasting

There have been various approaches used to forecast the ionosphere and in this section a review of these methods is given. They consist of two main approaches. The first to be shown will be neural network (NN) methods, which are trained with a data set before forecasting the medium. The second approach use forecast algorithms derived from long-term data sets.

Baker et al. (1990) first demonstrated the importance of non-linear behaviour within the solar environment. Non-linear theoretical models and non-linear time series methods were then developed to characterise the behaviour of complex systems such as geomagnetic activity by Kilmas et al. (1992), and coupling of the solar wind with the magnetosphere (Vassiliadis et al., 1995). From these, attention was then turned to methods derived from studies into artificial intelligence and the application of NN-based techniques (Francis et al., 2000).

The use of NN-based techniques for predicting parameters affecting the ionosphere were first seen in 1992 when Lundstedt (1992) showed the ability of NN to predict geomagnetic activity. Their ability was further shown by Lundstedt and Wintoft (1992) and Wu and Lundstedt (1996), who both used them to forecast the DST (Disturbance Storm Time) index, from solar wind measurement.

In 1996, the first use of NN methods to predict the ionospheric parameter foF2 were presented by Williscroft and Poole (1996). This predicted the noon value of foF2 and used season, solar activity and magnetic activity over a complete solar cycle as inputs. Progress was continued by Lamming and Cander (1997) and Cander et al. (1997), who predicted the monthly median value of foF2. By 2000 the complexity of the NN had been improved to produce prediction of hourly and daily time-scales, by Francis et al. (2000). Results showed there was a significant improvement when compared to standard persistence and 24-hour recurrence methods.

The use of NN methods has mainly focussed at predicting the ionospheric parameter foF2. Mitchell et al. (2000), presented NN performance at predicting TEC over a 1 year-period, compared with various mathematical approaches for time-scales of 30 minutes, 1 hour and 3 hours ahead. The methods employed were persistence, percentage persistence gradient and percentage gradient matching (PGM). These methods form part of the investigation in Chapter 6. The NN used is detailed in Francis et al. (2000). They found that PGM could be used to give

equal or better prediction errors compared to the NN during quiet and disturbed conditions. In addition, methods such as 24-hour persistence, are not suitable at disturbed times. PGM has certain advantages over NN as it does not require a specific training period, and can be performed on any time series of TEC of length greater than one day.

A study using autocovariance prediction methods between 1 and 12 hours ahead, showed that they could be used for foF2 data, (Stanislawska and Zbyszynski, 2001). Results of that study showed good improvements on monthly medians and persistence. In a continuation of this procedure predicting TEC, Stanislawska and Zbyszynski (2003) recorded less promising results with algorithm forecasts 1 hour ahead producing results of worse accuracy than persistence.

All results presented so far have used single site forecasts. Larger scale prediction services include Rutherford Appleton Laboratory (RAL) and Center of Orbit Determination in Europe (CODE). Both of these produce large-scale foF2 maps of Europe and globally, respectively. RAL has used a simple auto-regressive model, Dick et al. (1999) in their Short-Term Ionospheric Forecasting (STIF) tool. This produces estimates of ionospheric parameters, foF2 and MUF(3000)F2, which are input, with models of other ionospheric parameters into a TEC profiler. This system can be used to predict for periods longer than 24 hours ahead. They conclude that the STIF tool is a more reliable tool than persistence for quiet and storm conditions.

CODE produce Global Ionospheric Maps (GIMs) using data from more than 110 stations of the International GNSS Service (IGS), (Schaer et al., 1998). From past images produced by the Bernese Processing Engine, predictions are made, using spherical harmonic parameters that create the GIMs, for the next 48-hours, at two-hour intervals. Only long, prominent periods are used for the harmonic expansion of the trend line (11, 1 and 0.5 year periods), and so short-term fluctuations are not predicted.

Chapter 4 Study of imaging accuracy by simulation and comparison with ionosonde measurement

4.1 Abstract

In this chapter, the accuracy of images of the ionosphere over Europe is studied. The accuracy of the images must be verified because they will form the basis of the forecasting work in subsequent chapters. Firstly, the image accuracy is tested with a simulation of the imaging technique using the IRI model ionosphere and actual GPS receiver and satellite configurations. Experimental GPS phase data are then used to image the electron density during a period of disturbed geomagnetic activity during April 2002. These results are compared to independent measurements from three ionosondes located across Europe, and confirm an underestimate in peak electron density that was found in the simulation. The accuracy of the imaged peak electron density accuracy is shown to improve across the image when isolated measurements from ionosondes are included in the inversion process. The TEC produced was unaffected by this approach. The results show that both TEC and peak electron density accuracy can be achieved when both GPS and ionosonde data are used in a single inversion method.

4.2 Simulation of the imaging method

The tomographic method used by MIDAS is covered in Section 2.4 with the general parameters used in the reconstructions given in Table 2.1. The method to simulate TEC data, in the form of the ionospheric delay, is explained here.

Realistic representations of the ionosphere are used to simulate the electron density over the European region. For this the IRI model was chosen (IRI-95). To make the simulation realistic receiver and satellite positions need to be produced which relate to real world situations. Receivers and satellite positions were obtained from the database provided by the International GNSS Service (IGS). A map of the receiver sites in Europe is shown in Figure 4.1. In addition, the satellite positional information is provided by IGS at 15-minute intervals but slant TEC information is required every 30-seconds. For this reason, positional data were produced over 30-second intervals by using linear interpolation.

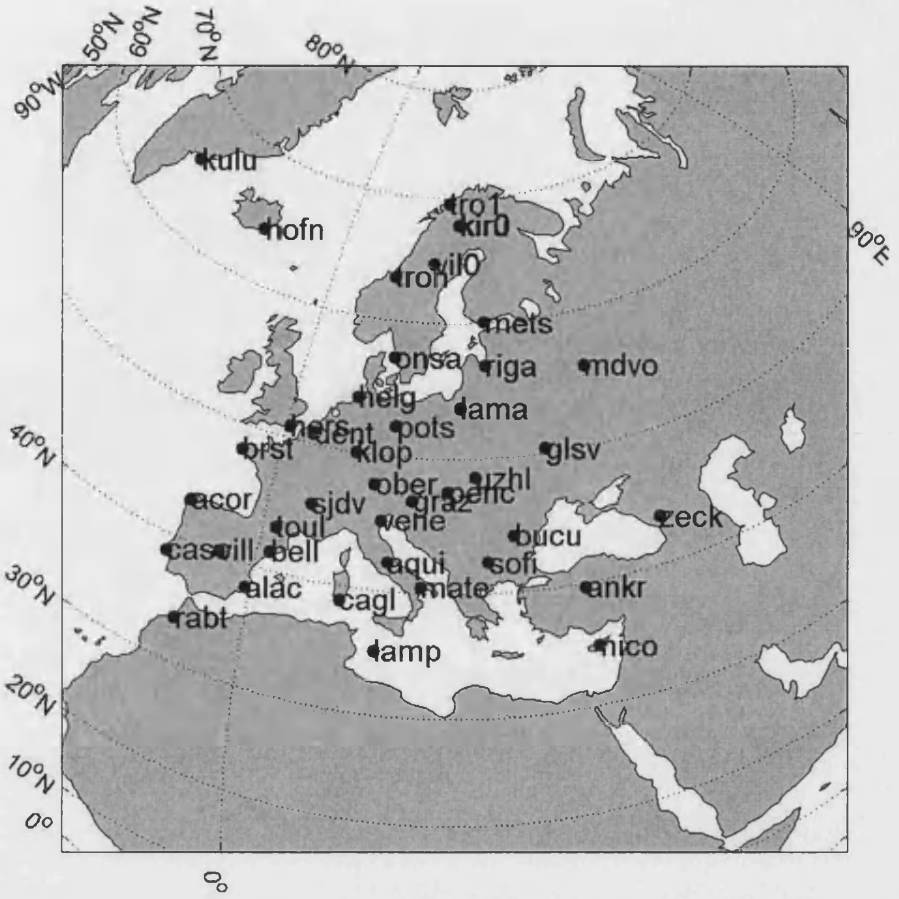

Figure 4.1. Locations of the GPS receivers used by MIDAS.

4D representations of the ionospheric model were produced for each hour. Numerical integration through these images, between each satellite position and each receiver in view of that satellite, allows the calculation of slant TEC values, b, for each specific satellite and receiver, b_{sr}. In Equation 4.1, **A** is a vector that contains measurements of the path lengths though each voxel, and $\mathbf{IRI}_{Ne}$, the electron density in each voxel given by the IRI model. If a particular ray path crosses M voxels, then each simulated measurement is the TEC through the IRI model.

$$b_{sr} = \sum_{l}^{M} A(IRI_{Ne}) \qquad [4.1]$$

The inversion was performed using the MIDAS algorithm described in Mitchell and Spencer (2003) (see Section 2.4). The inversion results in a 3-D movie showing the distribution of electron concentration. For presentation purposes it is only possible to show static images of TEC, taken from frames of the movie. In experimental studies the GPS phase data from the

database provided by the IGS, Scripps Orbit and Permanent Array Center (SOPAC) is used as input instead.

An example of this process is now shown. The chose time is the hour between 0800UT and 0900UT for February 15th 2002. Figure 4.2 shows an image of the IRI-95 model ionosphere for 0830UT. The particular hour is where the TEC of the ionosphere is increasing rapidly as the Sun moves to higher elevations.

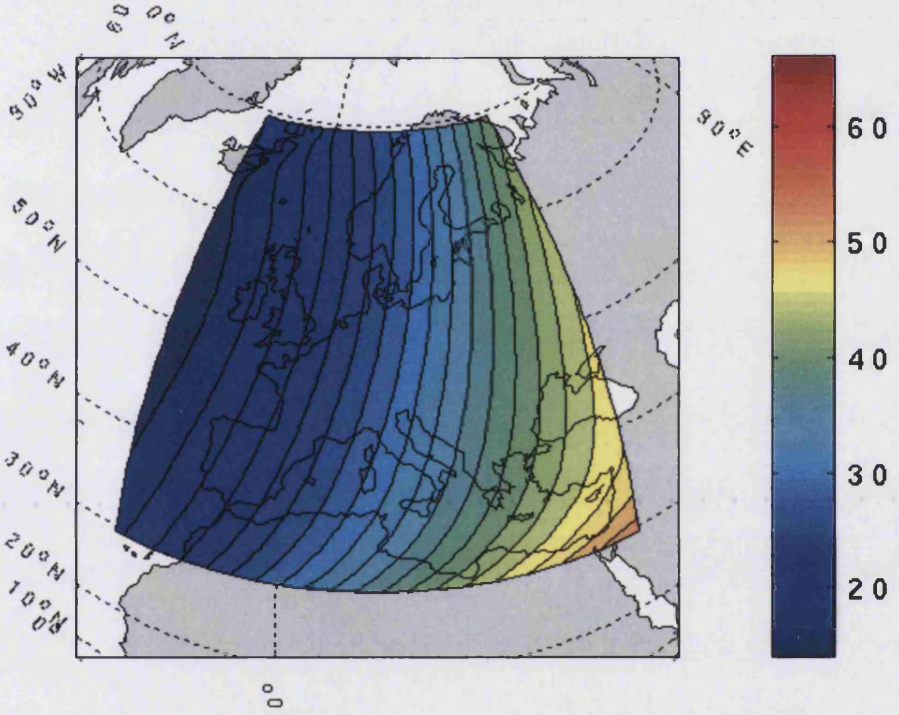

Figure 4.2. IRI model TEC at 08:30UT for February 15th 2002.

The simulated data shown in Figure 4.2 are then used to produce a set of slant TECs between the set of satellites and receivers. Figure 4.3 shows a representation of the hour of simulated MIDAS input data commencing at 0800UT. In the plot, the intersection of each ray path with a 400 km shell is shown with the slant TEC approximated to the vertical TEC at that point. Differences exist between the two figures because an approximation to represent the slant TEC as a vertical TEC is used in Figure 4.3

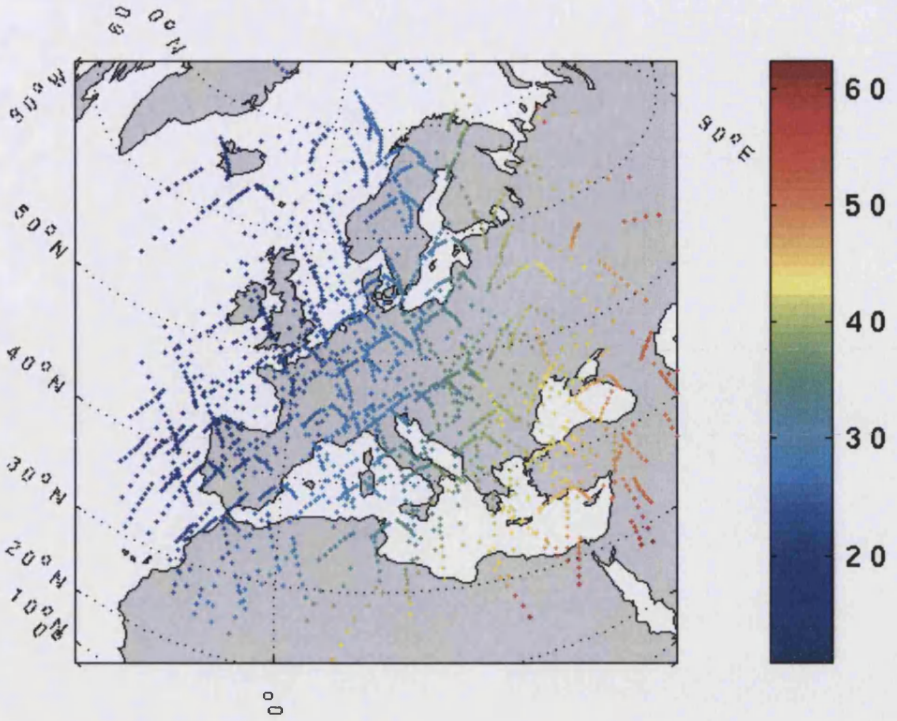

Figure 4.3. TEC calculated by integration between satellite and receiver through the IRI model for the hour commencing 08:00UT on February 15th 2002. Each point shows the intersection of the ray path with a shell at 400 km approximated to vertical TEC at that point.

The simulated slant TEC values are then used as an input to MIDAS, which produces a one-hour movie of electron density. Figure 4.4 shows the centre image of this movie and it can be seen that the input image, Figure 4.2, and the output inversion result, Figure 4.4, are similar which indicates that MIDAS is accurately recreating the ionosphere in terms of the vertical TEC.

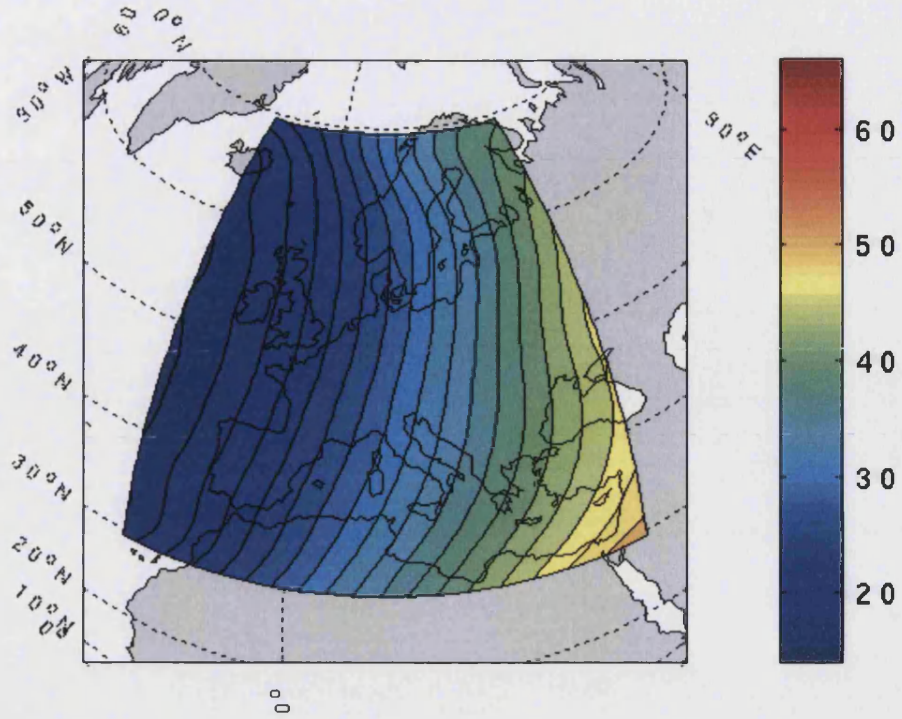

Figure 4.4. MIDAS inversion using the simulated IRI slant TEC input at 08:30UT for February 15th 2002.

Using simulated and then subsequently actual GPS TEC data, three representations of the ionospheric electron density are produced for each hour:

1) The IRI model (or MOD)
2) The MIDAS inversion using the IRI model as input (or INV)
3) The MIDAS inversion using actual GPS phase data (or REAL)

Two quantities are used for assessment of the images. One is the vertical TEC, at each latitude and longitude, produced by summing the electron densities in a vertical column. The second is the peak electron density or the F2-peak, found by calculating the maximum electron density in each vertical column of voxels.

4.3 Simulation results

Firstly, an investigation is undertaken to analyse the accuracy of TEC measurements over the image region using the MOD and INV datasets. The vertical TECs for these two datasets are calculated for the European region for January 2002 between latitudes, 20°N and 80°N, and longitudes, 10°W and 70°E. This represents the entire imaging region of the reconstructions.

The mean TEC was calculated for the month along each line of voxels in the latitude and longitude direction for each of the two datasets. Figure 4.5 shows these averages for each voxel in the latitudinal direction, and Figure 4.6 shows the averages along each line of voxels in the longitudinal direction. In these plots the solid line shows the results for the input ionospheric TEC, the MOD data, and the dashed line is the TEC from the output result from the MIDAS inversion.

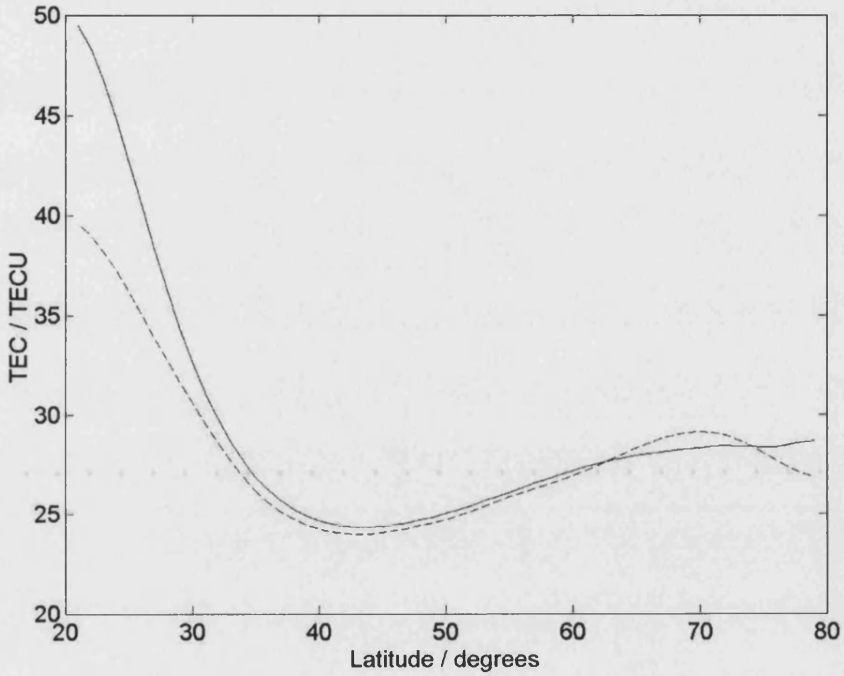

Figure 4.5. Comparison between IRI input (Solid line) and MIDAS inversion output (Dashed line) over European latitudes in January 2002

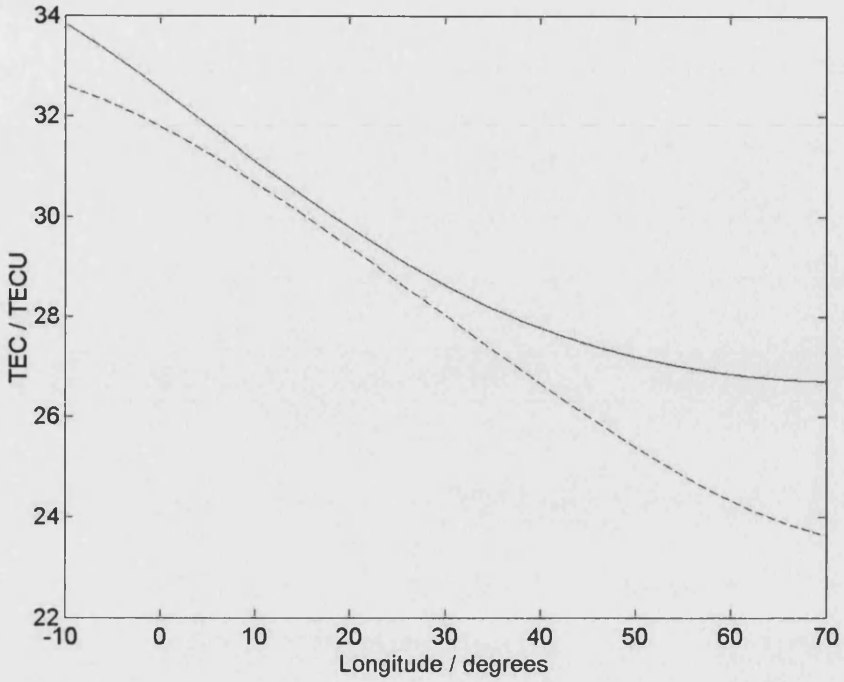

Figure 4.6. Comparison between IRI input (Solid line) and MIDAS inversion output (Dashed line) over European longitudes, January 2002.

In both figures, it is clear that the results are less accurate at the edges of the region than at the centre. The satellite-receiver ray paths do not cover these regions, either due to receiver availability on satellite constellation limitations. Therefore MIDAS does not have the input data required to image accurately over these regions as there are minimal ray paths traversing the ionosphere.

To produce results that do not use regions where there are few or no input satellite-receiver ray paths, data from the northern, southern and eastern edges of the image are removed. The image region used covered latitudes between 30°N and 65°N, and longitudes 10°W and 45°E. Results using this reduced imaging region are shown, with Figure 4.7 showing the latitudinal averages, and the Figure 4.8 showing the longitudinal results for the two sets.

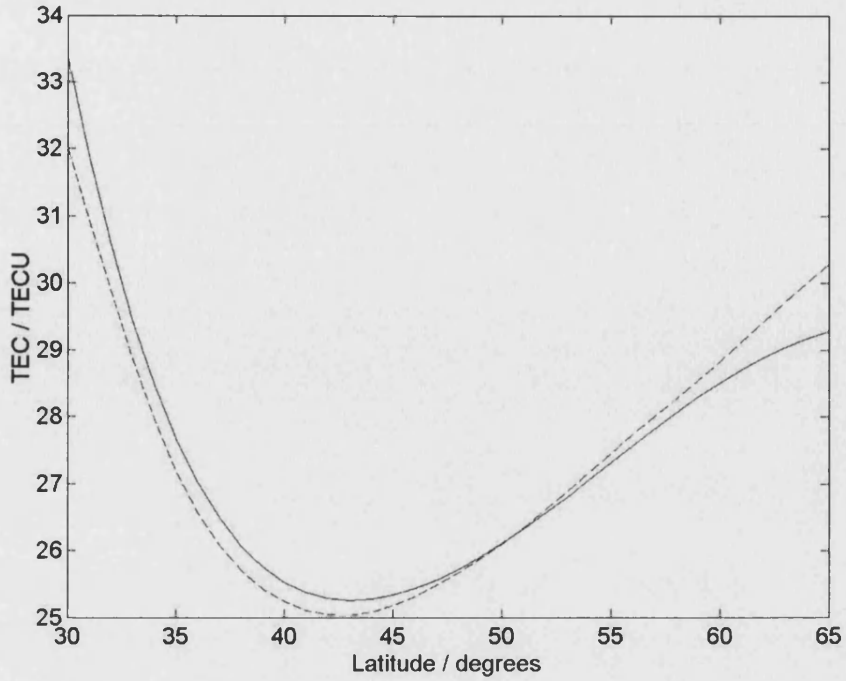

Figure 4.7. Comparison between IRI input (Solid line) and MIDAS inversion output (Dashed line) over selected latitudes (30°N to 65°N) in January 2002.

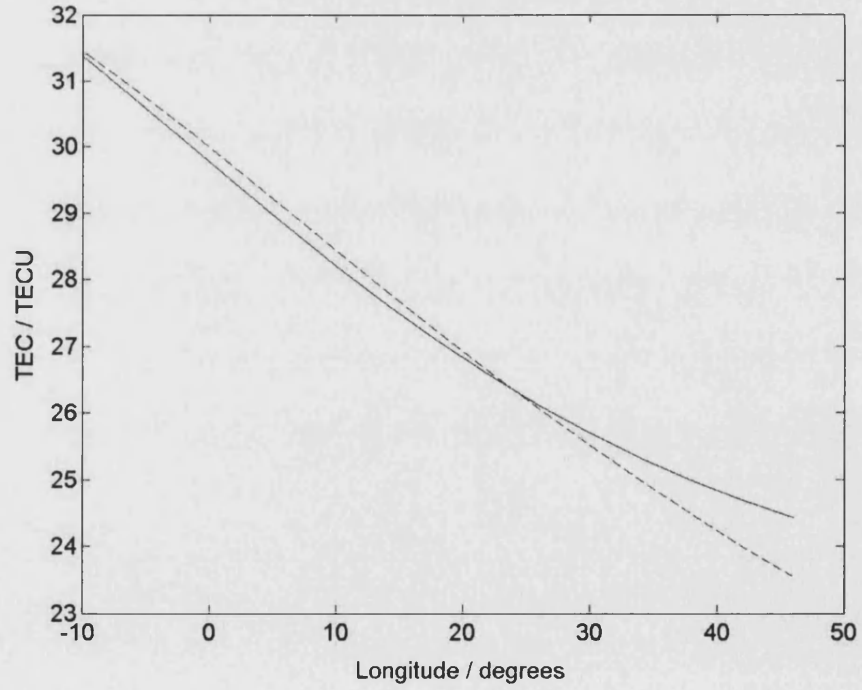

Figure 4.8. Comparison between IRI input and MIDAS inversion output for selected longitudes (10°W and 45°E) in January 2002.

It can be seen that the comparison is greatly improved, and shows that MIDAS is accurate where there is a high density of GPS phase data for input into the inversion. With these inaccurate areas removed from the analysis region, the simulation results can be studied further.

A comparison of the MOD and INV datasets using the smaller image region is now shown. Figure 4.9 shows the direct comparison of the model ionosphere, MOD, and the output images, INV, using the mean TEC across each of the images for each hour of the year 2002. It can be seen to be a very good correlation with a coefficient of +99.9% and mean, absolute mean and rms errors of -0.14, 0.41, 0.56 TEC units, indicating a very slight underestimate.

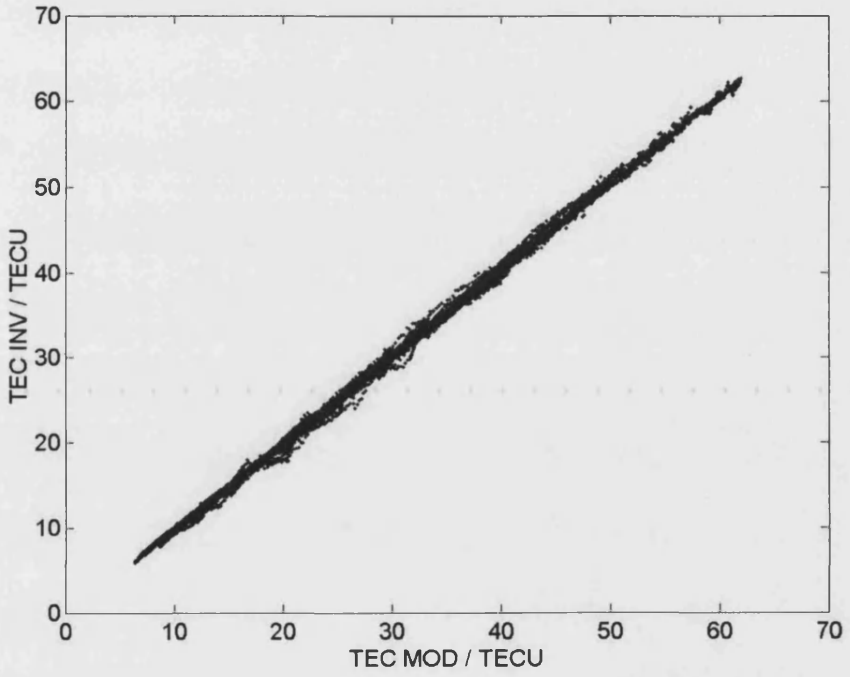

Figure 4.9. The mean hourly vertical TEC over Europe for each hour of 2002. The graph shows the inversion value against the IRI model value in TEC units (1TECu = 10^{16} e m^{-2}).

A smaller section of the hourly variation of vertical TEC over Europe at the time of a geomagnetic disturbance in April 2002 for all three data sets, MOD, INV and REAL, was then studied. The period used, from the 16th to the 25th, shows a large increase of magnetic activity. The highest K_p index values for the days used, 16th to 25th, are 3-, 7+, 7, 7-, 7+, 2+, 4, 6, 3+, 2. Figure 4.10 shows the hour mean of the three data sets with the MOD (dashed line), INV (dotted) and REAL (solid) hourly data.

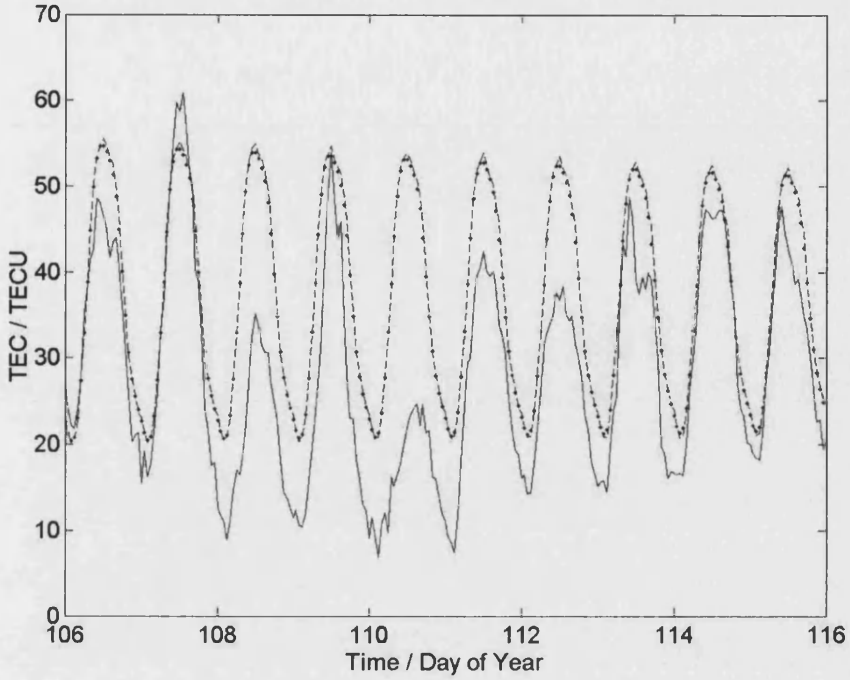

Figure 4.10. Mean hourly TEC during April 2002 storm for MOD (Dashed line), INV (Dotted line) and REAL (Solid line) datasets.

The MOD and INV data lines follow each other closely whereas the REAL data is more varied due to the effects related to the geomagnetic storm onset. The mean, absolute mean and rms error between MOD and INV for the daily mean TEC was 0.18, 0.69 and 1.01 TEC units. These low errors show that MIDAS can reconstruct the model ionospheric TEC to an accurate level.

In order to look at longer-term variations between the model and actual GPS real data, daily mean TEC values are compared. Figure 4.11 shows this daily mean TEC over Europe for the MOD (dashed) and REAL (solid) data sets. Large day-to-day variability can be seen in the values from the REAL data, as expected. However, the longer-term variations are well replicated by the IRI model, although some under representation in the winter and over in the summer can be seen by the model.

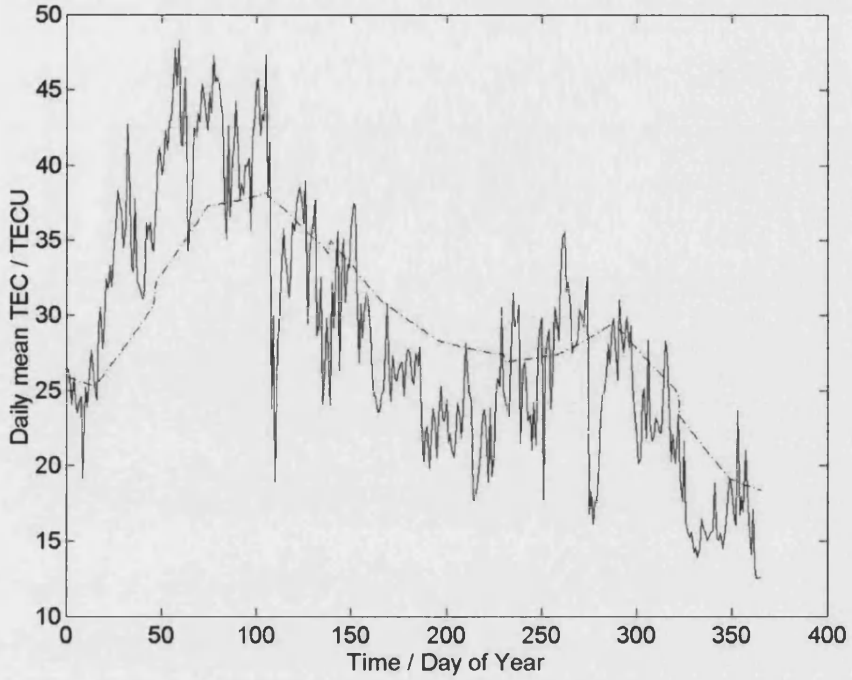

Figure 4.11. Daily mean TEC for 2002 over Europe for MOD (Dashed line) and REAL (Slid line) datasets.

The simulation gives a good indication of the accuracy of the imaging technique, but it is limited because the ionospheric model does not follow the day-to-day variability of the ionosphere. The model only uses 12-month running averages of input parameters so this is expected as they cannot reflect short-term variations. The imaging method must be verified using actual data but it is not possible to find independent and accurate estimates of vertical TEC. Instead, the MIDAS results are compared with ionosonde peak electron densities.

The next step is to test whether MIDAS can produce vertical profiles of electron density accurately by examining the simulation results. For this the peak electron density, at the latitude and longitude corresponding to the location of the Rome ionosonde, was found for the MOD and INV data sets. The latitude and longitude of the ionosonde are 41.8°N and 12.5°E respectively, so the nearest voxel, at 42°N and 14°E, was used. Figure 4.12 shows a direct comparison of the model to the inversion peak electron density for each hour of a ten day period, 16th to 25th April 2002, with the dashed line demonstrating a perfect correlation.

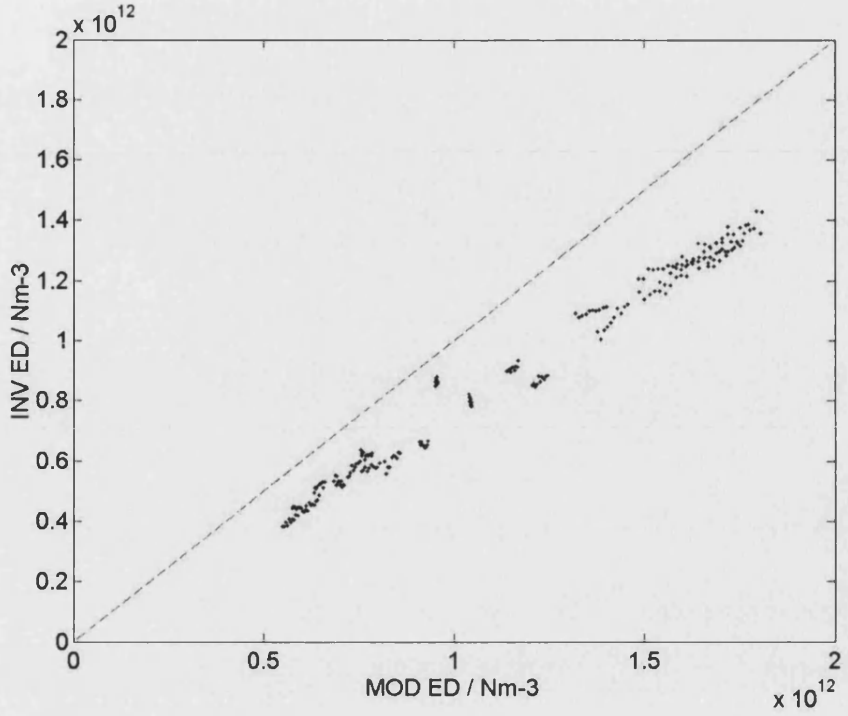

Figure 4.12. Comparison of peak electron density from MOD and INV at Rome.

The MOD and INV have a high correlation, 99.1%, but it can be seen that the imaging consistently underestimates the actual peak electron density value. The gradient of the least-squares-fit was calculated to be 0.78, with a very small offset of -1.45×10^{10} Nm^{-3}. Since the TEC do not show this large underestimate, this result is due to a combination of a larger scale height and a lower peak density. Hence, the integrated values of electron density (TEC) can be correct despite the inaccurate vertical profiles. This can be seen in Figure 4.13 where the vertical profile of the MOD (dashed) and INV (dotted) data are compared at Rome at 1230 UT, day 10th April, 2002.

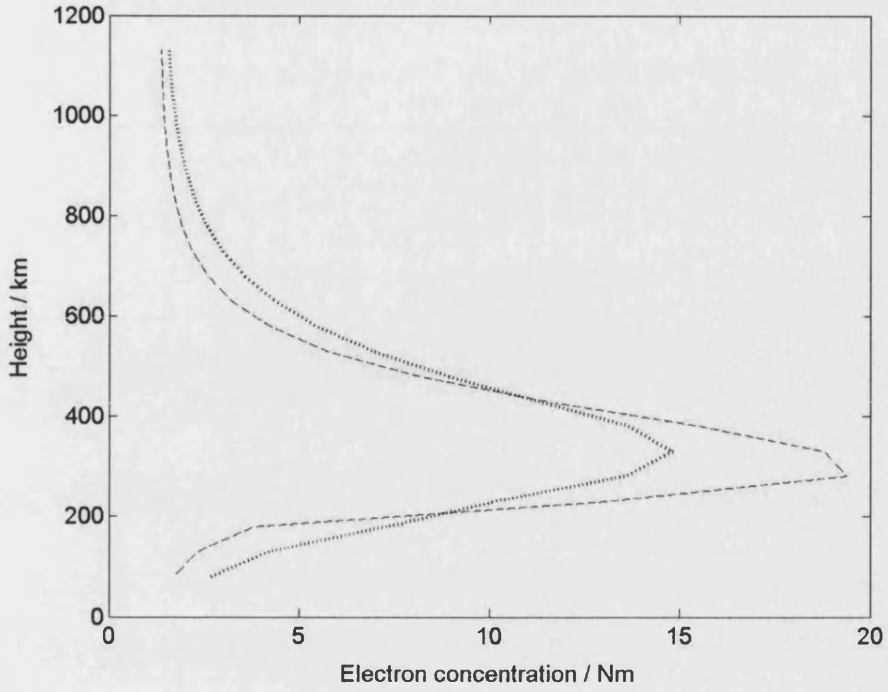

Figure 4.13. Comparison of MOD and INV vertical profiles for Rome, Italy. The dashed line shows the MOD profile and the solid line shows the resultant INV profile.

4.4 Peak density comparisons using GPS data

In this section, the underestimate in peak electron-density is tested using the REAL data set, compared with the actual peak electron density values calculated using the results from the Rome ionosonde, along with others in Europe. This will show whether the generic set of Chapman profiles are appropriate for the real ionospheres under question, and not for only simulation. The foF2 is the measurement of the frequency of signals, which reflect from the F2-layer peak. Data of foF2 from ionosondes in Italy (Rome), Bulgaria (Sofia) and Spain (Tortosa) were obtained from Space Physics Interactive Data Resource (SPIDR) website (http://spidr.ngdc.noaa.gov/spidr). The locations of these ionosondes are shown in Figure 4.14.

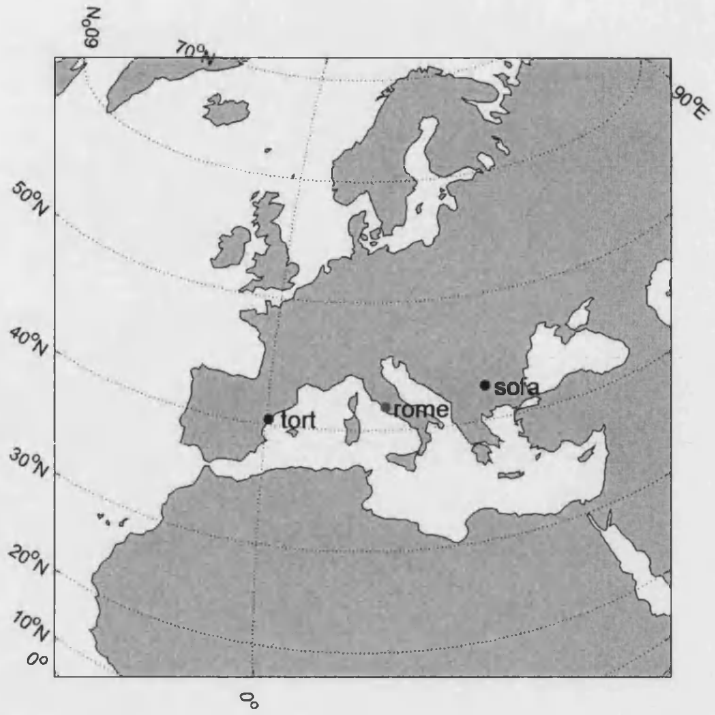

Figure 4.14. Locations of selected European ionosondes.

These data were converted into an electron density value using the formula below, which states that the square of the critical frequency in MHz, f, is directly proportional to the maximum electron density of that layer, N_E, measured in electrons per m^3. Further details can be found in McNamara (1991) and Davies (1990).

$$N_E = \frac{f^2}{80.5} \qquad [4.2]$$

The ionosonde peak electron density was compared to the corresponding images by taking the peak electron density from the vertical set of voxels closest to the location of each of the ionosonde from the REAL data set, given in Table 4.1. Figure 4. show the peak density values for the ionosondes and from the MIDAS inversions at these locations during the April 2002 geomagnetic disturbances.

Table 4.1. **Geographic locations of ionosondes and nearest MIDAS inversion voxel.**

Receiver	Geographic		Voxel	
	Latitude	Longitude	Latitude	Longitude
Tortosa	40.8°N	0.3°E	41°N	2°E
Rome	41.8°N	12.5°E	42°N	14°E
Sofia	42.4°N	23.2°E	42°N	22°E

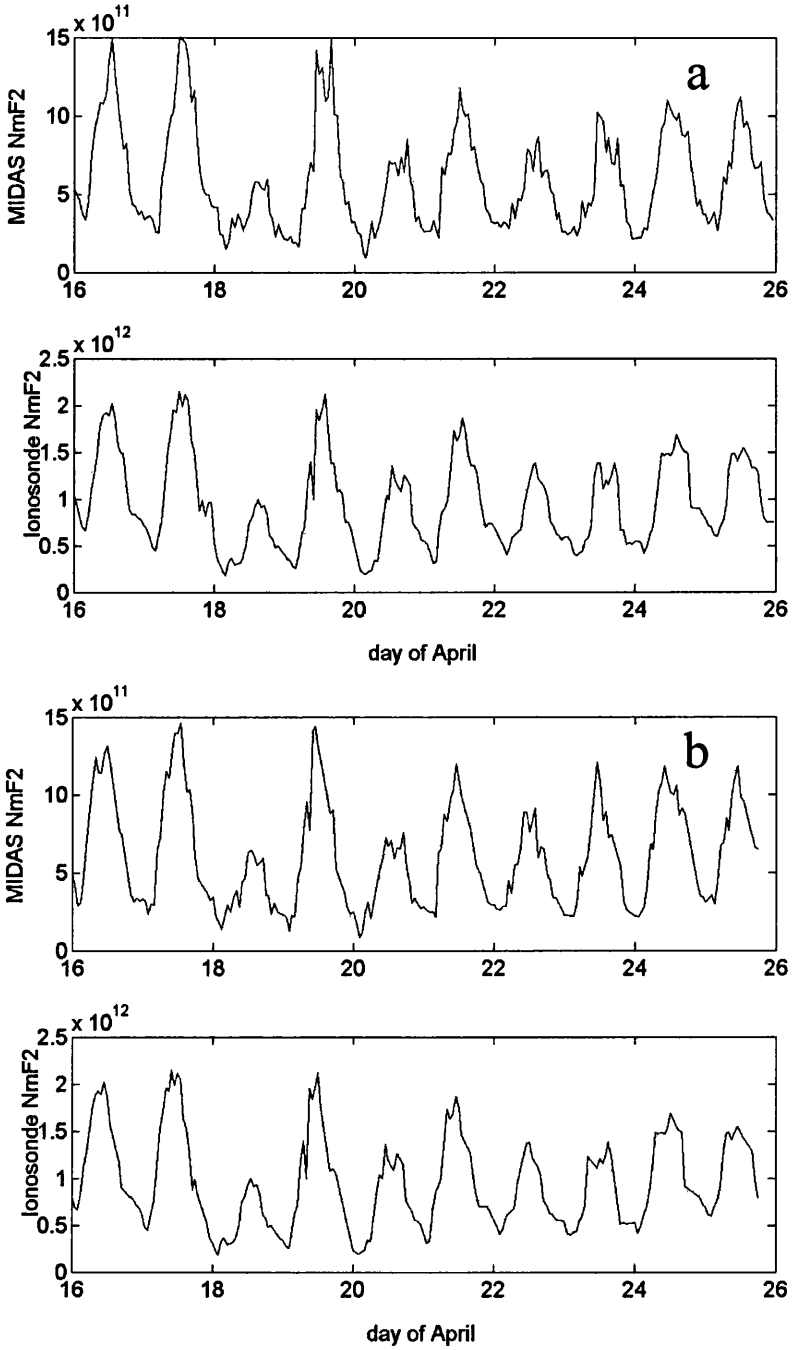

Figure 4.15. **Graphs showing the peak electron densities from the F-layer extracted from the MIDAS inversions and from the ionograms of Tortosa (a), Rome (b) and Sofia (c).**

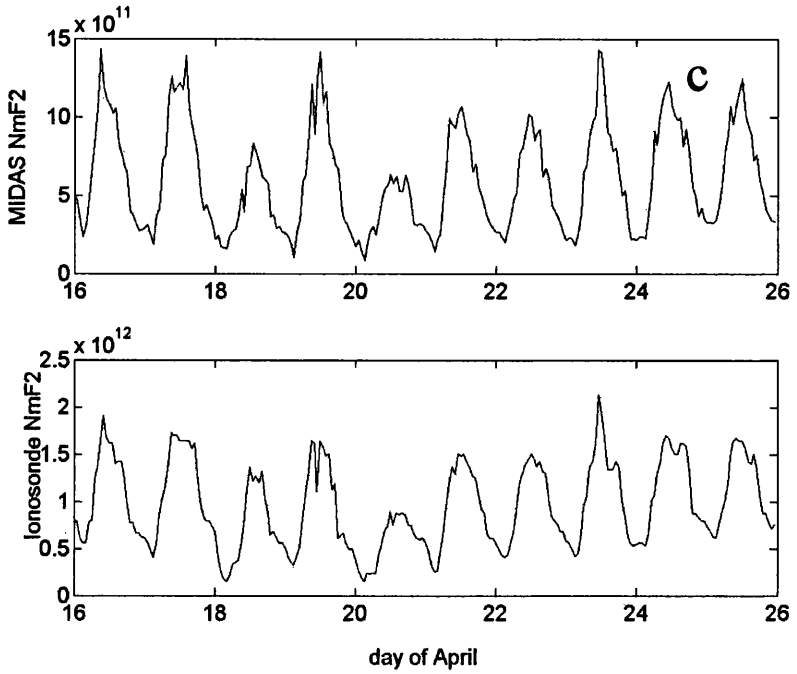

Figure 4.15 Graphs showing the peak electron densities from the F-layer extracted from the MIDAS inversions and from the ionograms of Tortosa (a), Rome (b) and Sofia (c).

The correlation coefficients for the peak EDs are high. The correlations were Tortosa (+94.53%), Rome (+92.27%) and Sofia (+95.85%). However, there is systematic underestimate of the peak electron density of 30% for all comparisons. This can be seen in Figure 4.16, which shows direct comparisons between measurements from the three ionosondes and from the MIDAS inversions. At all three locations, the majority of points are below the perfect correlation line.

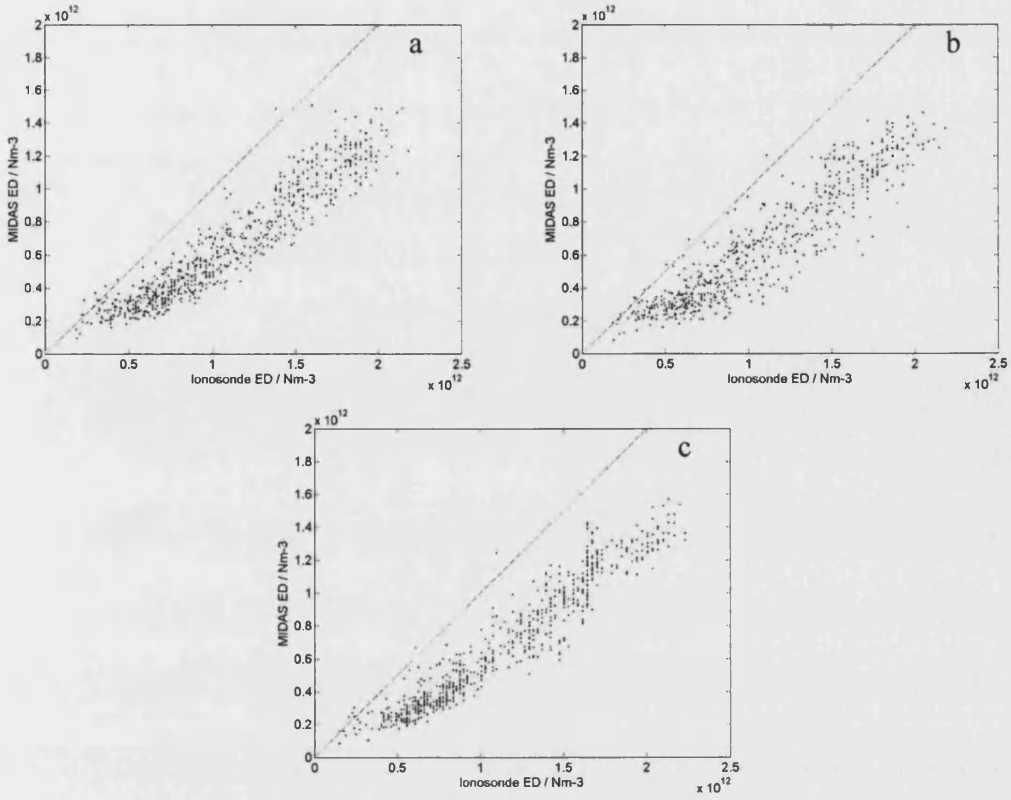

Figure 4.16. Comparison between peak electron densities for ionosondes and MIDAS inversions for Tortosa (a), Rome (b) and Sofia (c).

The gradient of the linear least-mean-square fits are 0.67, 0.67 and 0.72. Underestimates are greater than in the simulation study but are present in both simulation and actual data studies. This suggests that it could be due to the conditioning of the imaging algorithm. The vertical domain is defined in MIDAS using models to form a basis set of electron-density profiles. This requirement for vertical profile information is a well established issue due to the limited viewing angle of the satellite to ground data, inherent in tomographic imaging (Yeh and Raymund, 1991). The vertical profiles basis set models used so far, do not distribute the electron density correctly. In order to form a better basis set, **X** in Equation 2.16, a method to create them from ionosonde data has been implemented and is shown in the next section.

4.5 Formation of EOFs using GPS and ionosonde data

A modification to the inversion procedure was implemented. This new technique used contemporaneous measurements of the height and electron density at the F2 layer to produce a more realistic basis set of Chapman profiles to form the EOFs. This approach has been developed by Materassi and Mitchell (2005). Here, two ionosondes, Tortosa and Sofia, are used together with actual GPS phase measurements to reconstruct the vertical electron density profile

of the ionosphere. The inversion parameters used were as in Table 2.1, but the F2-peak height was obtained from the two ionograms, along with a range of bottom-side scale heights, {40, 60, 80, 100, 120} km, to replace the generalised set of F-layer characteristics. The accuracy of the new approach is verified using the Rome ionosonde as an independent source of data. The locations of the used and independent test ionosondes are shown in Figure 4.14.

A direct comparison of the peak electron density results, which used GPS alone and including the ionosonde data, is shown in Figure 4.17. The comparison for the GPS differential phase data is shown in the upper plot and the GPS data using the ionosonde method is shown in the lower plot. A dashed line showing an ideal correlation is included in both plots.

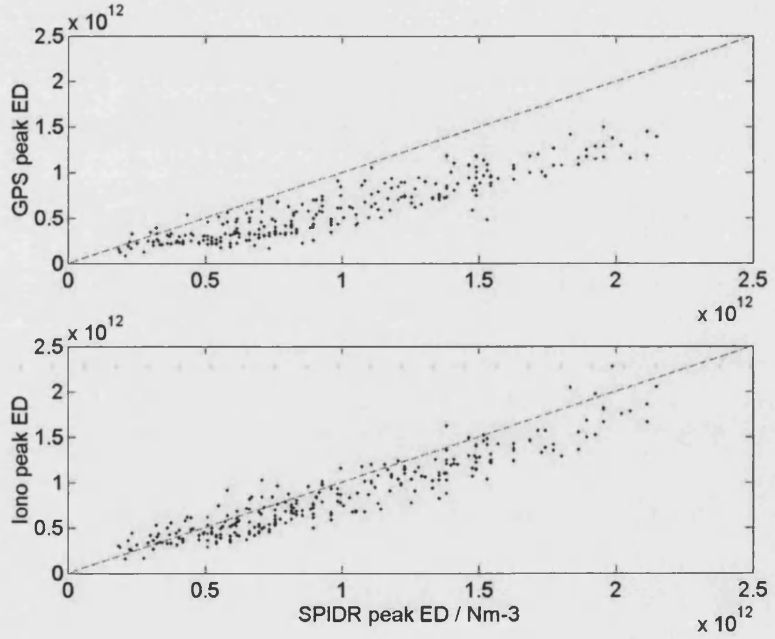

Figure 4.17. Direct comparisons of methods with the Rome peak electron density. The upper graph shows results using generic EOFs and the lower one, the "tailored" EOFs.

It can be seen that the lower graph is an improved match to the 1:1 correlation line. The correlation has remained high, 90.7% and the new method using peak electron density from other ionosondes has improved matters, especially for larger measurements of peak electron density. The gradient of the least mean square fits with and without the ionosonde data are 0.80 and 0.65 respectively, showing a significant improvement has been produced by including the ionosonde data.

A final test was carried out to verify that the improved MIDAS technique does not adversely affect the TEC accuracy. This requires a return to the simulation study because there is no

independent method to measure TEC. In Figure 4.18, the mean hourly TEC for the MIDAS reconstructions are compared with (dashed line) and without (solid line) the updated vertical profile. The results are very similar and have a mean, absolute mean and rms difference of 0.66, 1.08, 1.40 TEC units. This shows that the improvements made to the distributions in electron density have little effect on the final TEC result as it remained unbiased.

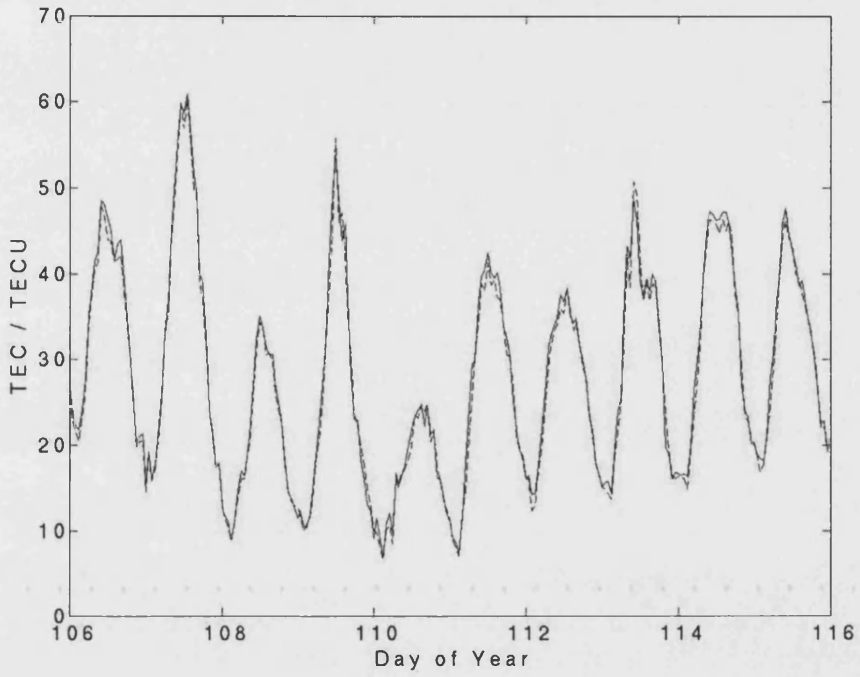

Figure 4.18. Mean hourly TEC for MIDAS with and without calibration.

The use of a confined set of basis functions, assisted by ionosonde data, improves the peak electron density, but does not effect the overall TEC measurement. This is because the method only redistributes the electron concentrations vertically in a more appropriate manner and has minimal effect on the integrated result. Therefore, the inclusion of the ionosonde data should be used when a more detailed vertical profile is required, but is not required for the vertical TEC.

4.6 Conclusions

A simulation study was carried out using the empirical model IRI for the year of 2002. The results of the study show that MIDAS can reconstruct the mean vertical TEC to rms, mean and absolute mean accuracies of 1.0, 0.2 and 0.7 TEC units respectively. The second conclusion of this study was that MIDAS consistently underestimates peak electron density. This underestimate was seen to be 15% in the simulated study and was found to be due to the

inversion's vertical structure being badly distributed due to an inappropriate choice of vertical basis functions, which are defined by the user. EOFs are used because GPS data alone are poor at measuring the vertical structure, as the inversion is underdetermined. A limited number of basis sets constrain the result so that an appropriate vertical ionospheric, electron-density profile can be produced. However, the vertical profiles in the bias set are not defined with relation to geophysical conditions or location, and hence inappropriate choices can be made by this use of a generic set of Chapman profiles.

For the experimental study, peak electron density values from MIDAS were compared to corresponding ionosonde measurements of the peak electron density values across Europe. The three sites had high correlations, between +92% and +96%, but also had underestimated the peak densities by over 30%. This again is attributed to an inappropriate definition of vertical basis functions.

The correlation between MIDAS and the ionosonde peak electron density was improved by including selected current ionosonde measurements into the imaging method. This is because the additional information gives real-time information about the actual vertical profiles, at least on the bottom-side. The TEC values were not affected, which indicates that only a redistribution of electron density occurred. The TEC measurements for both methods are accurate and can be used for further analysis.

Chapter 5 GPS interfrequency biases and total electron content errors in ionospheric imaging over Europe

5.1 Introduction

In the previous chapter, the accuracy of the MIDAS inversions was tested using a model ionosphere. Here a method that adds the Inter-Frequency Biases (IFBs) for each GPS satellite and receiver pair is used to verify further the accuracy of the imaging. First, the method is tested in a simulation study in which the IFBs from CODE, and the ionosphere simulated using the IRI-95, are combined and used as the input to MIDAS. This allows the errors in the IFB determination, and therefore the error in the TEC, to be found and give an indication of the expected errors in the real imaging system. Secondly, the procedure is repeated using real data, and the IFBs determined from ionospheric imaging are compared with those from CODE. Again, the errors are assessed by differences between the CODE-determined IFBs and the imaging IFBs. Results reveal that changes in the biases can be related directly to documented changes in receiver hardware, and allow an indication of the receiver biases and the error in TEC estimation for the images that MIDAS produces.

Dual frequency GPS data can be used for ionospheric investigation because the ionosphere is a dispersive medium causing a phase advance and a group delay to radio signals. If both frequencies are monitored simultaneously, then the data can be used in two different ways to obtain information about the TEC between any satellite and receiver. First, the difference between the signal phases yields the change in slant TEC, provided that the receiver does not lose lock on either signal. Second, the codes on the two signals can be used to find the difference in propagation speeds of the two signals and hence the slant TEC. Although this method at first might appear to provide absolute TEC, it suffers from errors due to the IFBs. These occur because of the unknown differences in time for the two signals to propagate through the satellite and receiver hardware, hence they are classified as either satellite interfrequency biases or receiver interfrequency biases. Frequently these IFBs are determined in pairs, such that each satellite plus receiver IFB constitutes the difference between an apparent and the actual ionospheric delay, and hence forms most of the error in TEC determination.

The topic of IFB determination has previously been addressed by Mannucci et al. (1998), Coco et al. (1991) and Sardon and Zarraoa (1997). The reason to revisit it here in the context of ionospheric imaging is that the magnitudes of these biases and the accuracy to which they can

be determined is very important for ionospheric measurement and imaging, since they are a source of error for ionospheric measurements based upon differential code records. One manner in which the accuracy of ionospheric imaging can be assessed is by the evaluation of the IFB values.

5.2 Simulating GPS data with interfrequency biases

In the first stage, a simulation study was undertaken. In order to simulate dual frequency GPS observations it is necessary to model the ionospheric delay and the transmitter and receiver IFBs. To make these realistic the IRI-95 model (Bilitza, 1997), was used to calculate the satellite-to-receiver differential delay and the biases were modelled using those calculated by CODE (http://www.aiub.unibe.ch/). The interfrequency biases used in this and further simulation studies are given in Section 5.3, Table 5.1 and Table 5.2. There are several sources of receiver and satellite interfrequency biases but CODE was chosen as a good indication of the correct bias values and has been tested alongside the GPS broadcasted group delay. Bias values are downloadable from October 1997 to the present and should continue as various biases are recommended for use with IGS official products (Ray, 2001).

CODE produces global ionospheric maps every two hours using over 200 GPS and GLONASS receiver sites from the IGS network and other institutions. The biases are calculated as a daily constant and are calculated alongside the 3328 parameters that are used to represent the global vertical TEC distribution. The daily repeatability of the biases is good with an rms error of approximately 0.03 and 0.20 nanoseconds for the GPS and GLONASS constellation (Schunk et al., 2002). The biases are given in time delay, which must be converted to TEC units before adding to the simulated ray paths. Equation 5.1 gives the relationship between ionospheric group delay to signal frequency and TEC. The signal frequency is the difference between the two GPS signal frequencies and so this produces the following relationship, with the reverse of this is given in Equation 5.2.

$$bias(ns) = 0.3469 * bias(TECu) \quad [5.1]$$

or

$$bias(TECu) = 2.8827 * bias(ns) \quad [5.2]$$

A particular day was selected, 15th February 2002, and the satellites' positions were obtained from the database provided by the International GPS Service (SOPAC). Since these were provided at 15-minute intervals they were interpolated linearly to 30-second intervals.

Numerical integration between each satellite position and each receiver in view of that satellite allowed the calculation of slant TEC (b) between a specific satellite and receiver (b_{sr}). In Equation 5.3, A is a vector that contains measurements of the path length though each voxel and IRI_{Ne} the electron density in each voxel given by the IRI model.

$$b_{sr} = \sum_{1}^{M} [A(IRI_{Ne})] + IFB_S + IFB_R \qquad [5.3]$$

Hence, if a particular ray path crosses M voxels, then each simulated measurement is the TEC through the IRI model plus the interfrequency biases. Satellite and receiver IFB values generated by CODE (IFB_S and IFB_R) were added to each simulated IRI TEC, and then grouped into periods of one hour. The inversion of the relative differential phase changes (or changes in TEC) was performed using the MIDAS algorithm described in Section 2.4.

The inversion results in a four-dimensional image showing the distribution of electron concentration. Static images of TEC are produced by summing the vertical columns of voxels in the image half way through the movie period. In experimental studies the GPS phase data from the database provided by the International GPS Service is used as input instead. The differences between the differential code measurements (i.e. those with interfrequency biases) and the corresponding MIDAS slant TECs are found. These differences are attributed to the combined satellite and receiver IFB values. Thus for each satellite and receiver pair a single bias value is found. The individual receiver and satellite interfrequency biases were estimated by a least-squares-fit.

5.3 Simulation results

Examples of the input data used in the simulation are shown in Figures 5.1 to 5.5. Figure 5.1 shows the vertical TEC taken from the 3D electron concentrations in the IRI model. Figure 5.2 shows the locations of the GPS receivers used in the simulation. They are a selection of the actual receiver sites of the geodetic GPS receivers in Europe. Figure 5.3 gives an idea of the data coverage by showing the equivalent vertical TEC at 400 km altitude between each GPS satellite and receiver. This is found by performing a geometrical correction of the slant TEC through the IRI model, without IFBs added. Continuous satellite-to-receiver arcs are clearly seen. It is these adjacent measurement along continuous satellite-to-receiver pairs that the algorithm relies on by computing the differences between adjacent measurements of the input data. Figure 5.4 shows the same as Figure 5.3, except the IFBs have been added to the slant TEC values. It should be noted that the IFBs are of no consequence to the imaging algorithm

itself because they are negated by the ray differencing technique. They are calculated using the differences in slant delay through the final image and the original differential delays.

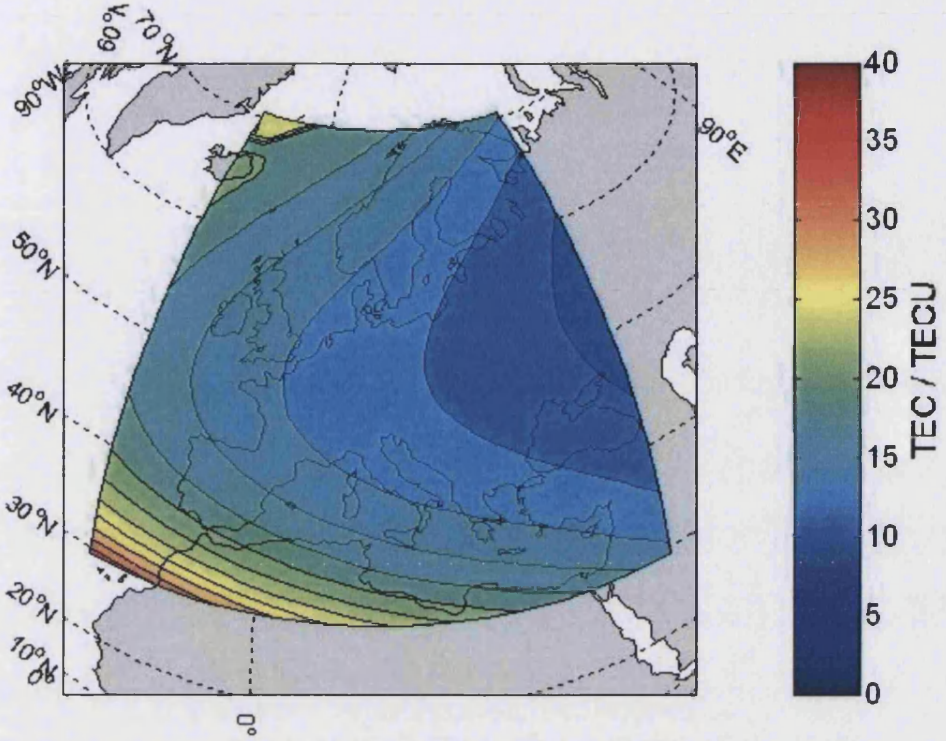

Figure 5.1. Vertical TEC over the European region from the IRI model at 00:30 UT on 15th February 2002.

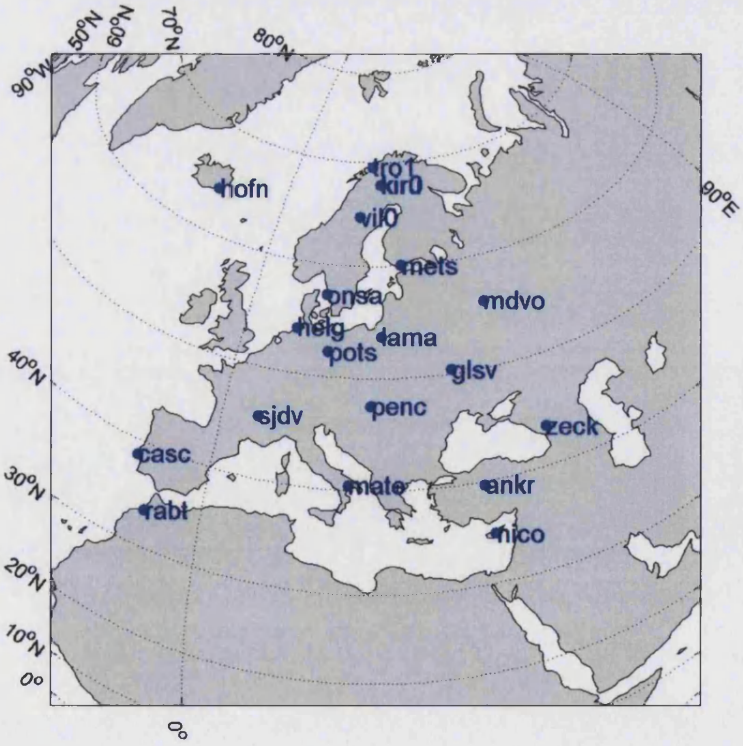

Figure 5.2. Locations and site codes of the GPS receivers used in the simulation.

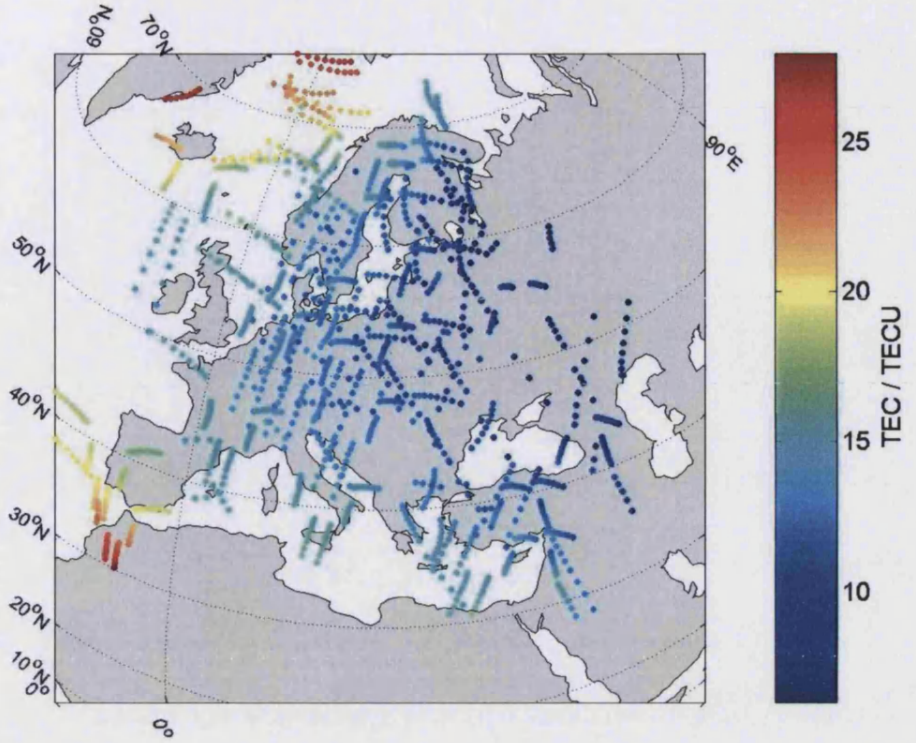

Figure 5.3. TEC calculated by integration between satellite and receiver through the IRI model for the hour following 00:00 UT on 15th February 2002. Each point shows the intersection of a ray path with a shell at 400 km approximated to vertical TEC at that point.

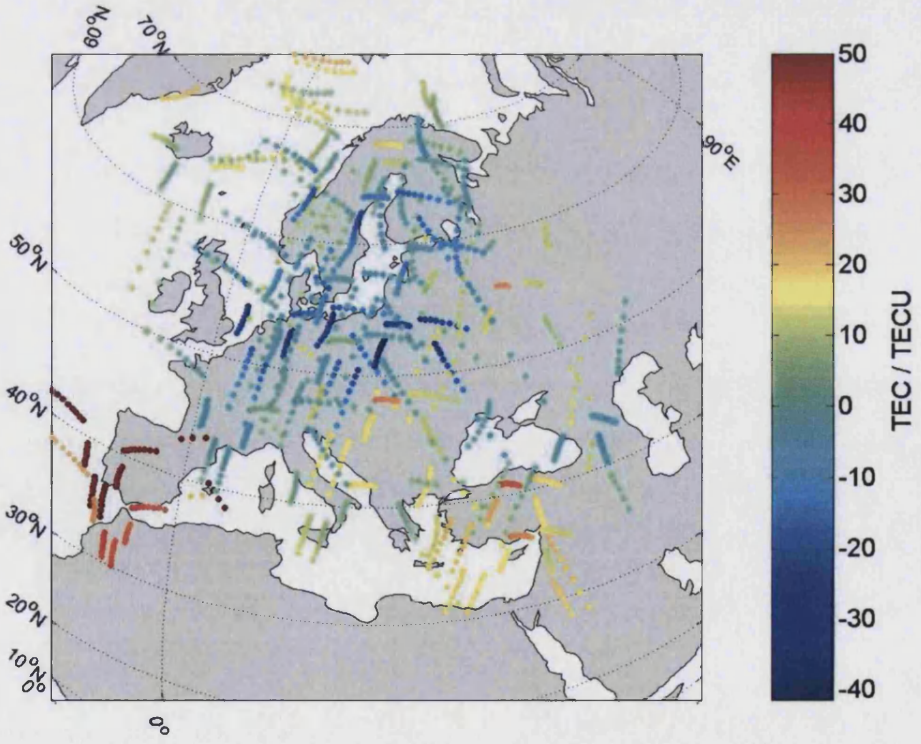

Figure 5.4. Simulated TEC of Figure 6.3 with CODE IFB values added for the hour following 00:00 UT on 15th February 2002.

Figure 5.5 shows the vertical TEC through the ionospheric image reconstructed from the data of Figure 5.4. By visual comparison with Figure 5.1 it can be seen that the vertical TEC in the ionosphere is well reproduced with mean absolute error in vertical TEC of 0.4 TEC units overall.

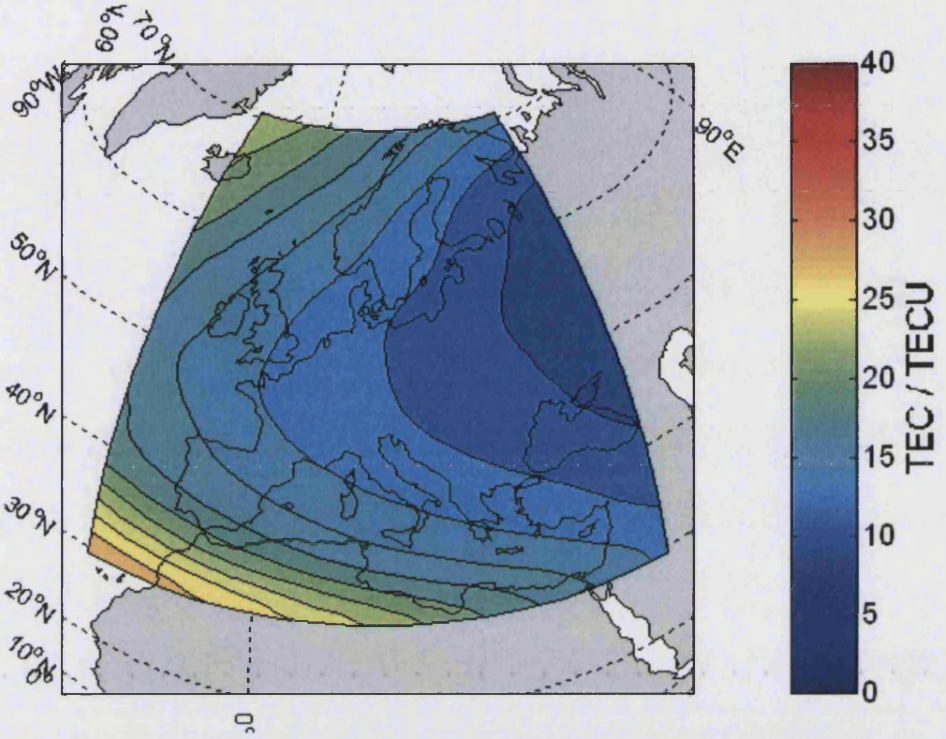

Figure 5.5. Vertical TEC produced by the inversion at 00:30 UT on 15th February 2002.

Figure 5.6 shows the receiver plus satellite IFBs from CODE (i.e. the true values put into the simulation) plotted against the biases obtained from the MIDAS inversion. Each point on the graph is the combination of a satellite plus receiver IFB calculated hourly by MIDAS, and plotted against the corresponding 30-day mean value from CODE. All pairs of receiver and satellite interfrequency bias are plotted when a satellite is in view of a receiver for a full hour. Good correlation can be observed between the biases that were put in to the simulation and those calculated by the MIDAS algorithm. This demonstrates that MIDAS can be used to calculate the paired IFB values. The correlation coefficient is +99.7% and the rms, mean and absolute errors are 0.92 ns, 0.29 ns and 0.64 ns. The respective slant TEC errors in TEC units, were 2.64, 0.83 and 1.84, and the percentage slant TEC errors were 6.0%, 0.7% and 4.4%. The vertical TEC errors are 1.28, 0.40 and 0.91 TEC units and in percentages 4.5%, 0.4% and 3.4%. Hence, for the simulation there is a very small (less than 1%) underestimate in TEC.

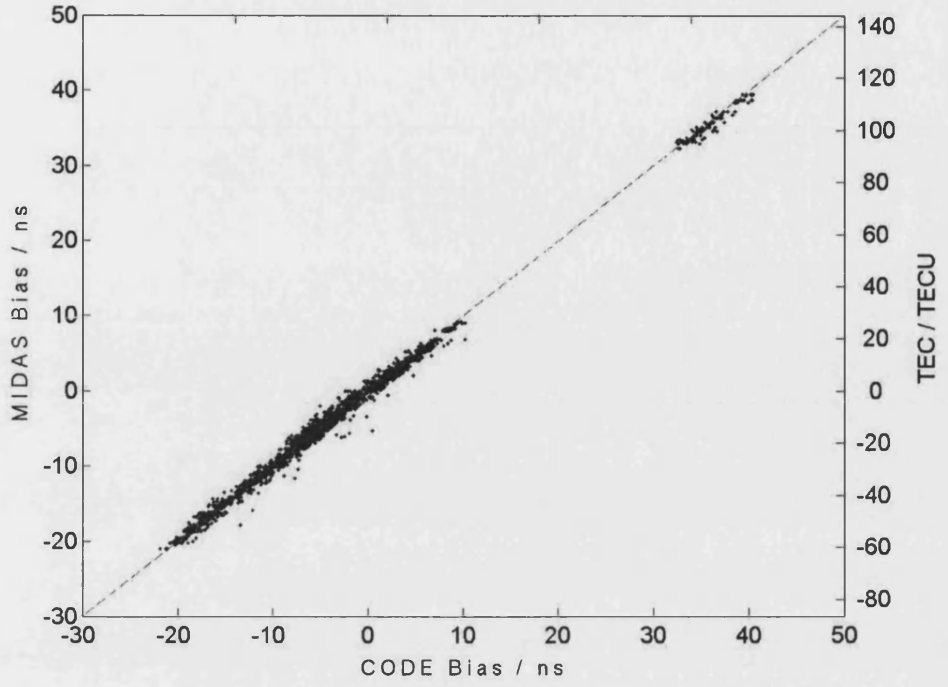

Figure 5.6. Simulated interfrequency bias comparison for 15th February 2002. Units are in both nanoseconds and TEC units ($1x10^{16}$ e m^{-2}).

Further simulation studies were also completed to verify that MIDAS was fitting to the actual magnitude of biases and not just replicating the least-mean-square distribution of the biases produced by the CODE algorithms. Firstly, the CODE biases were added to a simulated ionosphere as before but an extra 10 nanoseconds was added to each receiver and satellite bias, given in Table 4.1 and Table 5.2. Therefore, the output interfrequency bias of each satellite-receiver ray path should increase by 20 nanoseconds. If MIDAS fitted to the distribution of the interfrequency biases, the biases output would remain the same as before and so the TEC would be inaccurate by 10 nanoseconds or approximately 29 TEC units. This approach was used with the February 15th data. Figure 5.7 shows the satellite plus receiver biases output by MIDAS against the input satellite plus receiver biases. The correlation was +99.7%, which is identical to the study in which the CODE biases were not altered, but biases can now be seen to be in the range 0 to 60 nanoseconds, instead of -20 to 40 nanoseconds. This is the 20 nanosecond change of the interfrequency biases expected.

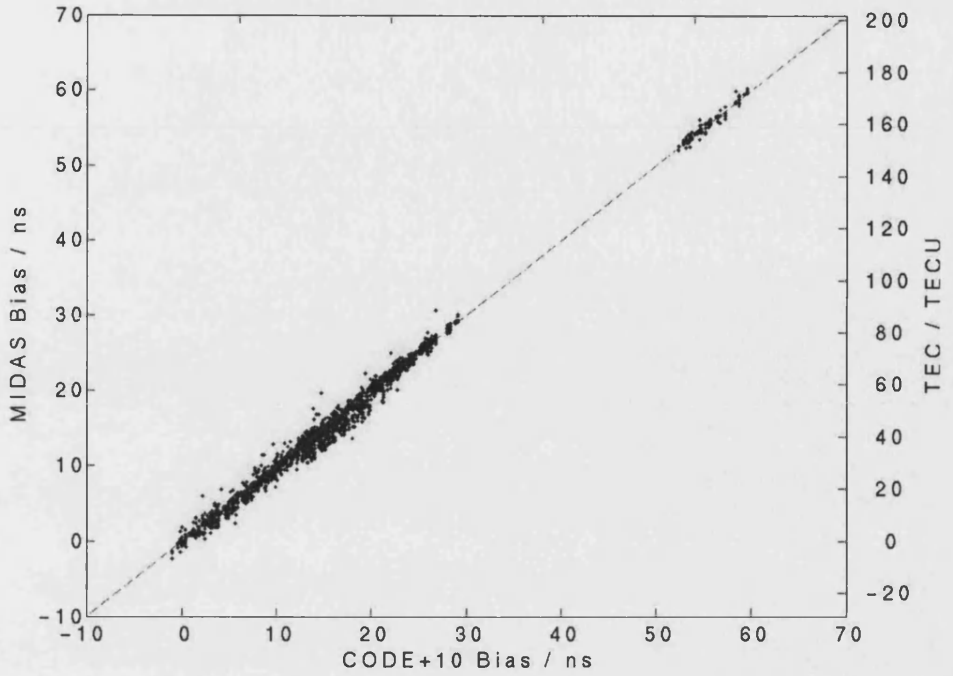

Figure 5.7. Simulated biases from CODE with 10 ns added and satellite ray paths from 15th February 2002.

A third simulation study has also verified the distribution of the biases by applying an integer bias to each receiver and satellite. This produced a distribution of the biases that are not correlated with the original CODE biases. The receiver bias was based on the alphabetical order of the receivers and the satellite bias from the satellite identification number, the satellite PRN. The values used are given in Table 5.1 and Table 5.2. The satellite data from February 15th 2002 was used and Figure 5.8 shows the comparison of the biases output by MIDAS and those input by this method.

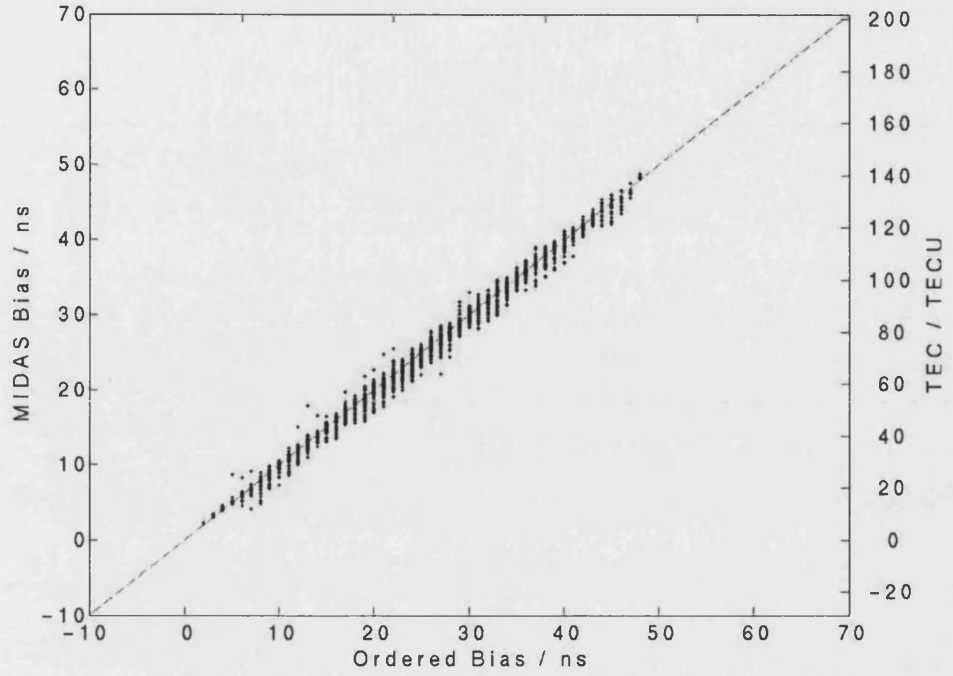

Figure 5.8. Simulated biases using PRNs and ordered receiver numbers with satellite ray paths from 15th February 2002.

The correlation found was again high, +99.6%. The results from these simulation studies show that interfrequency biases are correctly calculated by MIDAS and therefore that the integrated electron concentration information of satellite to receiver ray paths remaining after the bias has been removed is of high accuracy.

The receiver and satellite biases used in the three simulation studies are given in Table 5.1 and Table 5.2.

Table 5.1. **Receiver IFBs used in simulated studies.**

Site code	CODE bias (ns)	CODE+10 (ns)	Ordered (ns)
ankr	5.011	15.011	1
casc	35.403	45.403	2
glsv	-11.028	-1.028	3
helg	-16.437	-6.437	4
hofn	-4.195	5.805	5
kir0	-4.723	5.277	6
kiru	-0.083	9.917	7
lama	-17.885	-7.885	8
mate	-2.802	7.198	9
mdvo	2.678	12.678	10
mets	-10.211	-0.211	11
nico	2.226	12.226	12
onsa	-9.590	0.410	13
penc	2.568	12.568	14
pots	-6.473	3.527	15
rabt	4.957	14.957	16
sjdv	-7.805	2.195	17
tro1	-2.070	7.930	18
vil0	-14.469	-4.469	19
zeck	-5.394	4.606	20

Table 5.2. **Satellite IFBs used in simulated studies.**

Sat. PRN	CODE bias (ns)	CODE+10 (ns)	Ordered (ns)
01	-1.358	8.642	1
02	-2.527	7.473	2
03	-0.649	9.351	3
04	0.125	10.125	4
05	-0.645	9.355	5
06	-0.270	9.730	6
07	-2.307	7.693	7
08	-1.062	8.938	8
09	0.095	10.095	9
10	-2.251	7.749	10
11	4.109	14.109	11
13	3.802	13.802	13
14	3.316	13.316	14
15	-1.730	8.270	15
17	-1.917	8.083	17
18	3.253	13.253	18
20	0.866	10.866	20
21	-2.085	7.915	21
22	-0.825	9.175	22
23	-1.747	8.253	23
24	-3.085	6.915	24
25	1.330	11.330	25
26	0.300	10.300	26
27	-0.881	9.119	27
28	2.980	12.980	28
29	1.056	11.056	29
30	1.791	11.791	30
31	0.315	10.315	31

5.4 Experimental results

Using the receiver configuration of Figure 5.1, the MIDAS algorithm was used to reconstruct ionosphere images for each hour of the year 2002. Firstly, a small section of this data was used to verify the accuracy of the hourly IFBs from MIDAS for direct comparison to the simulation results. The day 15th February 2002 was again used and Figure 5.9 shows the receiver plus satellite IFBs obtained from the MIDAS inversion, plotted against those obtained by CODE, where only the IFBs which occur in both sources are used for the comparisons. Good agreement in the IFB values from MIDAS and CODE was found with a correlation coefficient of +98.6%, and rms, mean and absolute differences of 2.00, 0.36 and 1.57 nanoseconds. These correlations were lower than they had been in the simulation.

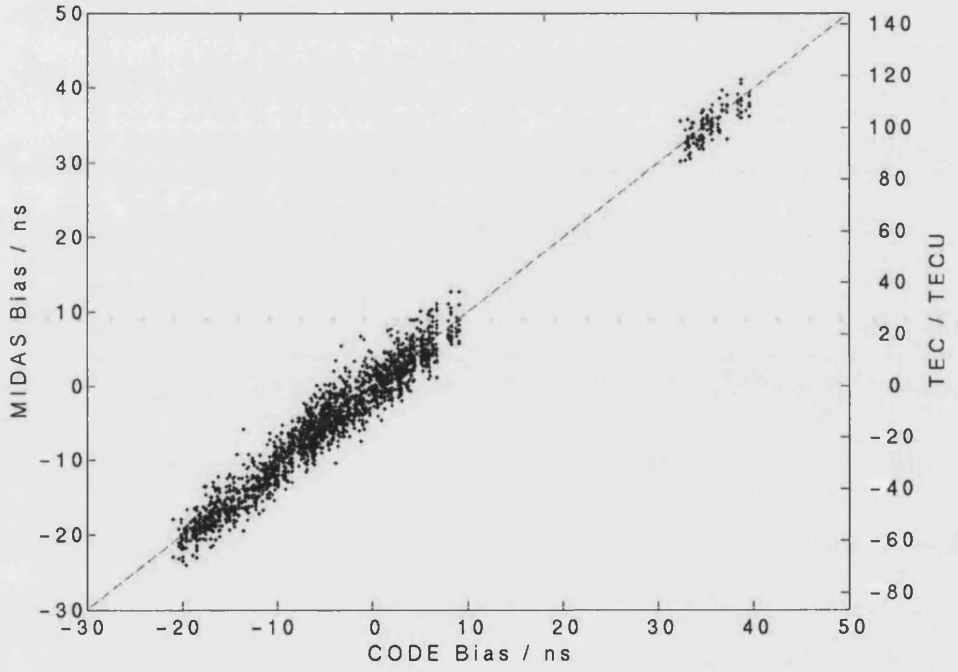

Figure 5.9. Experimental interfrequency bias comparison for 15th February 2002. Units are in both nanoseconds and TEC units ($1x10^{16}$ e m^{-2}).

Secondly, 30-day averages of the interfrequency bias, for each satellite-receiver pair were calculated and compared to those from CODE. Figure 5.10 shows these results. In general, a good agreement is found with a correlation coefficient of +98.3%, and a rms, mean and absolute difference of 2.03, -0.54 and 1.22 nanoseconds. It is interesting to note in the figure a cluster of points where there is disagreement and these were looked at in more detail. Disregarding this cluster, the statistics are improved by a small amount, with a correlation coefficient of +98.9%, and an rms, mean and absolute error of 1.64, -0.47 and 1.16 nanoseconds.

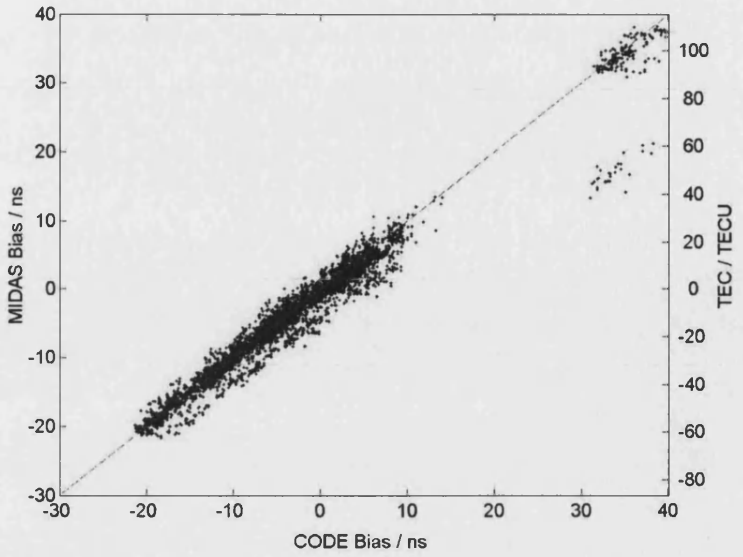

Figure 5.10. Comparison of monthly mean receiver and satellite combined interfrequency bias for MIDAS and CODE.

This cluster of mismatched IFB values was found to be associated with a receiver based in Cascais, Lisbon, Portugal. On July 10th 2002, (191st day of year) between 15:30 UT and 16:00 UT, the receiver's hardware was updated. This was documented on the site log (ftp://garner.ucsd.edu/pub/docs/site_logs/casc.log.txt). It seems that the update to the hardware caused the IFB related to this receiver to alter dramatically. A series of estimates of this receiver bias can be seen in Figure 5.11 for the year 2002. In this case, the absolute values of the biases are not determined reliably, since the individual satellite or receiver biases cannot be found independently, but the relative change is clear. Figure 5.12 shows the same plot over the five days around the change in the hardware. The change of interfrequency bias over day 191 is approximately 23 nanoseconds, which is equivalent to 66.2 TEC units. The plots demonstrate that the imaging technique is able to separate out changes in individual IFB values and can detect their changes on hourly timescales. However, it should be stressed that individual satellite or receiver IFBs such as these are not uniquely determined by our technique, unlike combinations of satellite and receiver IFBs which can in theory be found.

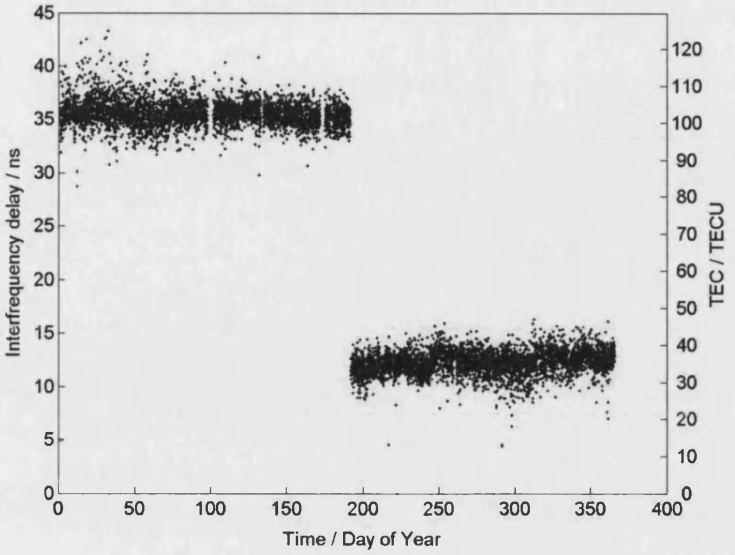

Figure 5.11. **Cascais receiver interfrequency bias for 2002.**

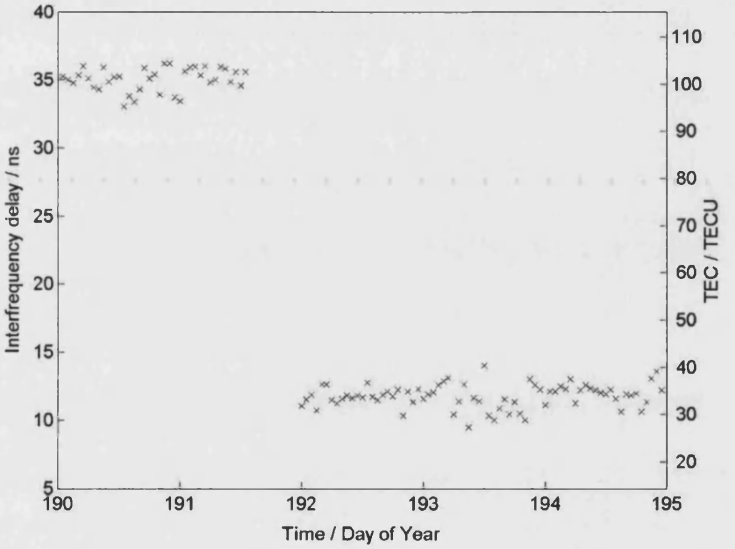

Figure 5.12. **Cascais receiver interfrequency bias around the time of the change in hardware.**

5.5 Conclusions

A simulation study was carried out using a realistic representation of the ionosphere from the empirical model IRI. Satellite and receiver IFB values were simulated using values calculated by CODE. The results of the study showed that the MIDAS ionospheric imaging technique can be used to calculate IFBs values to an accuracy of rms, mean and absolute mean values of 0.92, 0.29 and 0.64 nanoseconds. The corresponding slant TEC errors found by differencing those through the image with those from the IRI model were 2.64, 0.83 and 1.84 TEC units. In

percentage terms these values were 6.0%, 0.7% and 4.4%. Vertical TEC errors were 1.23, 0.40 and 0.92 TEC units and 4.5%, 0.4% and 3.4% respectively.

The experimental study for the same day showed that differences between the hourly MIDAS IFBs and the long-term CODE values were rms, mean and absolute mean values of 2.01, 0.35 and 1.60 nanoseconds. These indicate that the errors found by experiment are approximately double those found by simulation, assuming that the CODE bias values are correct.

On a longer timescale of one year the statistics of the differences between the monthly mean IFBs from MIDAS images and the CODE values were rms, mean and absolute mean values of 1.64, 0.47 and 1.16 nanoseconds. The MIDAS IFB values clearly showed the change in the bias for the Cascais receiver, which was traced to a documented change in the hardware at that site. It is noticeable that the errors are larger in the experimental case when compared to the simulation. Likely causes are changes in the IFB value with multipath. The data here were all processed with a 10° elevation mask but this may not be adequate in all cases.

The results are of interest for several reasons. Firstly, they give an estimate of the errors involved in TEC determination through the type of ionospheric imaging that relies on using uncalibrated differential phase observations. This gives confidence in the determination of absolute TEC values, which is important for the subsequent use of ionospheric images. This could be for scientific use where bounds on the physical parameters of the ionosphere are sought (see for example Yin et al., 2004). The results are also applicable to the navigation community who are interested in accuracies in TEC mapping for ionospheric corrections by Satellite Based Augmentation Systems such as WAAS and EGNOS. Finally, for real-time ionospheric mapping the ability to calculate IFBs on an hourly basis is very useful in situations where the values may change, such as in the case of the Cascais receiver. Data from new hardware can be used without concerns over the site-specific IFB values. The use of pre-calculated IFBs for this receiver in an ionospheric imaging/mapping system would have resulted in the introduction of errors of 66 TEC units for all slant paths from that site and this could have created an artificial ionospheric feature in the maps. The use of uncalibrated differential phase data for ionospheric mapping avoids this potential problem.

Chapter 6 Analysis of TEC forecasting techniques for a single location and wide-area maps

6.1 Introduction

In the previous two chapters the accuracy of imaging the ionosphere has been addressed. This chapter is concerned with forecasting the ionospheric electron density over timescales of several hours. The problem of forecasting has two sub-areas; in the first instance the issue is dealing with changes in the magnitude of the electron density. In the second (covered in Chapter 7) the complication of feature recognition is included. In this chapter, several methods of time-series forecasting are tested and developed into forecasting of wide-area maps. The techniques are tested and refined on data for the year 2002 that includes both quiet and disturbed geomagnetic conditions.

A review of the various modelling and forecasting approaches can be found in Chapter 3. Here, we focus on the development of time-series forecasts into forecasts of wide-area maps. The MIDAS algorithm is used to produce movies of electron density, and then integration provides maps of vertical TEC. Initially, various algorithms are used to implement single site forecasting of TEC for periods up to 12 hours. The methods used range in complexity from basic methods, such as persistence, to algorithms that use a database of past absolute and differentiated TEC measurements to match current data. These matching algorithms produce a significant improvement to long-term prediction methods, such as the IRI model. The accuracy of these methods are shown using TEC data from a period of high ionospheric variability, the April 2002, geomagnetic storm. These methods are then extended to produce wide-area forecasts over the European region for periods of 1 to 6 hours ahead. A forecasting method using percentage gradients calculated using the IRI-95 model is described and analysed. The accuracy of this method is shown for the year 2002 and it is shown to be useful for forecasting during certain solar conditions. An improvement in forecasting accuracy can be produced by using methods according to recent geomagnetic activity.

6.2 Forecasting methods

In this section a brief explanation of each forecasting approach is given, followed by the main formulae used in each method. I_T is the measured or predicted TEC at a particular time, T, in

hours. The time is indicated with three separate variables relating to the current time and period from this time. These variables are the current time, t, and two other variables, τ and n, which indicate the forecast period in hours and the number of days from the end of the TEC measurement.

N and W are used to describe the size of window used for some methods. N indicates the number of days the window covers and W is the number of past measurements used to match from of a particular day, so for example a forecast which uses W=4 and N=3, would match the last four TEC measurements from the current day with the three previous days.

6.2.1 Persistence

The most basic forecasting technique is persistence, which takes the TEC from the most recent TEC measurement and uses this as the forecast. This is used as a basic test of the forecasting technique's accuracy and is described below in Equation 6.1.

$$I_{t+\tau} = I_t \qquad [6.1]$$

6.2.2 24-hour Persistence

The accuracy of basic persistence should decrease as the forecast period increases because the TEC measurements are less relevant to the current time. Contrary to this, the measurement from the previous day, or 24-hour persistence, may be useful as it has the same local time. This method will not perform well in cases of large day-to-day variations which may occur during high geomagnetic periods. The method is described in Equation 6.2.

$$I_{t+\tau} = I_{t+\tau-24} \qquad [6.2]$$

6.2.3 Average percentage gradient

A more complicated method was developed that uses the most recent TEC measurement, but then uses several recent TEC changes to forecast the amount that TEC would change. The change in TEC is produced by calculation of the average percentage changes from the relevant

times during the most recent days. The percentage gradient (P_g) was used and the forecast period for the last N days found and applied to the most recent image to produce the forecast. For this study, N=3 is used as this gave the most accurate result. This technique can be described using Equations 6.3 and 6.4.

$$I_{t+\tau} = I_t * \sum_{n=1}^{N} \frac{P_g(t,n)}{N} \qquad [6.3]$$

where the percentage gradient over a forecast period, τ, from time t, using the TEC from n days in the past can be written as:

$$P_g(t,n) = 1 + \frac{I_{t+\tau-24n} - I_{t-24n}}{I_{t-24n}} \qquad [6.4]$$

6.2.4 IRI model

The IRI model (Bilitza 1990) is a well-established ionospheric model and has been used for many different applications. The IRI-95 version (Bilitza, 1990) uses 12-month running averages of solar and magnetic (Rz12) indices, along with seasonal variation and other ionospheric coefficients to generate the vertical and horizontal variations of the electron concentration in the global ionosphere. The model was evaluated for every hour of the forecast period and will generate a good estimate of a monthly median forecast, but will not forecast the short-term variations associated with recent geomagnetic activity.

6.2.5 Matching methods

An improvement on percentage gradient forecasts is to use a matching algorithm from a window of past data to find when previous occurrences of current TEC conditions were found. Three matching methods that use two different parameters, absolute TEC and percentage changes were tested. These were used separately and in combination.

a) **Absolute TEC.** This uses absolute TEC and finds the TEC data from previous days at the same local times that are closest to the current value from the windowed data. A vector, T, of length N, is produced by calculating differences between measurements from previous days and the current day, and is shown in Equation 6.5.

$$T = \sum_{w=1}^{W} \left| I_{t-24*n-w+1} - I_{t-w+1} \right| \quad [6.5]$$

The day with the most accurate match, m, is found by identifying the index of the minimum value of T. The output forecast can be generated in two ways. The first is by using the absolute TEC measured at the forecast time.

$$I_{t+\tau} = I(t+\tau, m) \quad [6.6]$$

The second uses the percentage gradient from day m for the forecast period applied to the most recent measurement.

$$I_{t+\tau} = I_t * P_g(t, m) \quad [6.7]$$

b) **Percentage Gradient.** This uses the same approach but matches the recent percentage gradient to past percentage gradient data. A vector, P, of length N, is produced by calculating differences between measurements from previous days and the current day, and is shown in Equation 6.8.

$$P = \sum_{w=1}^{W} \left| P_g(t-w, n) - P_g(t-w, 0) \right| \quad [6.8]$$

The best match, m, is found by identifying the minimum value of the vector, P, and a forecast is produced using the percentage gradient for the forecast period calculated from day m, produced by Equation 6.7.

c) **TEC and Gradient.** The final matching method uses a combination of the two parameters. The vectors T and P are combined, once the effect from each approach has been balanced, and is given below in Equation 6.9. This balancing approach is required so that both vectors equally bias the window of past data when identifying the most relevant changes.

$$C = \frac{T}{mean(T)} + \frac{P}{mean(P)} \quad [6.9]$$

The best match, m, is found by identifying the minimum value of the vector, $\boldsymbol{C}$ and used for the forecast to produce the TEC forecast using Equation 6.7.

The window sizes for the matching methods were generated by analysing data not used to test the forecasting algorithms. For this a 60-day period of 2001, from day 60 to 120 was used, with window sizes of N between 1 and 32, and W equal between 1 and 24. For gradient matching and the combined method using absolute and gradient TEC measurements, a window of the past eight days is studied using four samples for each day (N=8, W=4). For TEC matching an increased number of days was found to produce the most accurate results but fewer measurements were required for each day. For absolute TEC matching, windows of sixteen days and two samples from each day (N=16, W=2) were used.

6.3 Single-site TEC forecasting

The methods described above were tested during a twenty-day period in April 2002, which includes a strong geomagnetic storm, over forecast periods of 1, 3, 6 and 12-hour periods at a single location, Chilton (UK). It is these periods of high ionospheric variability that are of particular interest to users of forecasts. The chosen period will therefore cover the most difficult period. The variation of the geomagnetic activity, or K_p, is shown in Figure 6.1 (from the World Data Centre website, http://www.wdc.rl.ac.uk). This shows that the period has low to medium K_p for the first seven days, days 100 to 106 (April 10th to April 16th), until the commencement of the geomagnetic storm, which occurred at 06UT on day 107 (April 17th) with a maximum K_p of 7+ on days 107 and 109. The K_p is at least 3 until 21UT on day 110 (April 20th). The remainder of the period (April 21st to 30th) has low to medium activity, but the ionosphere will be recovering after the geomagnetic storm and so will still be difficult to predict accurately.

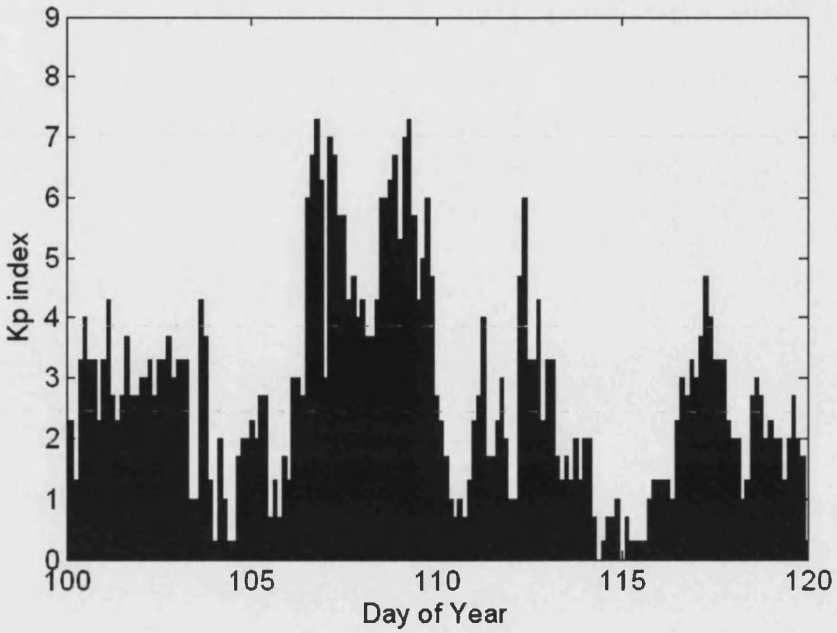

Figure 6.1. Variation of magnetic activity during the major storm from 10th to 30th April 2002 (data from WDC).

The effect of the storm can be seen from the foF2 measurement taken by the ionosonde at Chilton, UK, (from http://www.wdc.rl.ac.uk). The peak foF2 can be seen to vary greatly on day 105, with a midday value of 11.8 MHz, decreasing to daily peaks of 7.0 and 6.7 MHz for days 108 and 110. It is this dramatic change in daily magnitude of the ionosphere that must be forecast to show the technique to be successful.

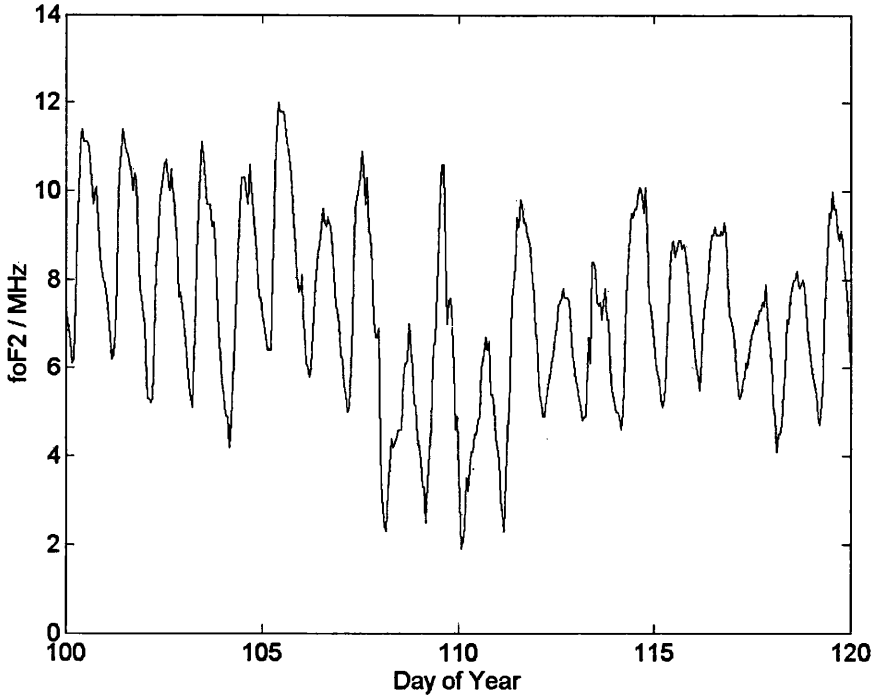

Figure 6.2. Critical frequency, foF2, from ionosonde measurements at Chilton from 10th to 30th April 2002 (data from WDC).

Reconstructions were carried out using the approach described in Section 2.4 with GPS phase data only. A time series of TEC is obtained using the reconstruction voxel closest to the location of the Chilton observatory. This latitude and longitude is 51.7°N and 1.3°W, so the voxel at 52°N and 2°W is used. Firstly, the basic approaches were tested so that they could be used as a benchmark to compare accuracy of more complex techniques. In the following plots, the red line is the measured TEC, and the blue line is the forecasted TEC. For graphs comparing the forecasted and the actual TEC the red line is the measured TEC and the blue line is the forecast TEC, produced using data up to 1, 3, 6 or 12 hour previously, depending upon the forecast period.

6.3.1 Persistence

Persistence (Equation 6.1) is the simplest approach and uses the most recent TEC measurement as the forecast. Figure 6.3 shows a comparison between measured TEC and the 1-hour forecasted TEC using the persistence method. Good agreement between the forecast and measured TEC can be seen, but this is only due to the short forecast period since the TEC changes in one hour are small.

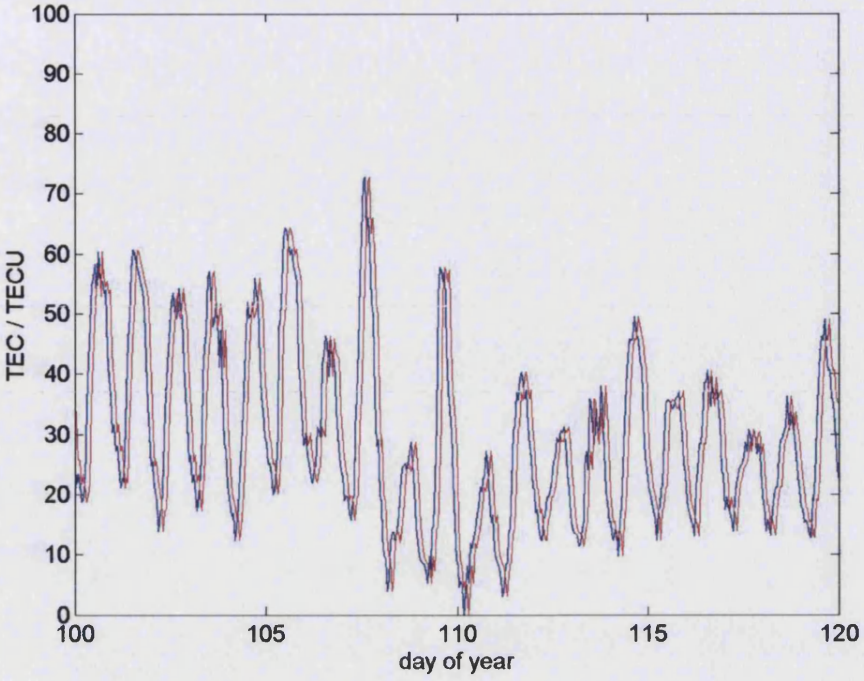

Figure 6.3. 1-hour forecast results for the persistence method,. The red line shows the forecasted value and the blue shows the measured value.

The forecast period used is then increased. Figure 6.4 shows the results for the forecast period of 3 hours. For this longer period, the ionosphere has changed due to external effects, such as the EUV radiation from the sun. Hence the forecast appears less accurate.

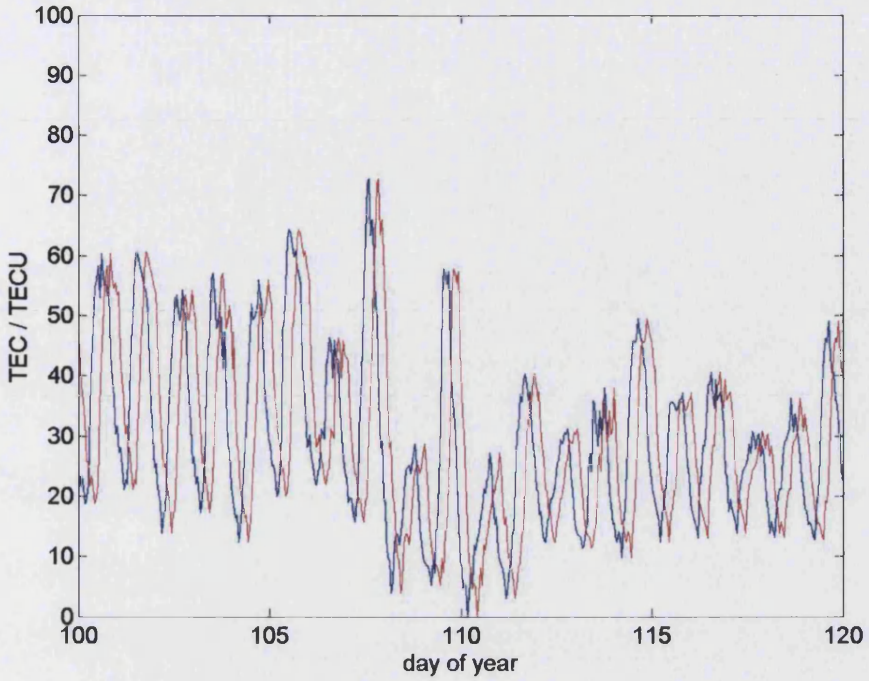

Figure 6.4. 3-hour forecast results for the persistence method,. The red line shows the forecasted value and the blue shows the measured value.

It is clear that the errors produced by this method will increase as the forecast period lengthens as the data are based upon decreasingly relevant measurements. This is shown in Table 6.1 which shows the absolute and rms errors for 1, 3, 6 and 12-hour forecasts.

Table 6.1. Absolute and rms errors for the persistence forecast method.

	1 hrs	3 hrs	6 hrs	12 hrs
Absolute (TECU)	3.30	7.88	14.08	20.70
Rms (TECU)	4.36	10.13	17.38	24.05

6.3.2 24-hour persistence

The next method to be tested is an improvement on basic persistence as the forecast is based upon measurements at the correct local time (Equation 6.2). This method will therefore produce good results when there is little change in the ionosphere from day to day. This can be the case during very low geomagnetic conditions, but in the storm part of the period studied here this will not be the case. This can be applied to forecast TEC for any period up to 24-hours ahead. The result is shown in Figure 6.5.

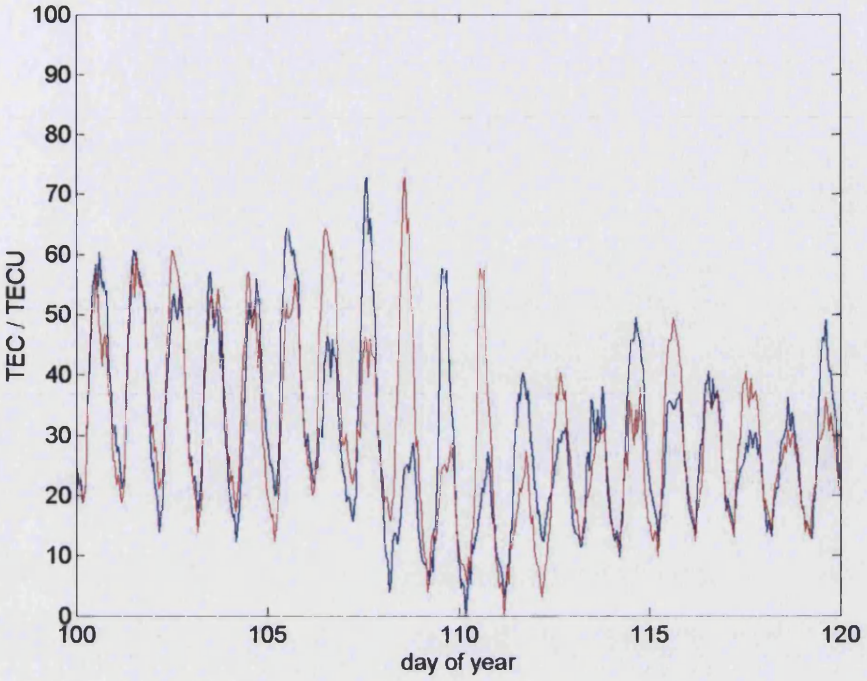

Figure 6.5. 1-hour forecast results for the persistence 24-hour method,. The red line shows the forecasted value and the blue shows the measured value.

Early in the test period, good agreement can be seen between the forecast and the measured TEC. An example is the period between days 100 to 104 where the day to day TEC variation is similar. With the onset of the geomagnetic storm, the difference between the forecast and measured TEC increases dramatically. The days that are most affected are days 106 to 110, which are influenced by storm effects, rather than general trends produced by the interactions between Sun and Earth. Over the entire period the absolute and rms errors are 7.31 and 10.78 TEC units respectively. When compared to the persistence method, it can be seen that this method produce less error for forecast periods of 3 hours and more. This method is accurate for geomagnetically quiet periods, as the day to day variation is much lower.

6.3.3 Average percentage gradient

The first two methods have both used vertical TEC measurements directly to forecast the future TEC. They can be accurate, but rely upon the conditions being stable without large day-to-day variations. For storm-time periods this is not the case and so improvements, which update the TEC depending upon recent results, must be made. This was generated by averaging the percentage variation over the forecast period from the previous three days (Equation 6.3 and 6.4).

shows the absolute and rms errors produced by this method.

Table 6.2. Absolute and rms errors for percentage gradient forecasts.

	1 hrs	3 hrs	6 hrs	12 hrs
Absolute (TECU)	2.48	3.85	5.76	8.03
Rms (TECU)	3.22	5.57	8.95	12.21

It can be seen that the errors produced are smaller than the previous two methods for forecasts periods of 6 hours and less. The 12-hour forecast has error greater than the 24-hour persistence method and therefore no advantage is gained by using the changes of vertical of previous days. The graphical comparison between the forecast and measured vertical TEC using the percentage gradient is shown in Figure 6.6 to Figure 6.8 for 1, 3 and 6-hour forecasts.

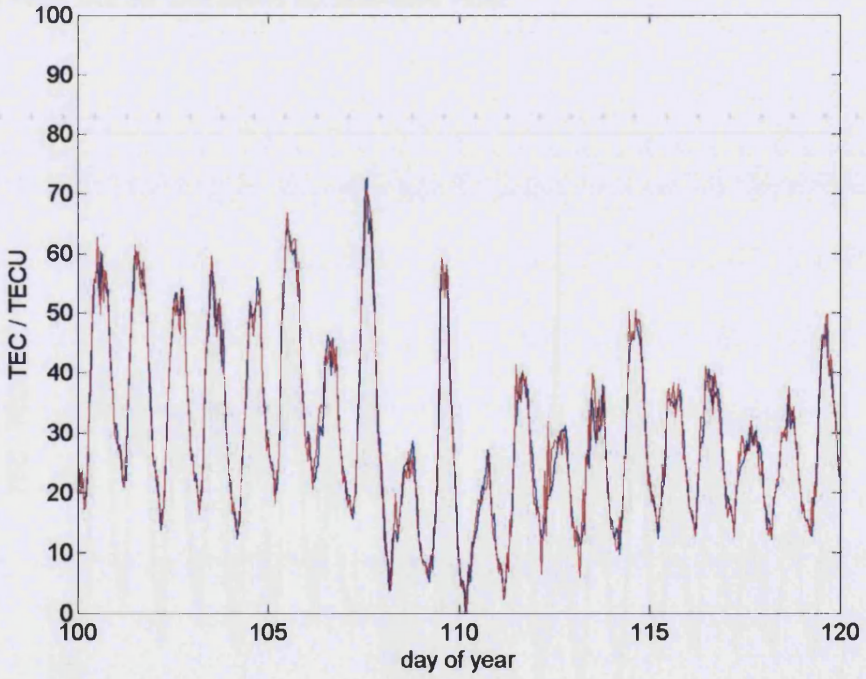

Figure 6.6. 1-hour forecast results for the percentage gradient method. The red line shows the forecasted value and the blue shows the measured value.

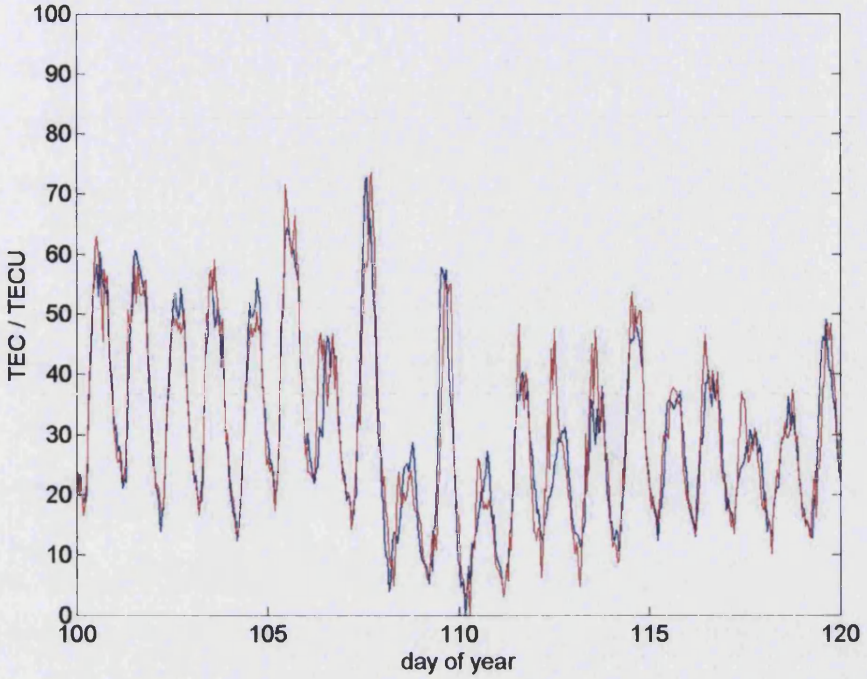

Figure 6.7. **3-hour forecast results for the percentage gradient method. The red line shows the forecasted value and the blue shows the measured value.**

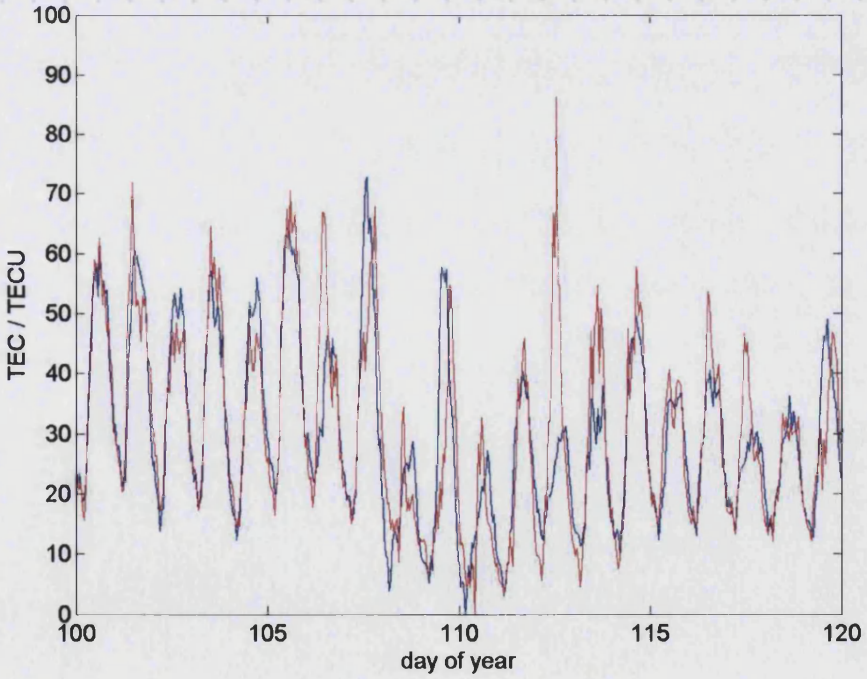

Figure 6.8. **6-hour forecast results for the percentage gradient method. The red line shows the forecasted value and the blue shows the measured value.**

The changes can be seen to be modelled accurately for the forecast period of one-hour, Figure 6.6), as the two lines follow closely and have low absolute and rms error. For the three-hour forecast period, Figure 6.7, some larger errors are apparent at the midday peak of days 112 to 114. The 6-hour forecast, Figure 6.8, show larger errors for days 112 to 114. Another error can also be seen for day 106. These days are similar, in that they are both part of the negative phase of the storm. This will have a different variation when compared to the previous days. Without information relevant to the negative edge of the storm in the previous three days, this approach will not reproduce the correct vertical TEC variations.

In general, the use of percentage gradients is useful for forecasting vertical TEC for short periods, although errors are introduced when external events, such as geomagnetic storms, change the properties of the ionosphere and the daily variation differs greatly from the previous days. The methods that will now be introduced use the percentage gradients calculated from the previous days, but instead of always using only an average of the previous three days, a match to recent vertical TEC is found and the percentage gradient is used from that day.

6.3.4 IRI model

The IRI model was described in Chapter 3. Here the model has been used to reconstruct the ionosphere for over two years and a short period of this can be used to show its accuracy during the large variation produced by the geomagnetic storm. The result for the method is shown below in Figure 6.9.

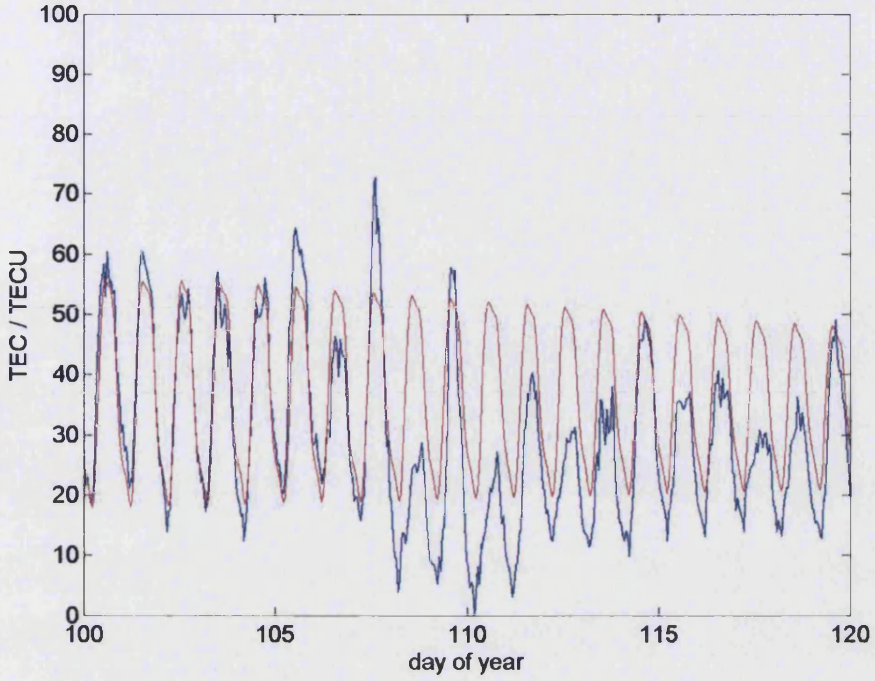

Figure 6.9. IRI-95 TEC values over Chilton. The red line shows the IRI forecasted value and the blue shows the measured value.

The figure shows that the IRI produces quite accurate predictions for the first five days of the period before the storm commencement, with TEC accuracy of absolute and rms errors of 3.50 and 4.28 TEC units respectively for days 100 to 104. During and after the storm the errors are found to be much larger with greatest error being produced during days 108 and 110. These have absolute errors of 20.0 and 23.1 TEC units respectively, and rms errors of 21.2 and 23.9. For the entire period the absolute and rms errors are 9.3 and 11.7 TEC units respectively.

6.3.5 Matching methods

The methods described in Section 6.2.5 are now tested using the data from 10th to 20th April 2004 at Chilton.

1) TEC Matching with absolute TEC output

The first matching method used a window of past data that was entirely based on absolute TEC measurements (Equations 6.5 and 6.6). The first choice of output method used the absolute TEC that had been used to match to the original data. The absolute and rms TEC errors are given in Table 6.3 and are greater than the gradient matching method and other techniques analysed earlier in this chapter.

Table 6.3. Absolute and rms errors for TEC matching (1) forecasts.

	1 hrs	3 hrs	6 hrs	12 hrs
Absolute	4.61	5.56	6.93	8.29
rms	6.32	7.97	9.82	11.28

The results are shown in Figure 6.10 and Figure 6.11 for the 1 and 3-hour forecasts using this method. It can be seen that large errors are produced for day 108, which has TEC that is much lower than any data that is included in the matching window. There are also large errors produced during the period shortly after sunrise where the matching algorithm has least knowledge of how the TEC will change as the Sun effects the TEC magnitude.

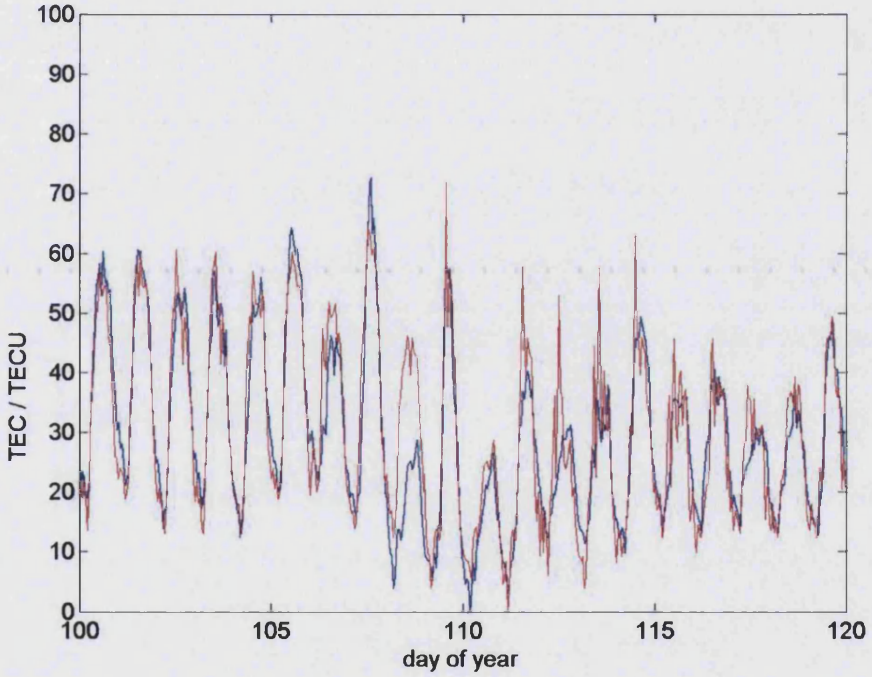

Figure 6.10. 1-hour forecast results for TEC matching method. The red line shows the forecasted value and the blue shows the measured value.

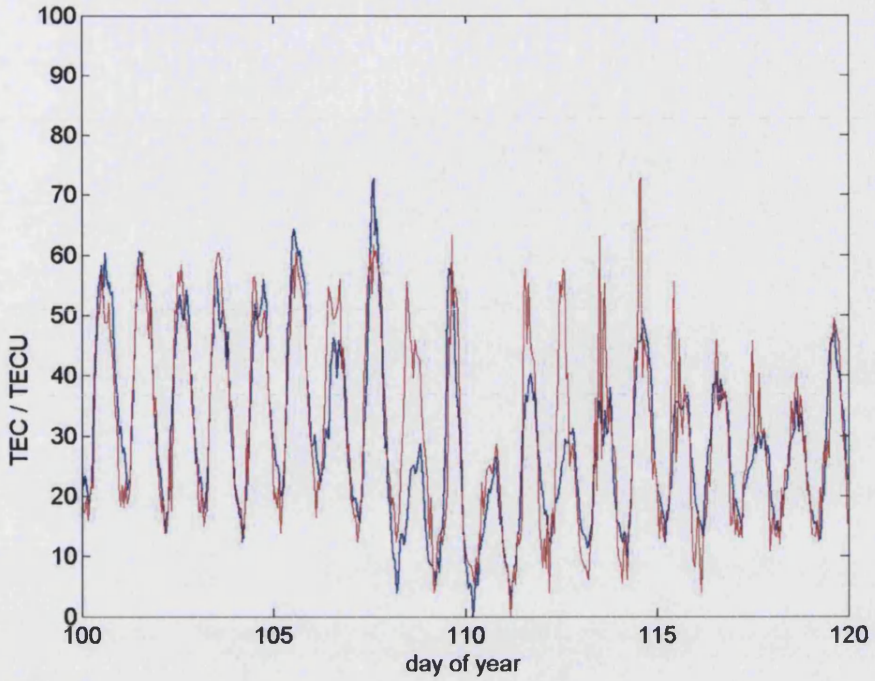

Figure 6.11. 3-hour forecast results for the TEC matching method. The red line shows the forecasted value and the blue shows the measured value.

This approach of using absolute TEC to produce the output can be seen to be inappropriate, as it is not sensitive to circumstances where the recent measurements are different in magnitude from the data in the matching window. The approach must be tested using an alternative output method to verify whether it is the output approach or the matching criteria that is the source of the increased error.

2) TEC matching using percentage gradient

Using the same matching algorithm as was used in the previous study, the forecast output is changed by using the percentage gradient of the best match, instead of the absolute TEC and the end of the forecast period (Equations 6.5 and 6.7). This should help to improve the forecast by not introducing large errors on days where data are not similar in magnitude to those of recent measurements.

shows the absolute and rms errors. An improvement is shown compared to the absolute TEC output method, although the accuracy is not as good as for the results produced by matching the temporal gradients of recent data with past data.

Table 6.4. Absolute and rms errors for TEC matching (2) forecasts.

	1 hrs	3 hrs	6 hrs	12 hrs
Absolute (TECU)	4.33	5.41	6.84	7.94
Rms (TECU)	5.97	8.43	10.12	10.97

Figure 6.12 and Figure 6.13 show the 1 and 3-hour comparison for this method.

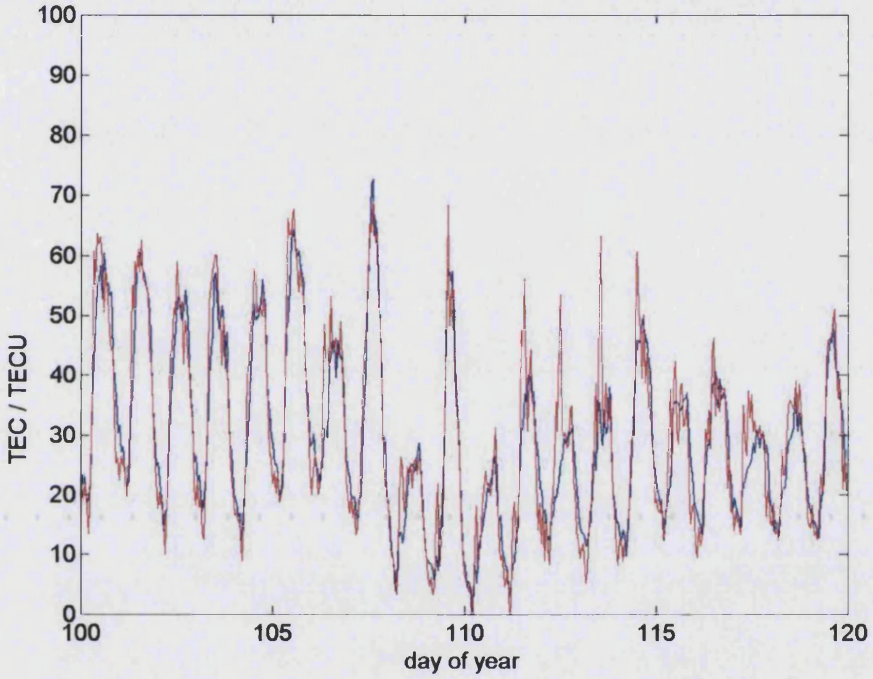

Figure 6.12 1-hour forecast results for the TEC matching method. The red line shows the forecasted value and the blue shows the measured value

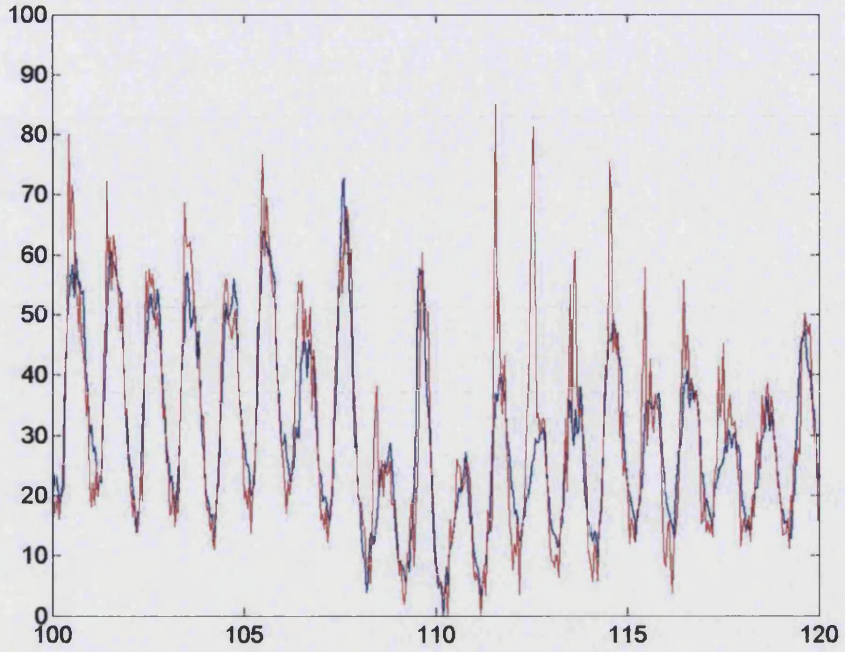

Figure 6.13. 3-hour forecast results for the TEC matching method. The red line shows the forecasted value and the blue shows the measured value.

Overall this method provides good accuracy for the period of the storm, but the accuracy decreases after the storm finishes. The geomagnetic conditions are in the region of medium to quiet and the absolute TEC matching method matches storm period TEC changes to these forecast periods. The gradient matching method did match these periods well, and so by combining the two methods using the past measurements, a forecast that best predicts the magnitude of the TEC may be found.

3) Percentage gradient matching

The next matching approach uses a window of past TEC gradients to match with the most recent changes in TEC to produce a forecast for the variation of the TEC (Equation 6.7 and 6.8). The analysis was carried out for the forecast periods and the absolute and rms TEC errors are given in Table 6.5.

Table 6.5. Absolute and rms errors for gradient matching forecasts.

	1 hrs	3 hrs	6 hrs	12 hrs
Absolute (TECU)	2.46	3.78	5.60	7.37
Rms (TECU)	3.31	5.47	8.19	10.24

These results have smaller errors than those produced by the average percentage approach shown in Section 6.4.3, for all forecast periods. It can be seen that the there is an improvement for longer forecast periods, with only a 1% improvement for 1-hour, but an 8% improvement for 12 hours. The performance of the 12 hour forecast is, however, worse than the result produced using the data from the previous day, so there is still some improvement to be gained. The graphical comparisons for the 1, 3 and 6-hour forecasts are shown in Figure 6.14 to Figure 6.16

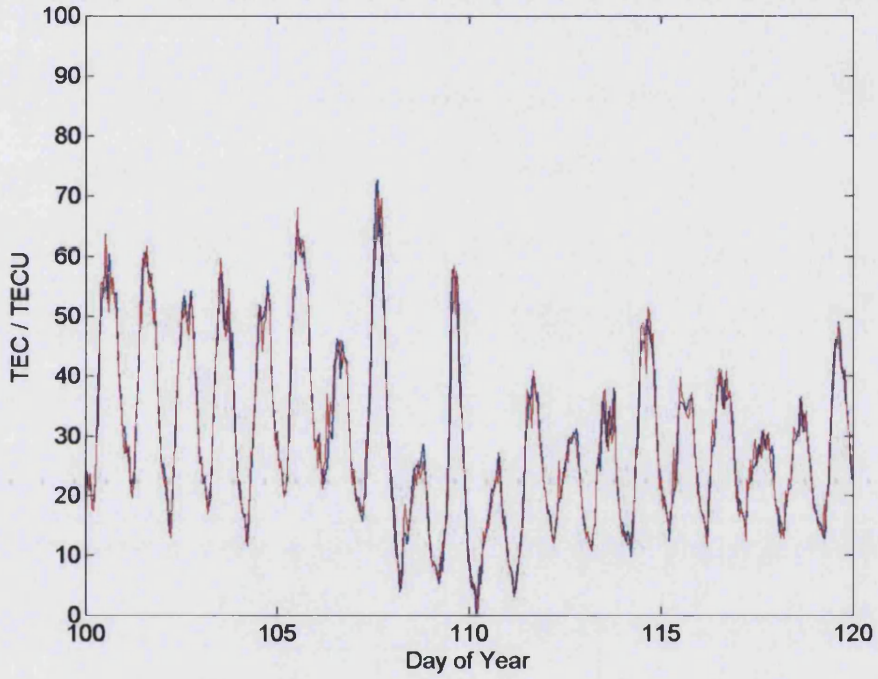

Figure 6.14. 1-hour forecast results for the percentage gradient matching method. The red line shows the forecasted value and the blue shows the measured value.

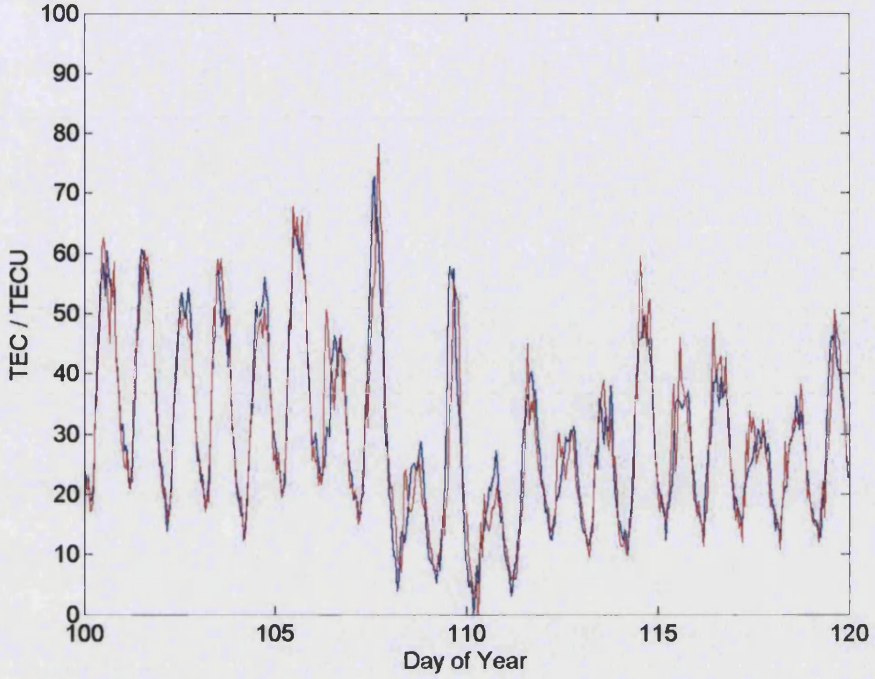

Figure 6.15. 3-hour forecast results for the percentage gradient matching method. The red line shows the forecasted value and the blue shows the measured value.

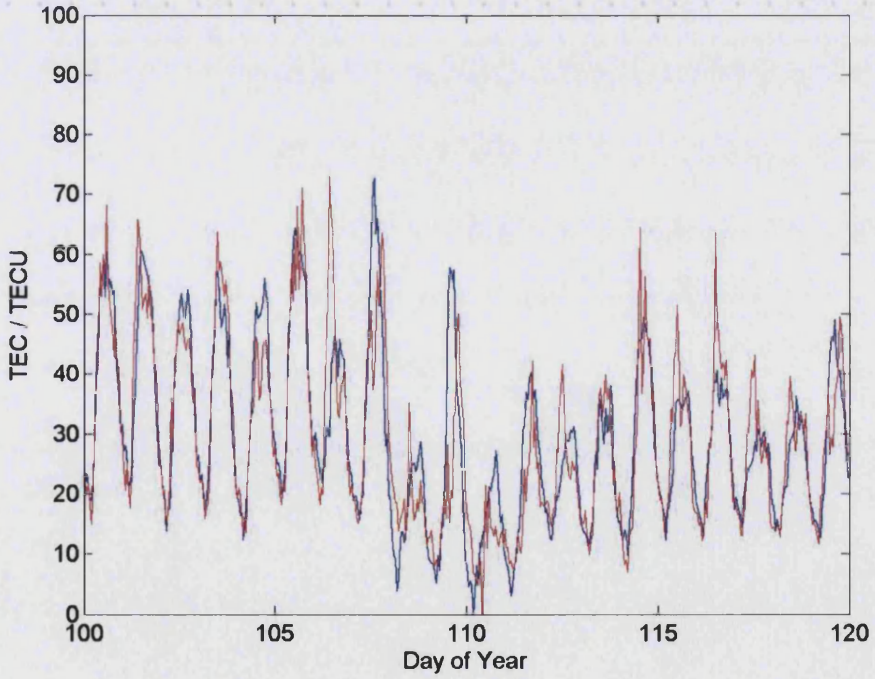

Figure 6.16. 6-hour forecast results for the percentage gradient matching method. The red line shows the forecasted value and the blue shows the measured value.

The result for the 1-hour forecast is again accurate due to the short forecast period and shows a slight improvement in accuracy

4) TEC and Gradient matching combined

By using two data parameters, an improved result for the current and past variation can be achieved (Equations 6.7 and 6.9). The previous matching methods only use one parameter and both of these approaches produced inaccurate forecasts at given times because of mismatches to the windowed data. A good match of the percentage change in TEC will not necessarily produce a good forecast because the absolute TEC is not appropriate. The results for the four forecast periods are given in Table 6.6

Table 6.6. Absolute and rms errors for TEC gradient and absolute combination matching forecasts.

	1 hrs	3 hrs	6 hrs	12 hrs
Absolute (TECU)	2.42	3.75	5.19	6.33
Rms (TECU)	3.23	5.18	7.26	8.54

It is clear that the TEC and gradient matching method does provide the best accuracy for these single site forecasts. The comparisons for 1, 3 and 6-hour forecast periods are shown in Figure 6.17 to Figure 6.20.

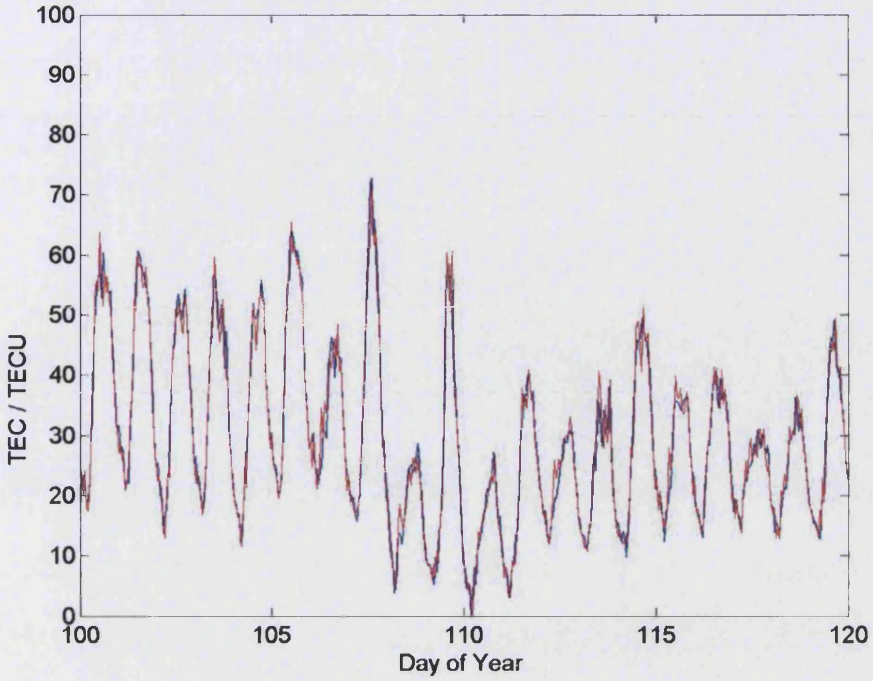

Figure 6.17. 1-hour forecast results for the gradient and absolute TEC combination matching method. The red line shows the forecasted value and the blue shows the measured value.

For the 1-hour forecast there is again minimal difference between the forecast and the measured TEC. The accuracy is a 2% improvement on average percentage gradient and a 1% improvement on the gradient matching method.

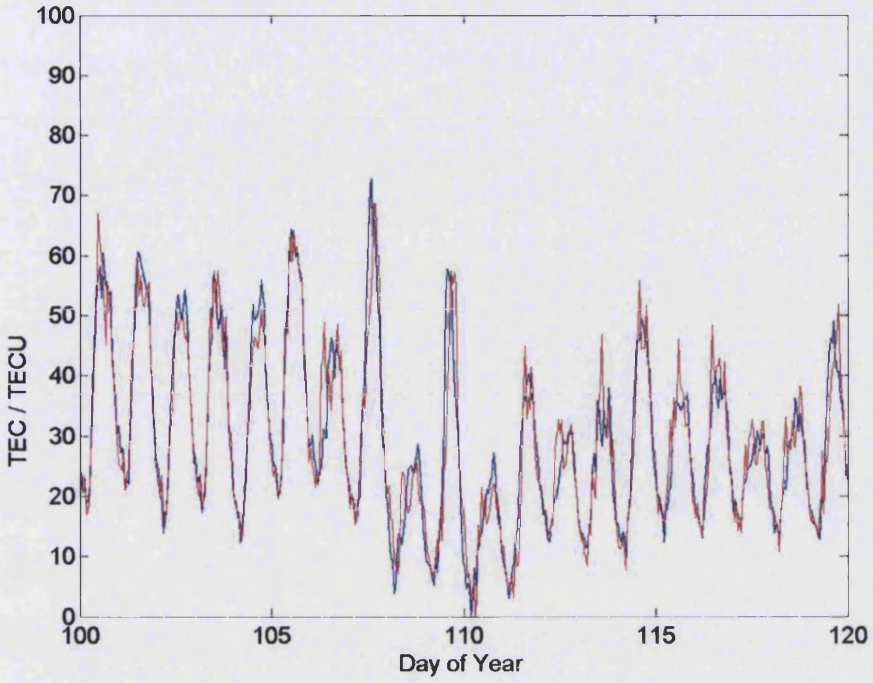

Figure 6.18. 3-hour forecast results for the gradient and absolute TEC combination matching method. The red line shows the forecasted value and the blue shows the measured value.

As the forecast period increases, so do the errors produced by the TEC forecast. The greatest errors can be seen during the period between sun rise and the daily peak of TEC. This is not as large as the errors produced by previous forecasting techniques and afternoon and night time forecasts are very accurate.

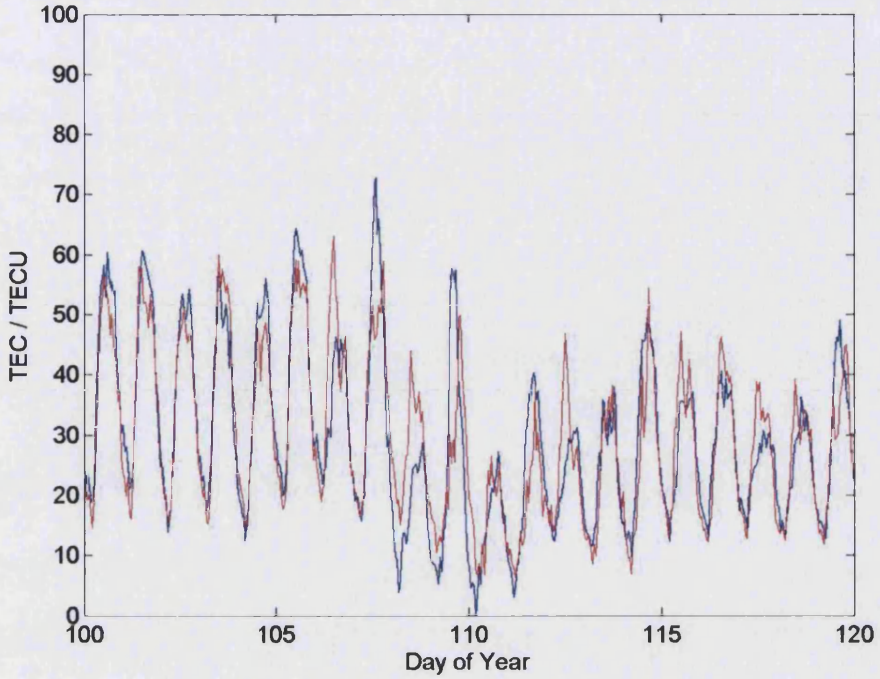

Figure 6.19. 6-hour forecast results for the gradient and absolute TEC combination matching method. The red line shows the forecasted value and the blue shows the measured value.

A summary of all the accuracies for the methods in the time series study are shown in Table 6.7, with the lowest error for each hour and error type shown in bold. In general the lowest error is given by the matching method using both TEC and TEC gradient. The only improvement was the percentage gradient method for the shortest time period in the rms error. The difference between the two was negligible at 0.01 TEC units.

Table 6.7. Summary of forecasting accuracies for storm period in April (all values are in TECU).

Method Type	Equation	Error type	Forecast period (hours)			
			1	3	6	12
Persistence	6.1	absolute	3.30	7.88	14.08	20.70
		rms	4.36	10.13	17.38	24.05
Persistence 24	6.2	absolute	7.31	7.31	7.31	7.31
		rms	10.78	10.78	10.78	10.78
Percentage Gradient	6.3 and 6.4	absolute	2.48	3.85	5.76	8.03
		rms	**3.22**	5.57	8.95	12.21
IRI	Section 6.3.4	absolute	9.25	9.25	9.25	9.25
		rms	11.65	11.65	11.65	11.65
TEC Match (1)	6.5 and 6.6	absolute	4.61	5.56	6.93	8.29
		Rms	6.32	7.97	9.82	11.28
TEC Match (2)	6.5 and 6.7	absolute	4.33	5.41	6.84	7.94
		Rms	5.97	8.43	10.12	10.97
Gradient Match	6.7 and 6.8	absolute	2.46	3.78	5.60	7.37
		rms	3.31	5.47	8.19	10.24
Combination Match	6.7 and 6.9	absolute	**2.42**	**3.75**	**5.19**	**6.33**
		rms	3.23	**5.18**	**7.26**	**8.54**

6.3.6 Year study

The forecasting methods were used to determine the best method for the entire 2002 period. This is to verify the accuracy of the methods during quiet periods as well as during the April storm period. The absolute and rms errors are shown in Table 6.8.

Table 6.8. Absolute and rms errors for forecasting methods in 2002.

Method Type	Error type	Forecast period (hours)			
		1	**3**	**6**	**12**
Persistence	absolute	3.41	7.90	13.71	19.45
	rms	4.90	11.26	18.50	24.63
Persistence 24	absolute	4.21	4.21	4.21	4.21
	rms	6.30	6.30	6.30	6.30
Percentage Gradient	absolute	2.21	3.33	4.44	5.26
	rms	3.15	5.15	7.30	8.25
Gradient Match	absolute	**2.11**	3.23	4.31	5.09
	rms	**2.95**	4.87	6.73	7.62
TEC Match	absolute	3.39	3.76	3.97	4.03
	rms	4.39	5.49	5.74	5.81
Combination Match	absolute	2.18	**2.85**	**3.42**	**3.87**
	rms	3.04	**4.13**	**5.08**	**5.68**

Throughout the year, the errors were generally lower than the shorter period during the April geomagnetic storm examined in the first part of this chapter. Persistence produces the greatest error for all forecast periods, except for a 1-hour forecast, when 24-hour persistence is least accurate. 24-hour persistence is better for forecasts of 3 hours and more, and the ability of the basic persistence approach is minimal. Percentage gradient produces an improvement to the result from the TEC of the previous day for shorter forecast periods of 1 and 3 hours, but does not provide improvement beyond this.

6.4 Wide-area TEC forecasting

The time series methods used for the April geomagnetic storm period were applied to wide-area TEC maps. The methods are applied independently to each latitude and longitude voxel with a window of past data relevant to that particular voxel. An example is shown in Figure 6.20. It was found that when these matching methods were used to produce wide-area images they produced artificial features. This can be seen by the differences between the two plots in Figure 6.20, which shows the MIDAS reconstruction (on the left) and the forecast image (on the right) using the gradient and TEC matching algorithm for the same time. Added structure produced by the method can be seen north of the UK and in Eastern Europe. A new method would need to be developed to produce more realistic regional area forecasts, without the possibility of generating local errors such as generated here.

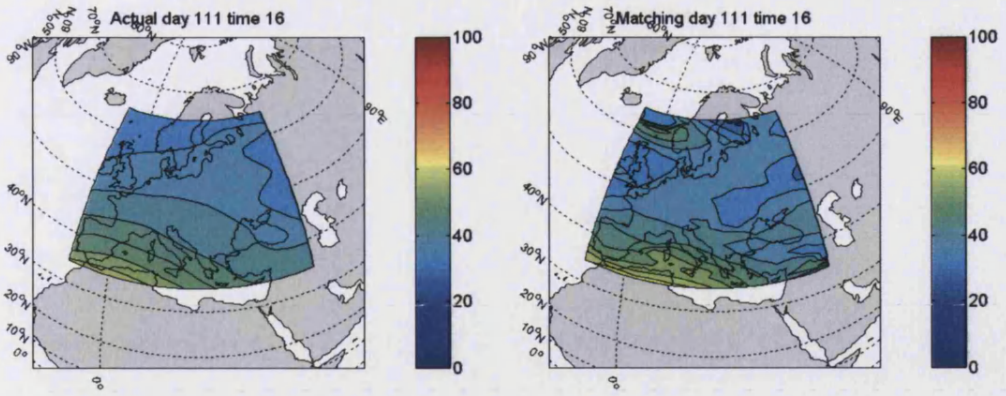

Figure 6.20. Images of vertical TEC for MIDAS (left) and matching method (right) for 16:00 UT, 21st April 2002.

6.4.1 IRI gradient method

Absolute TEC predictions from the IRI model are often inaccurate as they are based on long-term averages of ionospheric conditions. IRI models the temporal changes during the day, and so it was possible that the short-term changes of TEC from IRI may be useful for forecasting. For this reason, a method using temporal gradients from the IRI model was developed to forecast regional area images. The method consisted of the following three steps:

(1) Create separate MIDAS and IRI TEC images for Europe
(2) Calculate IRI percentage gradients at each grid point for the forecast period
(3) Apply these gradients to the MIDAS image to produce a forecast

The formula expressing this method for a forecast period, τ, and a current time, t, is:

$$I_{t+\tau} = I_t \left[1 + \frac{I_{t+\tau}^{IRI} - I_t^{IRI}}{I_t^{IRI}} \right] \qquad [6.10]$$

The IRI temporal gradients were used to forecast daytime European images during April 2002 to evaluate the method. Example forecasts are shown for a medium geomagnetic activity day (25th April, Figure 6.21) and a high geomagnetic activity day (22nd April, Figure 6.22). To evaluate the method, the actual MIDAS TEC image (labelled a in both figures) is compared to the IRI model (labelled b), and the 1-hour (labelled c) and 3-hour (labelled d) forecasts for that time. The images all display TEC measured in TEC units.

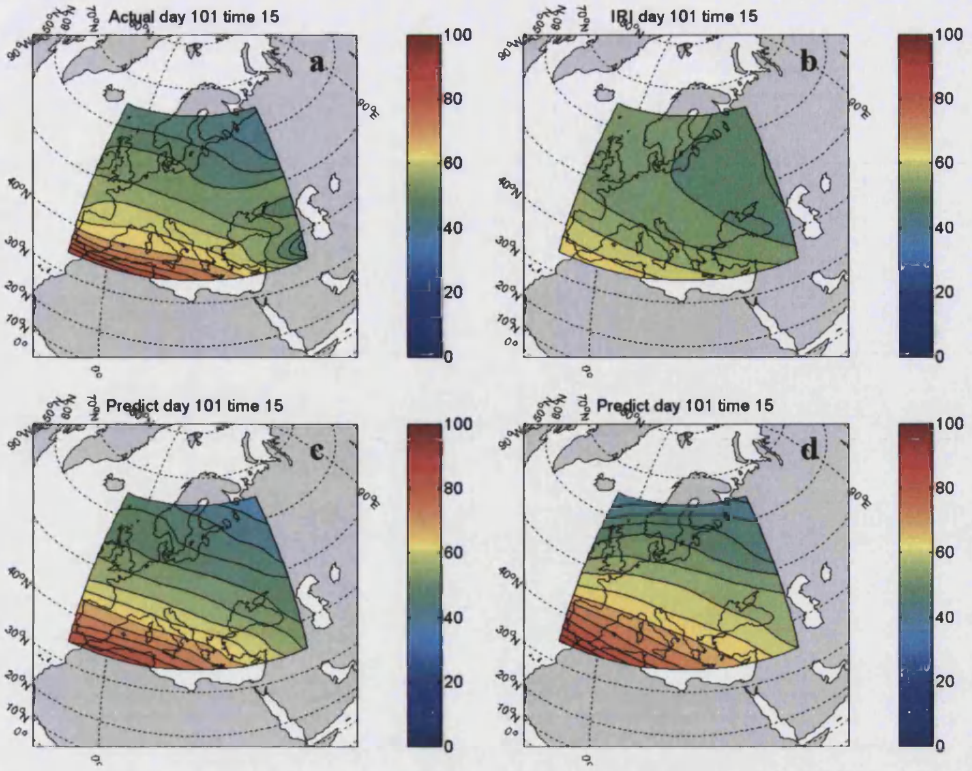

Figure 6.21. Vertical TEC images for MIDAS (a), IRI model (b) and IRI gradient forecasts for 1 (c) and 3-hour (d) at 15:30 UT, 25th April 2002.

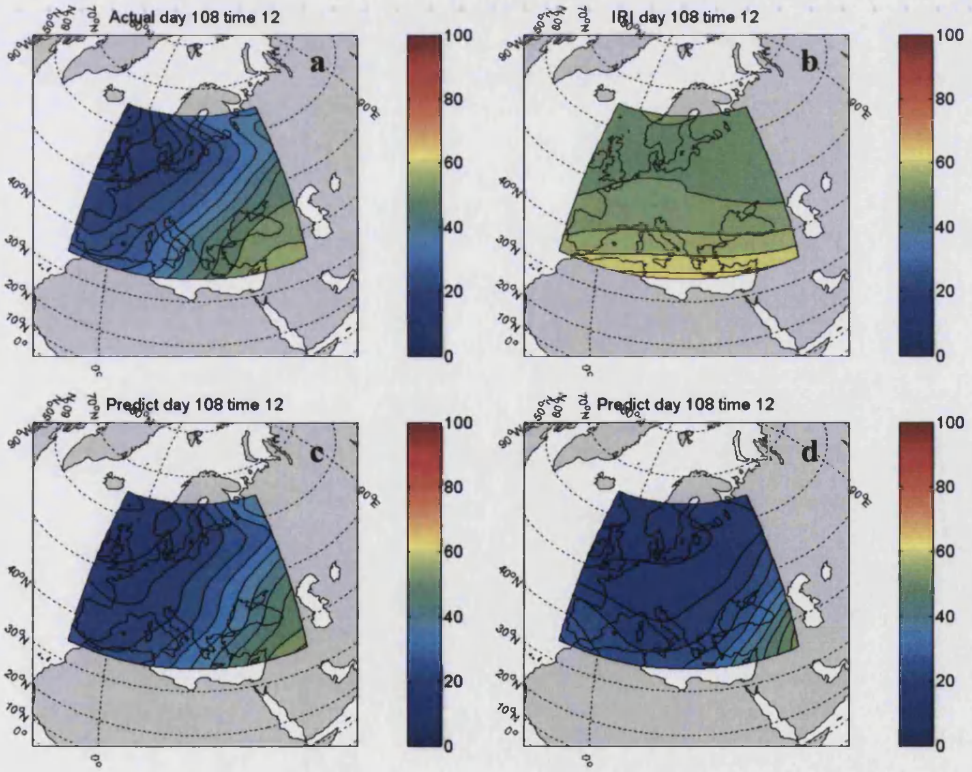

Figure 6.22. Vertical TEC images for MIDAS (a), IRI model (b) and IRI gradient forecasts for 1 (c) and 3-hour (d) for 12:30 UT, 22nd April 2002.

These images show that the IRI gradient method produces quite accurate results during quiet to medium geomagnetic conditions. This accuracy is an improvement over the instantaneous IRI maps, which do not take account of recent geomagnetic conditions. The accuracy is not as good for periods of high geomagnetic activity, due to limitations in the accuracy of the temporal TEC gradients in IRI for these periods, since the IRI is related to monthly median ionosphere changes. Nonetheless, this gradient method is still a large improvement on the forecast images produced by the IRI model alone.

6.5 Error analysis using geomagnetic activity

The daytime forecasting errors for 2002 were calculated and then separated according to geomagnetic activity. It was found that the negative storm effect was the dominant factor in the error and that the K_p from the previous day was a good indicator of this. Plots of these 'K_p separated' forecast errors for 1, 3 and 6-hour periods ahead are shown in Figure 6.23. The four methods compared are the IRI percentage gradient (dark blue), absolute IRI (green), 24-hour persistence (red) and 3-day mean percentage gradient (light blue).

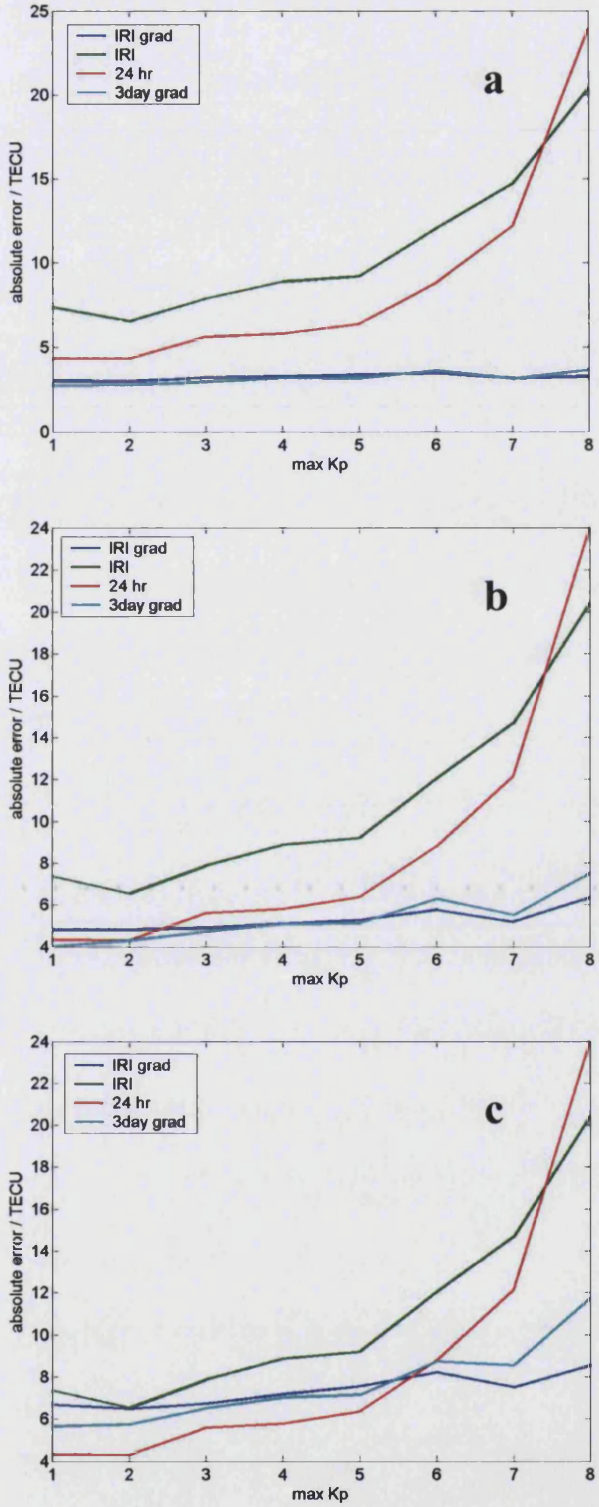

Figure 6.23. Forecast errors for 2002 separated by K_p for 1 (a), 3 (b) and 6-hour (c).

The least accurate method can be seen to be the IRI model, which has highest error for all except the highest geomagnetic activity where 24-hour persistence is least useful. The most accurate methods for short forecast periods are the percentage gradient methods, which produce

similar accuracies for low to medium geomagnetic activity. The IRI gradients methods are more accurate than using measured gradients for the occurrences of high K_p index. For the longest forecast period tested, IRI temporal gradients again produced lowest error for high geomagnetic activities of greater than K_p index of 5. The 24-hour persistence method provided lowest errors for K_p index of 5 and below.

Percentage gradients can be seen to give a reliable forecast of TEC under all geomagnetic conditions, which are not liable to produce large errors. The overall forecasting accuracy can be improved by using several methods depending upon the recent geomagnetic activity. Overall, absolute daytime TEC forecasting error was found to be less than 5 TEC units for forecast periods of 6-hours by using 24-hour persistence. It is most accurate for low K_p index where day to day TEC variation is minimal.

6.6 Conclusions

The accuracy of various methods have been tested to estimate the use of the approaches to the forecasting of the ionosphere. Initially the methods were tested using a time series study based at the location of the Chilton ionosonde. It was found that simple approaches gave good accuracy during quiet geomagnetic conditions and for short forecast periods. For longer and more disturbed periods, more advanced methods are required. This is because accurate forecasts as large errors can be produced by the basic techniques due to poor modelling of the large day to day variations. Matching methods were shown to produce the best results for the time series study, with the best results being produced by a combination of using absolute and temporal gradients of recent TEC measurements.

When the matching methods were used to produce wide-area images it was found that small-scale artefacts were produced during daytime forecasts. By using the temporal gradients produced by the IRI model to generate the forecast image, the possibility of producing these features was reduced. When estimating the accuracy, it was found that the errors produced by the forecasting methods were correlated with the maximum K_p from the previous day. This is because it is a good indicator of the possibility of large changes in TEC, produced by geomagnetic storms, for example by decrease of TEC expected by the negative phase of a storm. Improvements in forecasting accuracy can be achieved by altering the forecast method in accordance with K_p and forecast time. Finally, some improvements to the IRI gradient method are required for the early phase of a geomagnetic storm due to limitations of the IRI gradients during these times.

Further work using this forecasting approach is carried out in the next chapter to test this method for producing wide-area images during the night. This period will have more local variation caused by features such as the main trough, a night time feature that has a distinct southerly shift as the night develops. This movement would not be forecast using IRI gradients alone and require a separate approach to help replicate this.

Chapter 7 Ionospheric forecasting at night

7.1 Abstract

In this chapter, the focus is on forecasting the ionospheric TEC during the night. The main feature of the night-time ionosphere over Europe is a depletion known as the mid-latitude trough. A method to detect the presence and location of a trough in the TEC images is introduced. First, modelling approaches are developed to predict the location of the trough; these were found to be of comparable accuracy to previous recorded studies. Basic forecasting approaches are tested, and it was found that a constant velocity trough was less accurate than a variable-velocity trough. Least-mean-square fits are then applied using different combinations of parameters to produce a positional forecast for the trough. These show that the most useful inputs were the previous trough position and the geomagnetic activity. The combination of this movement model and the temporal gradients from IRI are shown to provide the most accurate TEC and trough positional results in forecasted images from the night-time.

The method described in the previous chapter, which used the temporal gradients produced from the IRI-95 model, can be used to predict the future state of the ionosphere. However, this method will not generate movement of a feature in any particular direction. The main feature of the ionosphere during the nighttime in the mid-latitude region is the main or mid-latitude trough, which moves south during the night. IRI temporal gradients alone will produce only stationary features. An improvement of this approach will be to use a feature recognition algorithm and a movement model.

MIDAS has been used previously to study the imaging of the main, or mid-latitude, trough by Meggs et al. (2005). This used independent measurements from incoherent scatter radar to demonstrate that GPS imaging can reveal the location and structure of the main trough.

Previous trough modelling approaches were described in Section 1.1.4. The studies use equations of the form shown in Equation 7.1.

$$\Lambda_t = \Lambda_0 - \alpha Kp - \beta t \qquad [7.1]$$

The three coefficients Λ_0, α and β relate to the midnight trough position (geomagnetic latitude), magnetic activity and local time parameters and the studies have found values in the

ranges, 62.2° to 66.3°, 1.3 to 2.4 and 0.5 to 1.4. Variations between these studies are due to the technique used, the location of the measurements and the differing subsets of data dependant upon the local time and solar cycle. The use of GPS phase data from many sites around Europe means that images cover a wide region and provide more frequent trough measurements than the previous studies, which relied upon a small chain of receivers or a lone low-earth-orbit satellite.

These previous studies have mainly focused upon the need for ionospheric models, such as IRI, to include an accurate representation of the trough, so the ionospheric maps produced can be more realistic. Although these previous studies have looked at the time dependence of the trough and the ability to produce an overall model, the short-term movement and forecasting of the trough has not been studied. The studies did not have continuous data sets and so trough occurrences had to be matched by parameters, and not the short-term movement of the trough. In this study the data set is continuous and so, such analysis can be undertaken.

7.2 Further simulation of MIDAS imaging

The accuracy of MIDAS was shown by simulation using IRI in Chapter 4. IRI, however, is a median monthly representation and does not produce strong latitudinal gradients as would be generated by the main trough. The imaging approach must be tested to ensure it can reproduce these gradients as well as the smoothed gradients alone. Here, a simulation is carried out using an approach similar to that of Chapter 4 but including a representation of the trough. The moving trough model used is that detailed in Collis and Haggstrom (1988). This was applied to an IRI-95 simulated ionosphere, and a K_p index of 5 was used. This was used to simulate GPS RINEX data for the European receivers. This input data was put into the MIDAS algorithm, and the output results were then compared with the model input to determine the accuracy of the algorithm.

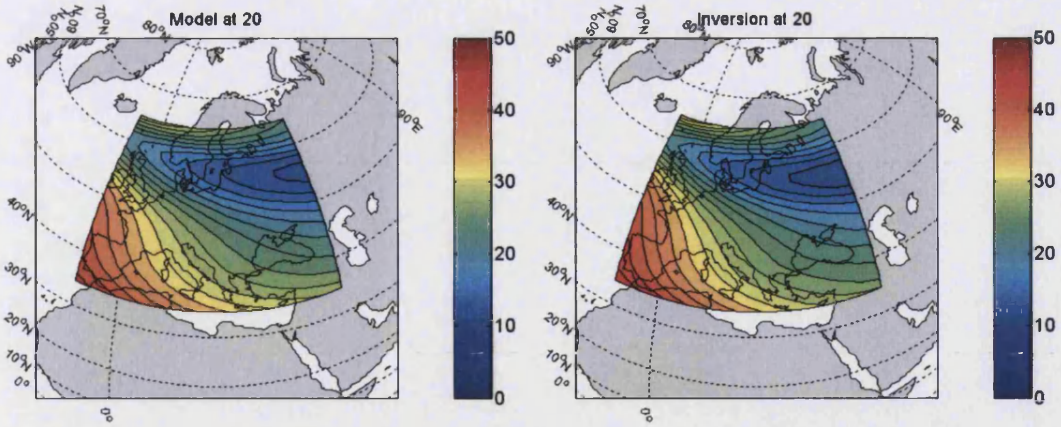

Figure 7.1. Vertical TEC images at 20:30 UT 10th April 2002, in TEC units, for the input model (left) and the MIDAS inversion output (right).

Figure 7.1 shows an example of a comparison between a model ionosphere and the MIDAS inversion of that simulated data for 20 UT on the 10th April 2002. The two images are very similar and shows that MIDAS can reconstruct the ionosphere including the trough. A further simulation study using IRI reconstructions for the whole of 2002 (see Chapter 5) showed that the output inversion from MIDAS had a mean absolute TEC error of 0.64 TECU and a mean percentage TEC error of 2.5%. Both of these studies demonstrate that MIDAS is able to reconstruct vertical TEC accurately.

7.3 Trough detection method

In this study, MIDAS is used to reconstruct electron density, to obtain the TEC of the ionosphere over Europe using differential phase measurements from the dual-frequency, ground based, GPS receivers shown in Figure 5.1. MIDAS was previously described in Section 2.4. Reconstructions were produced over a region covering longitudes 10°W to 50°E and latitudes between 40°N and 65°N using voxels, or 3D pixels, of constant electron concentration of size 4° longitude by 1° latitude and 50 km height. A single TEC map for each hour is produced by summing the vertical columns of voxels of the image at the centre of the one-hour movie period.

The images were analysed to study the presence of a trough, along each line of geographic longitude for every hour in the period between January 2001 and December 2003. An example trough is shown in Figure 7.2.

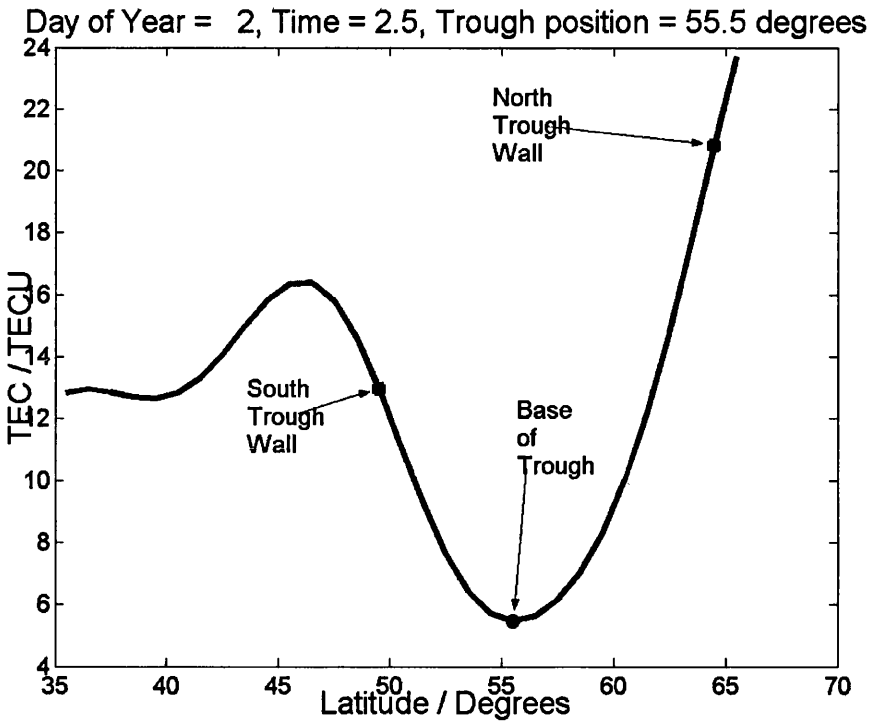

Figure 7.2. A distinct trough measured at 02:30 UT, 2nd January 2002.

The trough was detected automatically by using the following criteria:

1. There must be a north and south wall with a minimum turning point between these walls.
2. This minimum must be below 80% of the average TEC in the search region.
3. A trough cannot move more than 5° north or south in a single hour.
4. Only occurrences in which a trough was detected in the previous hour are included in the final analysis.

Constraints 3 and 4 were included as the trough is a long-lived feature lasting throughout the night, and these will reduce the likelihood of including other short-term features in the analysis. The analysis was first carried out in the geographic coordinate system that was used to reconstruct TEC. Studies using geomagnetic coordinates were produced using troughs located along geographic longitudes, but with the search longitude and the measured latitude converted into the geomagnetic domain.

Figure 7.3 and Figure 7.4 show examples of the general trends of the trough data that was analysed. The results shown are taken from one longitude (2°W), and show the probability that a trough occurred at a particular local time or month of the year. In Figure 7.3, data from January 2002 was used, and it can be seen that the nearly all of the troughs are seen in the night-time

ionosphere. In Figure 7.4, all of the data from 2002 was used. It can be seen that the majority of troughs observed are during the winter months. Both of these follow general trends shown in a previous study by Karpachev and Afonin (1998) (see Figure 1.5). The differences between the results from Karpachev and Afonin (1998) and MIDAS, are due to the differing limits set by the two imaging processes.

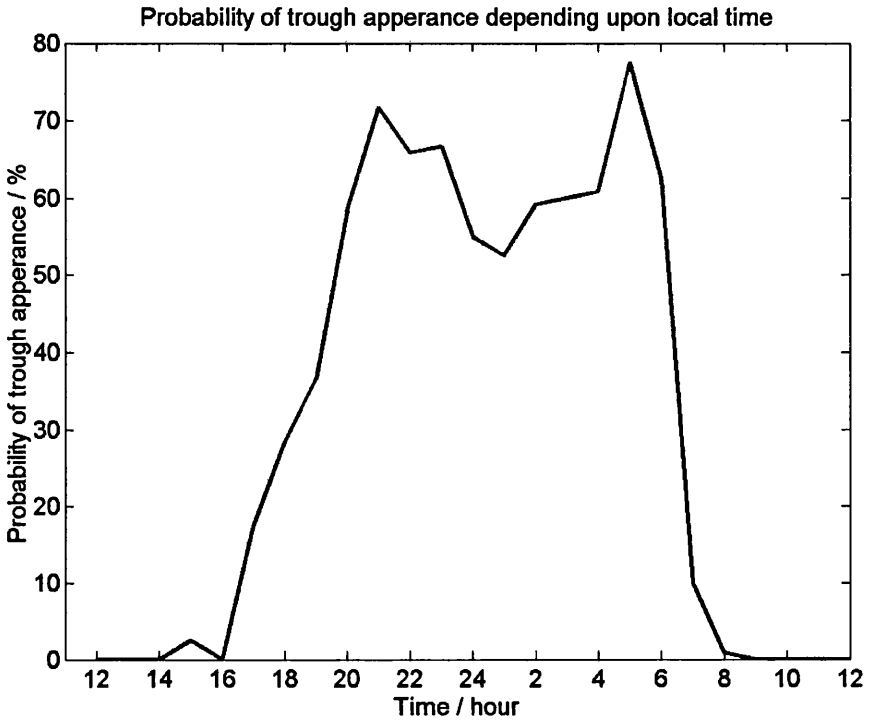

Figure 7.3. Probability of trough occurrence in January 2002.

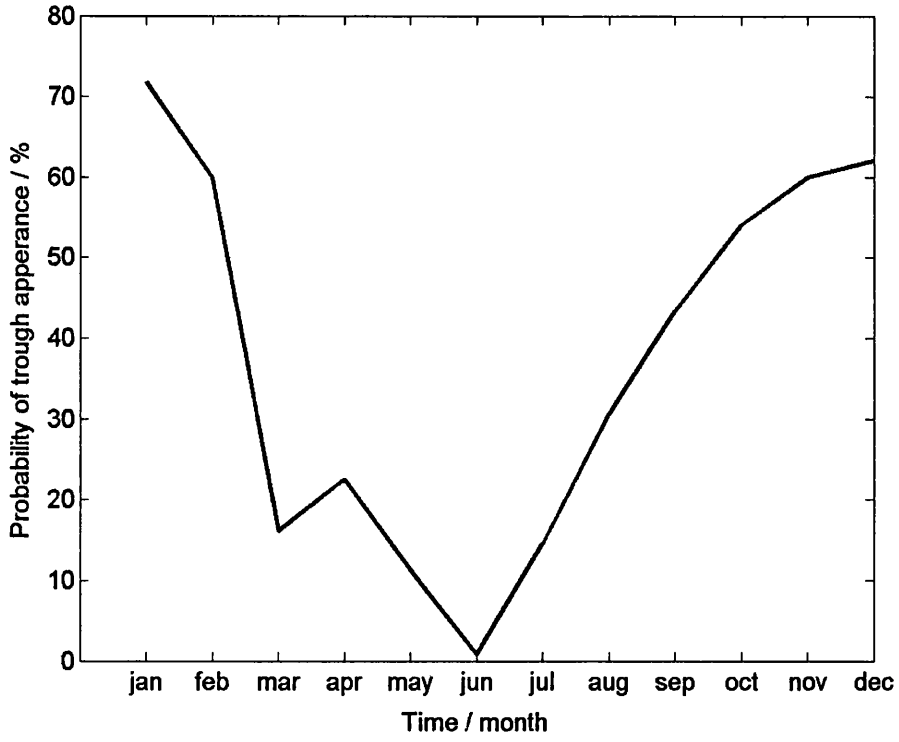

Figure 7.4. Monthly probability of trough occurrence for 2002 between 18UT and 00UT.

7.4 Trough modelling

The ability to predict the location of the trough was tested for various sets of the following data sets. Universal Time (UT), longitude, planetary magnetic index (K_p), Disturbance Storm Time index (D_{st}) and seasonal term (dN). The seasonal term used was the number of days from the summer solstice (day number 172). The trough locations were modelled using both geographic (GG) and geomagnetic (GM) co-ordinate systems. Results for various combinations of parameters for pre-midnight hours are given in Table 7.1. Methods A to F were produced by adding parameters to the input database. Method A has no input parameters and thus predicts a constant trough position output. Method B also includes the search longitude, C includes the Universal Time, D takes in the magnetic index, E adds the Storm index, and finally, Method F uses the seasonal parameter.

Table 7.1. Trough modelling coefficients and accuracy using different combinations of input parameters.

Method	GG / GM	Constant	Longitude	UT	K_p	D_{st}	dN	Rms
A	GG	59.00	-	-	-	-	-	2.417
B	GG	58.78	0.03	-	-	-	-	2.397
C	GG	58.29	0.02	-0.21	-	-	-	2.378
D	GG	60.75	0.01	-0.47	-0.99	-	-	1.985
E	GG	60.28	0.01	-0.50	-0.79	0.02	-	1.890
F	GG	62.74	0.01	-0.60	-1.00	0.02	-0.02	1.765
A	GM	59.69	-	-	-	-	-	2.937
B	GM	73.11	-0.14	-	-	-	-	2.504
C	GM	73.41	-0.15	-0.11	-	-	-	2.498
D	GM	77.77	-0.17	-0.42	-1.02	-	-	2.110
E	GM	77.49	-0.17	-0.45	-0.81	0.02	-	2.013
F	GM	80.66	-0.18	-0.57	-1.04	0.02	-0.02	1.886

As more parameters are included, the accuracy of the resultant model improves. If the parameters are useful then this is to be expected, because a least-mean-square approach is used to find the coefficient fit. Introducing the magnetic activity, which results in an increased southerly movement with higher index, produces the largest single gain in accuracy. The D_{st} term helps to model the lower latitude troughs found in the period during and after a magnetic storm. The seasonal term is also seen to improve the model, as there is a general trend of the summer trough being at higher latitude, compared with winter troughs under similar conditions. Geomagnetic longitude was seen to be better than geographic longitude. This may be due to the trough having a closer link to the geomagnetic co-ordinate structure, but this result may be an effect produced by detecting the trough in the geographic domain, and then converting to geomagnetic coordinates for analysis. This should be studied in the future, but will require analysis of a similar series of images based in the geomagnetic domain, and is therefore not covered here due to the large amount of processing required.

Overall, the best rms accuracy of these modelling approaches was 1.8° latitude. Previous modelling approaches, using only local time and magnetic activity, have standard deviations of 1.9° or greater. Here the accuracy produced using K_p, UT and longitude is 1.99°, which is comparable to the accuracy of previous studies. Differences in accuracy may be due to the differing latitudinal boundaries of the studies, with high latitude troughs not being included due

to reduced receiver coverage over northern Europe. Also, the accuracy has been improved as troughs have been measured over a range of longitudes. Some studies have used only a chain of receivers along one magnetic or geographic longitude, and thus could not have the range that the study described here achieved.

7.5 Trough forecasting

The basic properties of the trough have been studied by many groups (see Chapter 1) and all show that the trough moves to lower latitudes towards local midnight and also for increased magnetic activity. For short time periods the magnetic index will not change greatly, as a result, the main parameter to be concerned with is the movement south due to local time. Three methods were tested for accuracy in forecasting the trough latitudinal position.

1. Persistence: A basic comparison where the trough is modelled as stationary and the previous location of the trough is used for the forecast period.
2. 1° southerly movement: Where a measured trough is moved 1° south per hour, an estimate of the mean velocity of the trough detailed in previous studies.
3. Local time dependant approach: This was produced using a study of trough velocity which is shown below.

The local time dependant approach was developed by measuring the movement of the trough over periods of two to four hours along all of the European longitudes. Figure 7.5 shows the result of the fitting procedure for the longitude 2°W during 2002. Here the average southerly movement is plotted against UT. The least-mean-squares fit of the points is also plotted.

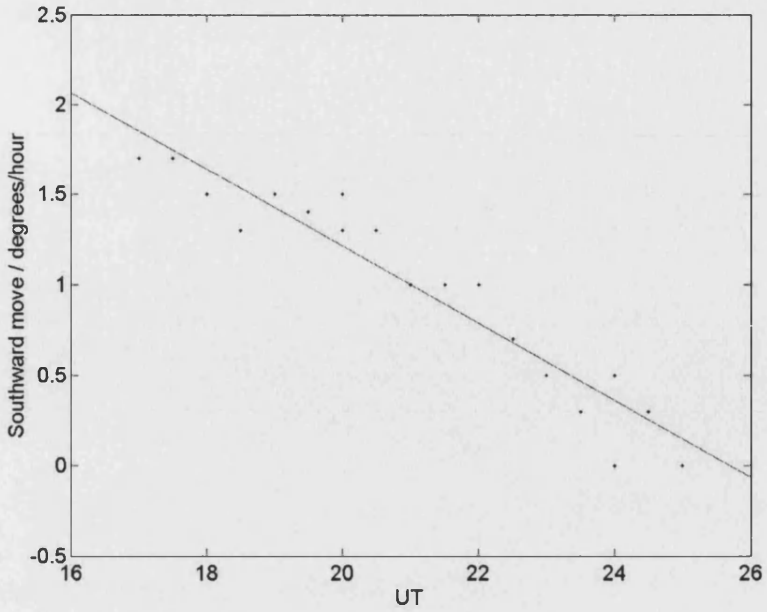

Figure 7.5. Southward trough movement against universal time for 2°W.

This was repeated for all European longitudes in the image region and compared to local time. Figure 7.6 shows that the linear fits produced for all of the separate longitudes follow the same trend.

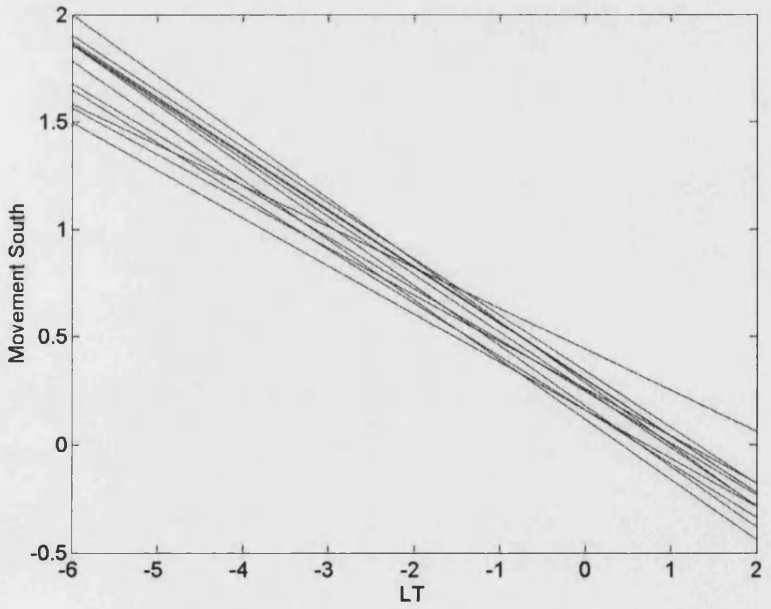

Figure 7.6. Southward trough movement against local time for European geographic longitudes.

The southerly velocity of the trough (Δ) was therefore approximated for all of the geographic longitudes using local time (t as Equation 7.2) and was found to be:

$$\Delta = 0.25 - 0.25t \qquad [7.2]$$

The full data set created for 2002 troughs was used to test the three forecasting methods, persistence, 1° southerly movement and local time shift. Table 7.2 and
Table 7.3 give the results for pre- and post-midnight trough forecasts for time periods of one, two and three hours.

Table 7.2. **Errors of trough forecasting methods between 6pm and midnight local time.**

Time / hours	1		2		3	
Method	rms	abs	rms	abs	rms	abs
Persistence	1.85	1.41	2.72	2.18	3.59	2.99
1 degree	1.66	1.22	2.07	1.52	2.39	1.78
LT shift	1.66	1.22	2.03	1.49	2.38	1.76

Table 7.3. **Errors of trough forecasting methods between midnight and 6am local time.**

Time / hours	1		2		3	
Method	rms	abs	rms	abs	rms	abs
Persistence	1.67	1.20	2.06	1.50	2.42	1.81
1 degree	1.78	1.33	2.39	1.87	2.98	2.42
LT	1.67	1.20	2.03	1.46	2.32	1.72

The errors suggest that a simple approach using constant movement will not yield the most accurate results. The LT approach gives the best results for both periods. Using the parameters from the modelling study with the measured trough latitude from the previous period to forecast the next trough position should yield improved results. The results for 1-hour forecasting using a least-mean-square fit based on troughs from 2001 to 2003 measured between 6pm and midnight is given in
Table 7.4.

Table 7.4. Coefficients and rms errors for 1-hour forecasts with trough measurement included.

GG/GM	c	tr	K_p	Dst	UT	Longitude	rms
GG	13.18	0.77	-	-	-	-	1.480
GG	18.82	0.69	-0.38	-	-	-	1.398
GG	19.73	0.68	-0.34	0.005	-	-	1.390
GG	20.30	0.67	-0.43	-	-0.10	-	1.391
GG	20.16	0.67	-0.42	-	-0.06	0.01	1.384
GG	21.64	0.64	-0.38	0.006	-0.09	0.01	1.373
GM	8.26	0.85	-	-	-	-	1.400
GM	11.71	0.81	-0.30	-	-	-	1.344
GM	12.03	0.80	-0.27	0.003	-	-	1.341
GM	11.78	0.81	-0.27	-	0.08	-	1.337
GM	17.94	0.75	-0.34	-	0.01	-0.03	1.322
GM	19.36	0.73	-0.31	0.004	-0.01	-0.03	1.316

The errors produced here are less than those produced by the modelling approaches and persistence (see Table 7.1, 7.2 and 7.3). The major increase in accuracy after the previous trough position has been included is the magnetic activity or K_p index. The relevance of using the other parameters is much less, as they improve the rms accuracy only by 0.03°. For this reason, further analysis will continue to use the movement model using the previous trough position and the magnetic activity over longer periods. Figure 7.7 shows the comparison between the forecast trough position and the measured trough position for one-hour forecasts using geographic and geomagnetic coordinate systems.

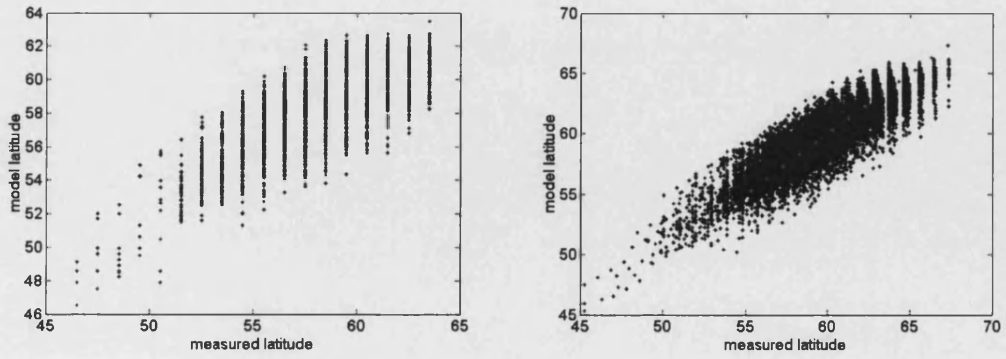

Figure 7.7. Geographic and geomagnetic comparisons for measured and forecast trough position.

An example of the movement the formula produces is shown in Figure 7.8 for a trough located at 65°N for magnetic activity of 1, 3, 5, 7 and 9 K_p index (coefficients from Table 7.4 using geographic co-ordinates, previous trough position and K_p only). The lines are in order of magnetic activity with the top line having the lowest K_p. The figure shows movement of the trough to lower latitudes as geomagnetic activity increases, and time progresses.

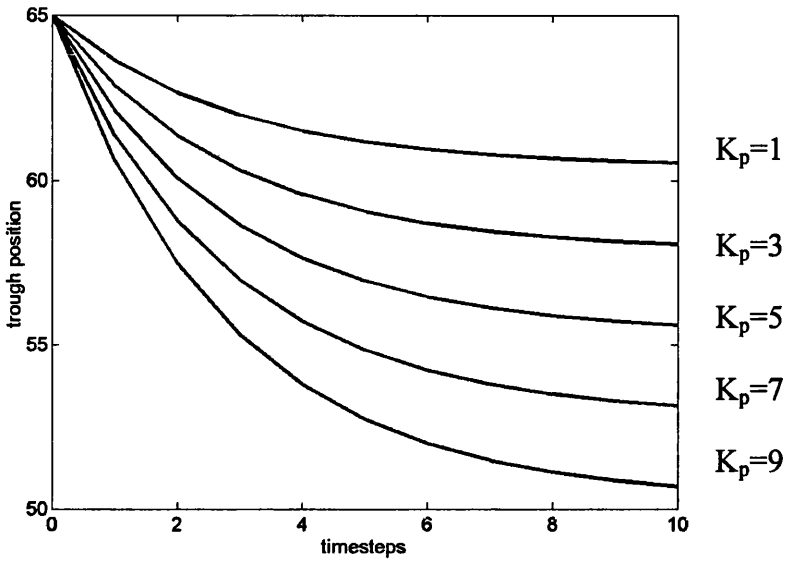

Figure 7.8. Forecasted positions of a trough detected at 65°N for five separate magnetic activities for 1-hour timesteps.

7.6 Other trough characteristics

The studies carried out for the trough position were also carried out for other trough characteristics to improve the final trough model for use with ionospheric forecasting. The first to be tried was the TEC at the trough minimum. This is useful for forecasts as changes in the minimum would not be picked up by a general move of the voxels using the movement model only, produced in the previous sections. The indices and parameters used for the study were again tested for the set of geographic trough data in years from 2000 to the end of 2003, and the results given in Table 7.5.

Table 7.5. Fitting for the trough minimum TEC (in TECU).

Method	c	tr	K_p	Dst	UT	Longitude	DN	F10.7	rms
A	5.17	-	-	-	-	-	-	-	3.562
B	4.51	-	0.03	-0.03	-0.03	-0.02	-	-	3.420
C	10.06	-	-	-	-	-	-0.04	-	3.104
D	0.12	-	-	-	-	-	-	0.03	3.288
E	4.81	-	-	-	-	-	-0.04	0.04	2.713
F	1.25	0.68	-	-	-	-	-	-	2.258
G	1.63	0.53	-	-	-	-	-0.02	0.01	2.162

Indices that produced the best results for trough latitude forecasting (K_p, Dst, UT and longitude) did not produce large improvements in prediction accuracy for the trough minimum. This is shown by Method B having accuracy similar to Method A, which is a simple trough with constant TEC minimum for all trough occurrences. Instead, the best parameters related to the day number (Method C) and the solar flux (Method D), F10.7 index. Measurements were found to lead to greater improvement, with an increased accuracy for a combination of these two parameters (Method E). The largest single improvement was found when including the trough minimum measured in the previous hour (Method F). Further small improvements were seen when combining the radio flux, day number and the previous trough measurement (Method G).

Figure 7.9 shows a direct comparison with the trough model and the measured trough minimum using the previous trough position with the seasonal term and the solar flux.

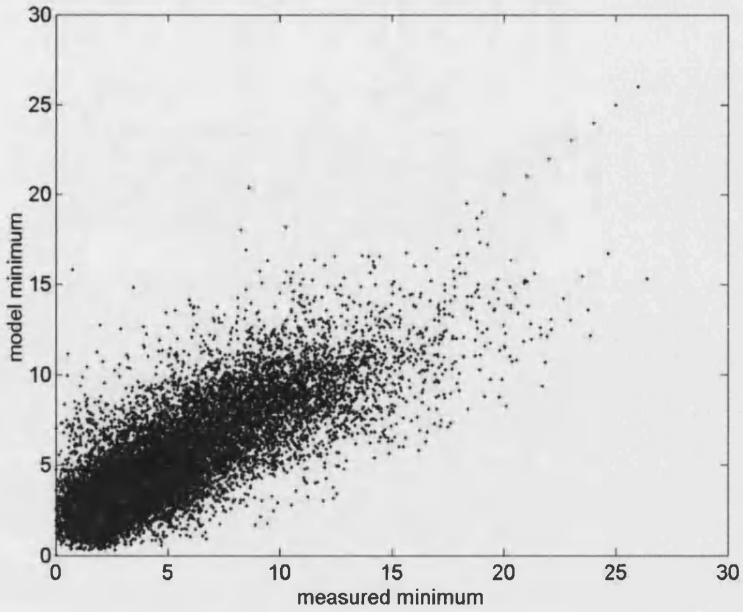

Figure 7.9. Direct comparison of modelled and measured TEC at the trough minimum.

There is a good agreement between the modelled and forecast TEC with rms error of 2.162 TECU, although larger errors can be seen when the trough minimum is greater. A longer data series is required to forecast the movement with greater accuracy, as these troughs do not occur in the high numbers seen for trough minimums less than 15 TECU. This is due to troughs with high TEC being most common during the summer and early evening. A result that is a small proportion of the total troughs (see Section 8.4 for trough appearance trends).

The results of longer predictions using the trough minimum from the previous hour, along with the seasonal term and the radio flux are shown in Table 7.6.

Table 7.6. Coefficients and rms errors for the model and persistence methods when forecasting the trough minimum over 1 to 5 hours using the previous trough position, tr, seasonal term, DN, and radio flux, F10.7.

Hours	c	tr	DN	F10.7	Model	Persistence
1	1.63	0.53	-0.02	0.01	2.162	2.728
2	1.28	0.41	-0.01	0.02	2.083	3.294
3	1.25	0.30	-0.01	0.03	2.049	4.143
4	0.98	0.25	-0.01	0.02	1.992	5.025
5	1.68	0.22	-0.01	0.01	2.158	6.275

It can be seen that the use of the model improves upon the basic approach of persistence, which uses the previous value of the trough minimum. The general trend of the trough is that the minimum TEC decreases as the evening progresses. The results show a small improvement may be possible by using such models to forecast the future TEC of the trough minimum. The accuracy of the results is similar to that produced by using the IRI temporal gradients to predict changes in TEC. The next section will focus on combining two methods to forecast the night-time ionosphere, the trough movement model introduced earlier in this chapter, and the IRI temporal gradients method shown in Chapter 6.

7.7 Using the model

The accuracy of the TEC forecasting approach using IRI temporal gradients, with the addition of the trough model was tested for wide-area forecasting. It is tested for troughs during 2002. To ensure the model is verified using unfitted data, the model is calculated using the trough measurements from the year 2001. This fit is given below in Equation 7.3:

$$\Lambda_t = 16.9 - 0.43K_p + 0.72\Lambda_{t-1} \qquad [7.3]$$

Three methods are tested for accuracy for forecasting European TEC. Persistence uses the image from the previous time step. The second improves on this by modelling the change in TEC over the period by calculating the temporal gradients from the 1995 version of the International Reference Ionosphere, IRI95, and applying these to the most recent TEC image. The third also uses these temporal gradients but shifts the image by the amount forecast by the model with the movement rounded to the nearest degree, which is the size of the voxels in the latitudinal direction. The results of the 2002 study are given below for three time periods of one, two and three hours with the accuracy shown by calculating the rms trough position error and absolute TEC error. These results are given in Table 7.7.

Table 7.7. Accuracy of trough positional forecast and absolute TEC errors for 1, 2 and 3 hour forecasts.

Method \ hrs	1		2		3	
	Tr pos	TEC	Tr pos	TEC	Tr pos	TEC
Persistence	1.88	2.99	2.81	4.79	3.62	6.88
IRI gradients	1.91	2.26	2.77	2.65	3.55	2.99
IRI + Model	1.60	2.25	1.88	2.54	2.05	2.84

It is clear that persistence produces the least accurate result, as it does not take account of any variation of the ionosphere. The TEC errors for both of the IRI gradient approaches improve greatly on the results obtained with persistence, especially over the longer forecast periods. The trough position is forecast to good accuracy for short time periods by all methods, but without the trough movement model, errors increase rapidly as the forecast period lengthens. For example, a one-hour forecast for persistence has 17.5% lower accuracy than the movement model, but for three-hour forecasts, persistence accuracy is 76.6% lower. For short forecast periods, the model does not improve persistence greatly, due to the trough movement being comparable to the resolution of the trough position measurement. As the forecast period increases, the trough movement forecast by the model is greater, and the accuracy of the measurement is less.

Examples of the images produced are shown in Figure 7.10 for 23UT October 21st 2002. The first two maps are the results of inversions from MIDAS. The left image shows the TEC map produced by MIDAS at 21UT, the second is the MIDAS image two hours later, 23UT, and the third is the forecast image for 23UT from the image at 21UT.

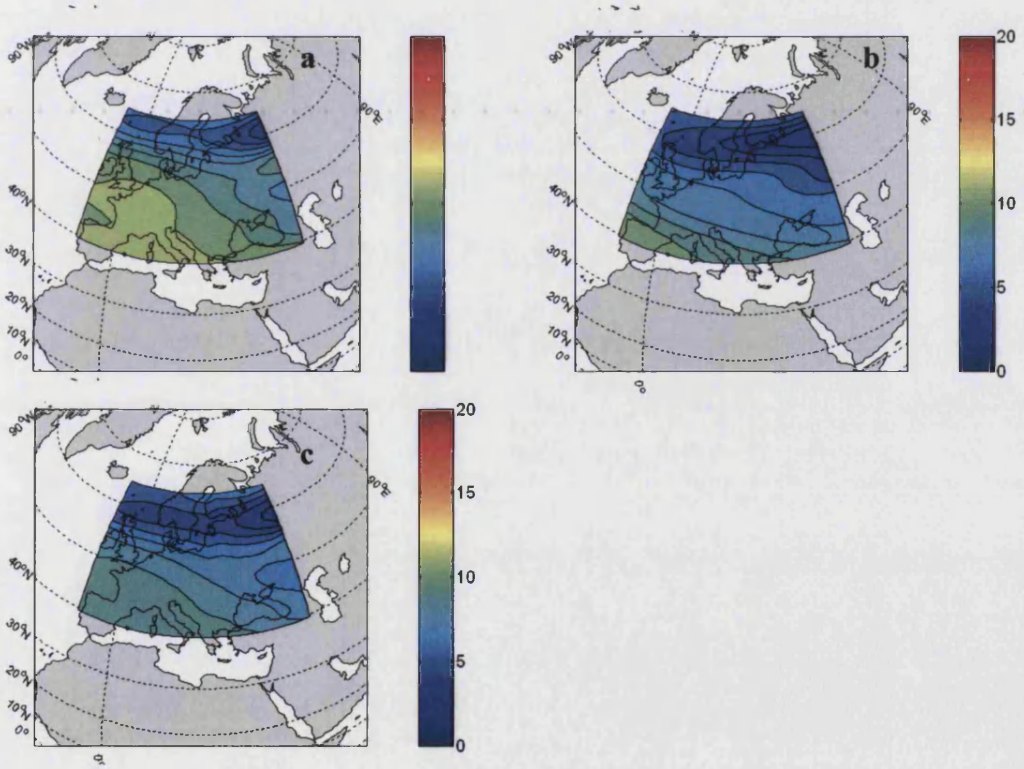

Figure 7.10. Vertical TEC images on October 21st 2002 showing the MIDAS inversion at 23UT (a), the image produced using the persistence method from 21UT (b) and the forecasted image using IRI and the trough movement model (c) (in TEC units).

In the images, the trough was detected for latitudes between 61° and 63° at 21UT and for the two hour forecast period the movement predicted was 2° at eastern longitudes, increasing to 3° at western longitudes. In this example, the rms trough position error was 1.27° and the absolute TEC error for the forecast image was 2.48 TEC units. The basic shape of the trough, such as width, depth and gradient of walls, is not altered thus any variation of the trough shape will not be produced. The accuracy in this example is greater than the overall accuracy calculated for the two-hour forecasts. This is because the trough has been detected over all longitudes in both time periods, which illustrates that a strong trough has developed and so will have better defined future movement. Troughs which cover only a few longitudes do not have such a well defined movement. Also, such results may be due to the depletion detected not being the main trough. The results were filtered to reduce the effect of other features by only including longstanding depletions, but this has not completely removed the effect.

7.8 Conclusions

In this Chapter, the effectiveness of TEC forecasting during night-time was explained. In particular, methods to accommodate the movement of the trough were developed and tested. This involved various input parameters such as UT, longitude, K_p, DST and time of year. Trough position forecasts were first produced using persistence and a 1° southerly shift. This produced larger errors than the local time modelling approach, for either the pre or post-midnight period, due to the change of the velocity of the trough depending upon local time. An approach, which varied the velocity of the trough dependant upon local time, produced an improvement of the accuracies. Forecasts were then produced using various parameters and the previous trough position. The previous trough position was the most effective with a linear approach resulting in a dependence, similar to the local time approach. The other major improvement was found by using the magnetic activity.

The use of the most accurate model for producing TEC forecasts was then shown and found to improve the accuracy over the simple IRI gradients approach by 11%. The accuracy of the IRI temporal gradients with the trough movement model improved TEC forecasts compared to persistence by 59% for longer periods. Trough position was improved by over 40% for longer forecast periods.

Further work must be carried out to investigate whether this approach will produce accurate results for all solar conditions at different periods of the solar cycle. The data is based on a period during the maximum of the solar cycle and are only based on medium to high sunspot

numbers. Other parameters may also be found to have a greater influence on such longer data sets. Also by studying other trough characteristics such as the depth and trough width a better trough forecast may be able to be produced by altering the trough shape further into the night.

Chapter 8 Summary and Conclusions

The research contained within this thesis has established the accuracy of mid-latitude ionospheric imaging and has laid the foundations for a real-time imaging system. The simulation results have shown that the MIDAS algorithm can be used to produce accurate ionospheric images in the European region, which could be later used for forecasting the ionospheric TEC. Comparisons were made with independent instrumentation, and it was shown that a systematic underestimation of the electron concentration occurred when using a standard set of orthonormal functions to represent the vertical profile of the electron density. This was due to the lack of information about the vertical profile that can be obtained from GPS satellite to ground links at mid-latitudes. Consequently, a new method that incorporated ionosonde measurements into the imaging was tested. This improved the peak density in the reconstructions. It was therefore found to be crucial to include ionosonde data into MIDAS inversions when peak electron concentrations are needed to be determined. However, if only vertical TEC maps are required, then data from ionosondes is not necessary and TEC images can be accurately generated from GPS data alone. The forecasted TEC rms accuracy that can be achieved is typically 1.0 TEC units, or absolute accuracy of 0.7 TEC units.

A key problem in using GPS data for ionospheric studies is the removal of the satellite and receiver interfrequency biases. The MIDAS software is capable of making estimates of the biases, since independent calibration of the differential carrier-phase method can be performed. The simulation study in Chapter 5, has shown that the biases and hence slant TEC can be estimated to an rms, mean and absolute accuracy of 2.6, 0.8, 1.8 TEC units respectively or vertical TEC accuracy of 1.3, 0.4, and 0.9 TEC units. This was then compared using real data, in which changes in the bias values were clearly detected, and the interfrequency bias closely correlated with independent sources of the biases. This shows that the MIDAS algorithm produces accurate images since the source of error has been removed.

After successfully establishing the capabilities and limitations, the primary goal of forecasting was tackled. This was divided into day and night sections. A number of different approaches to vertical TEC forecasting were developed. Those that had been shown to work well for single locations did not translate directly into forecasting of TEC maps. The daytime forecasting showed that TEC could be forecast to within absolute accuracy of 2.97, 4.63 and 4.95 TEC units for 1, 3 and 6 hours ahead, respectively. These are based on the assumption that the MIDAS images are correct. It should be noted that, in the worst case, the errors from the MIDAS images and the errors for the forecasting should be added.

For the night-time, special attention was given to the mid-latitude trough. Techniques for recognising this feature and forecasting the trough position were developed and in fact could be used as a stand-alone model for the trough. This could be incorporated into any other model such as IRI. The important input parameters to this model were magnetic activity, local time, DSP and time of year. This method achieved rms accuracies of 1.8°. When using the previous measured trough position, magnetic activity was the most parameter. This method improved accuracies to less than 1.4°. An alternative approach, of using a current ionospheric image and updating it with a forecast, was outlined. This method of ionospheric forecasting was shown to be very promising and could achieve TEC accuracies of 2.3 and 2.8 TECU, and trough latitude forecasts of 1.6 and 2.1 degrees for 1 and 3 hour forecast periods respectively.

From an application point of view the results here need to be interpreted with care. For example, the TEC error across an entire image may be very low, both in terms of percentage and absolute values, but the misplacement of the trough could have large detrimental effects on an HF prediction system. Also, a navigation correction system (such as differential GPS) that is concerned with the absolute TEC (proportional to delay) would suffer from a strong TEC gradient such as sunrise and sunset much more than it could from the trough, when the overall ionosphere is much lower in TEC. The approach here in this thesis has been to aim for the best overall prediction of the entire TEC map, in order to retain a realistic picture of the ionosphere in the forecast. This could be further optimised for a specific system.

This project has demonstrated the potential of real-time imaging of the ionospheric at mid-latitudes. Near real-time systems will have to cope with the need to collect measurements and to translate them into a format for the user. At present, a realistic aim would be to have data collection and translation completed within half an hour. Since the MIDAS software uses a one-hour window of data, and it is archived at the end of that hour, it is reasonable to assume that the prediction times stated in this thesis could be applied directly to a real-time imaging system and give ionospheric forecasts for up to five hours.

References

Andreeva, E. S., A. V. Galinov, V. E. Kunitsyn, Mel'nichenko, A. Yu, E. D. Tereshchenko, M. A. Filimonov and S. M. Chernykov (1990). "Radio tomographic reconstruction of ionisation dip in the plasma near the Earth." Journal of Experimental and Theoretical Physics letters **52**(145).

Austen, J. R., S. J. Franke and C. H. Liu (1988). "Ionospheric imaging using computerized tomography." Radio Science **23**(299).

Austen, J. R., S. J. Franke, C. H. Liu and K. C. Yeh (1986). "Application of computerized tomography techniques to ionospheric research." Proceedings of the Beacon Satellite Symposium 1986.

Baker, D. N., A. J. Kilmas, R. L. McPherron and J. Buchner (1990). "The evolution from weak to strong geomagnetic activity: An interpretation in terms of deterministic chaos." Geophysical Research Letters **17**: 41-44.

Bilitza, D. (1990). "International Reference Ionosphere 1990." NSSDC 90-22, Greenbelt, Maryland.

Bilitza, D. (1997). "International Reference Ionosphere-Status 1995/96." Advances in Space Research **20**(9): 1751-1754.

Bilitza, D., K. Rawer, L. Bossy and T. Gulyaeva (1993). "International Reference Ionosphere — Past, present, and future: I. Electron-density." Advances in Space Research **13**(3): 3-13.

Blewitt, G. (1990). "An automatic editing algorithm for GPS data." Geophysical Research Letters **17**(3): 199-202.

Boithias, L. (1983). "Propagation des ondes radioélectriques dans l'environnement terrestre." Collection Technique et Scientifique des Telecommunications CNET-ENST, Paris.

Buonsanto, M. J. (1999). "Ionospheric Storms - A Review." Space Science Reviews **88**: 563-601.

Bust, G. S., D. S. Coco and T. L. Gaussiaran (2001). "Computerized ionospheric tomography analysis of the Combined Ionospheric Campaign." Radio Science **36**(6): 1599-1605.

Cander, L. R., L. R. Stankovic and M. Milosavljevic (1997). "Dynamic ionospheric prediction by neural networks." Second International Workshop on Artificial Intelligence Applications in Solar-Terrestrial Physics, Sweden.

Coco, D. S., C. Coker, S. R. Dahkle and J. R. Clynch (1991). "Variability of GPS Satellite Differential Group Delay Biases." IEEE Transactions on Aerospace Electronic Systems **27**(6): 931-938.

Collis, P. N. and I. Haggstrom (1988). "Plasma convection and auroral precipitation processes associated with the main ionospheric trough at high latitude." Journal of Atmospheric and Terrestrial Physics **50**(4/5): 389-404.

Daniell, R. E., L. D. Brown, D. N. Anderson, M. W. Fox, P. H. Doherty, D. T. Decker, J. J. Sojka and R. W. Schunk (1995). "Parameterized Ionospheric Model: A Global Ionospheric Parameterization based on First Principles Models." Radio Science **30**(7): 1499-1510.

Davies, K. (1990). Ionospheric Radio, Peter Peregrinus Ltd.

Dick, M. J., M. F. Levy, L. R. Cander, I. Kutiev and P. Muhtarov (1999). "Short-Term Ionospheric Forecasting over Europe." IEE Conference Publication **461**: 105-107.

Francis, D. S., P. S. Cannon, A. G. Brown and D. S. Broomhead (2000). "Nonlinear prediction of the ionospheric parameter foF2 on hourly, daily, and monthly timescales." Journal of Geophysical Research **105**(A6): 12839-12849.

Fremouw, E. J., J. A. Secan and B. M. Howe (1992). "Application of stochastic inverse theory to ionospheric tomography." Radio Science **27**(5): 721-732.

Golub, G. H. and C. F. Van Loan (1989). Matrix Computations. Baltimore, John Hopkins University Press,.

Hajj, G. A., R. Ibanez-Meier, E. R. Kursinski and L. J. Romans (1994). "Imaging the ionosphere with the Global Positioning System." International Journal of Imaging Systems and Technology **5**(174).

Hajj, G. A., B. D. Wilson, C. Wang, X. Pi and I. G. Rosen (2002). "Ionospheric Data Assimilation of Ground GPS TEC by use of the Kalman Filter." Radio Science.

Hargreaves, J. K. and C. J. Burns (1996). "Electron content measurements in the auroral zone using GPS: preliminary observations of the main trough and a survey of the degree of irregularity in summer." Journal of Atmospheric and Terrestrial Physics **58**(13): 1449-1457.

Hedin, M., I. Haggstrom, A. Pellinen-Wannberg, L. Andersson, U. Barandstrom, B. Gustavsson, A. Steen, A. Westman, G. Wannberg, T. V. Eyken, T. Aso, C. Catell, C. Carlson and D. Klumpar (2001). "3-D extent of the main ionospheric trough - a case study." Advances in Polar Upper Atmosphere Research **14**: 157-162.

Kaplan, E. D. (1996). Understanding GPS principles and applications, Artech House.

Karpachev, A. T. and V. V. Afonin (1998). "Dependence of the probability of ionospheric-trough. Observations on the season, local time, longitude and level of geomagnetic activity." Geomagnetism and Aeronomy **38**(3): 325-333.

Karpachev, A. T., M. G. Deminov and V. V. Afonin (1996). "Model of the mid-latitude ionospheric trough on the base of COSMOS-900 and INTERCOSMOS-19 satellites data." Advances in Space Research **18**(6): (6)221-(6)230.

Kersley, L., S. E. Pryse, E. Walker, J. A. T. Heaton, C. N. Mitchell, M. J. Williams and C. A. Willson (1997). "Imaging of electron density troughs by tomographic techniques." Radio Science **32**: 1607-1623.

Kilmas, A. J., D. N. Baker, D. A. Roberts and D. H. Fairfield (1992). "A nonlinear dynamical analogue model of geomagnetic activity." Journal of Geophysical Research **97**: 12253-12266.

Klobuchar, J. A. (1987). "Ionospheric Time-Delay Algorithm for Single-Frequency GPS Users." IEEE Transactions on Aerospace and Electronic Systems **AES-23**(3).

Kohnlein, W. and W. J. Raitt (1977). "Position of the mid-latitude trough in the topside ionosphere as deduced from ESRO 4 observations." Planetary Space Sciences **25**: 600.

Lamming, X. and L. R. Cander (1997). "Monthly median ionospheric frequencies prediction with Neural Networks." Second International Workshop on Artificial Intelligence Applications in Solar-Terrestrial Physics, Sweden.

Leitinger, R. (1999). "Ionospheric Tomography." Review of Radio Science 1996-1999: 581-623.

Logsdon, T. (1992). The NAVSTAR Global Position System.

Lundstedt, H. (1992). "Prediction of solar-terrestrial effects." Planetary Space Sciences **12**(19): 457.

Lundstedt, H. and P. Wintoft (1992). "Prediction of geomagnetic storms from solar wind data with use of neural networks." Annals of Geophysics **12**(19).

Mannucci, A. J., B. A. Iijima, U. J. Lindqwister, X. Pi, L. Sparks and B. D. Wilson (1999). GPS and Ionosphere, Wiley-IEEE Press.

Mannucci, A. J., B. D. Wilson, D. N. Yuan, C. H. Ho, U. J. Lindqwister and T. F. Runge (1998). "A global mapping technique for GPS-derived ionospheric total electron content measurements." Radio Science **33**(3): 565-582.

Materassi, M., L. Ciraolo, P. Spalla, C. N. Mitchell and P. S. J. Spencer (2001). "The effect of the northern crest of the equatorial anomaly on propagation delay at GPS frequencies." Proc. of Global Navigation Satellite Systems Conf. Seville, Spain 8-11 May 2001.

Materassi, M. and C. N. Mitchell (2005). "A simulation study into constructing of the sample space for ionospheric imaging." Journal of Atmospheric and Solar-Terrestrial Space Physics **67**(12): 1085-1091.

McNamara, L. F. (1991). The Ionosphere: Communications, Surveillance, and Direction Finding, Krieger Publishing.

Meggs, R. W., C. N. Mitchell and V. S. C. Howells (2005). "Simultaneous observations of the main trough using GPS imaging and the EISCAT radar." Annales Geophysicae **23**(3): 753-757.

Millward (1996). "STEP Handbook on Ionospheric Models." Utah State University **239**.

Mitchell, C. N., T. Baxter and S. Musman (2000). "A comparison of methods for forecasting total electron content." Proceedings of IONGPS, Salt Lake City.

Mitchell, C. N., D. G. Jones, L. Kersley, S. E. Pryse and I. K. Walker (1995). "Imaging of field-aligned structures in the auroral ionosphere." Annals Geophysicae **13**: 1311.

Mitchell, C. N. and P. S. J. Spencer (2003). "A three-dimensional time dependent algorithm for ionospheric imaging using GPS." Annals of Geophysics **46**: 687-696.

Moffett, R. J. and S. Quegan (1983). "The mid-latitude trough in the electron concentration of the ionospheric F-layer: a review of observations and modelling." Journal of Atmospheric and Terrestrial Physics **45**(5): 315-343.

Pryse, S. E. and L. Kersley (1992). "A preliminary experimental test of ionospheric tomography." Journal of Atmospheric and Solar-Terrestrial Physics **54**(7-8): 1007-1012.

Pryse, S. E., C. N. Mitchell, J. A. T. Heaton and L. Kersley (1995). "Travelling ionospheric disturbances imaged by tomographic techniques." Annals Geophysicae **13**: 1325.

Ray, J. (2001). "updated <P1-C1> pseudorange bias corrections." IGS Mail 3160.

Raymund, T. D., S. E. Pryse, L. Kersley and J. A. T. Heaton (1993). "Tomographic reconstruction of ionospheric electron density with European incoherent scatter radar verification." Radio Science **28**(5): 811-818.

Rees, D. (1995). "Observations and modelling of ionsospheric and thermospheric disturbances during geomagnetic storms: A review." Journal of Atmospheric and Solar Terrestrial Physics **57**(12): 1433-1457.

Rishbeth, H. (2001). "The centenary of solar-terrestrial physics." Journal of Atmospheric and Solar-Terrestrial Physics **63**: 1883-1890.

Rodger, A. S., R. J. Moffett and S. Quegan (1992). "The role of ion drift in the formation of ionisation troughs in the mid- and high-latitude ionosphere --a review." Journal of Atmospheric and Terrestrial Physics **54**(1): 1-30.

Rycroft, M. J. and S. J. Burnell (1970). "Statistical analysis of movements of the ionospheric trough and the plasmapause." Journal of Geophysical Research **75**: 5600-5604.

Sardon, E. and N. Zarraoa (1997). "Estimation of Total Electron Content using GPS Data- How stable are the differential satellite and receiver instrumental biases." Radio Science **32**: 1899-1910.

Schaer, S., B. Gerhard and M. Rothacher (1998). "Mapping and predicting the ionosphere." Proceedings of the IGS AC Workshop, Darmstadt, Germany.

Schunk, R. W., L. Scherliess and J. J. Sojka (2002). "Ionospheric Specification and Forecast Modelling." Journal of Spacecraft and Rockets **39**(2): 314-324.

Stanislawska, I. and Z. Zbyszynski (2001). "Forecasting of the ionospheric quiet and disturbed foF2 values at a single location." Radio Science **36**(5): 1065-1071.

Stanislawska, I. and Z. Zbyszynski (2003). "Forecasting of the Total Electron Content at a single location." Cosmic Research **41**(4): 353-356.

Tsagouri, I., B. Zoleski and A. Belehaki (2005). "Evaluation of the performance of the real-time updated simplified ionospheric regional model for the European area." Journal of Atmospheric and Solar Terrestrial Physics **67**(12): 1137-1146.

Vassiliadis, D. A., S. Sharma, D. N. Baker and D. A. Roberts (1995). "A description of the solar-wind magnetosphere coupling based on non-linear filters." Journal of Geophysical Research **100**: 3495-3512.

Williscroft, L. A. and A. W. V. Poole (1996). "Neural networks, foF2, sunspot number and magnetic activity." Journal of Geophysical Research **100**: 3495-3512.

Wilson, B. D. and A. J. Mannucci (1993). "Instrumental biases in ionospheric measurements derived from GPS data." Proceedings of the institute of Navigation GPS-93: 1343.

Wu, J.-G. and H. Lundstedt (1996). "Prediction of geomagnetic storms from solar wind data using Elman recurrent neural networks." Geophysical Research Letters **23**(4): 319-322.

Yeh, K. C. and T. D. Raymund (1991). "Limitations of ionospheric imaging by tomography." Radio Science **26**(6): 1361-1380.

Yin, P., C. N. Mitchell, P. S. J. Spencer and J. C. Foster (2004). "Ionospheric electron concentration imaging using GPS over the USA during the storm of July 2000." Geophysical Research Letters **31**(12): L12806 1-4.

Zolesi, B., A. Belehaki, I. Tsagouri and L. R. Cander (2004). "Real-time updating of the simplified ionospheric regional model for operational applications." Radio Science **39**(2).

Zolesi, B., L. R. Cander and G. D. Franceschi (1996). "On the potential applicability of the simplified ionospheric model to different midlatitude areas." Radio Science **31**(3).